

Deformation Mechanisms in Polymer-Clay Nanocomposites

by

Amit K. Kaushik

A dissertation submitted in partial fulfillment
of the requirements for the degree of
Doctor of Philosophy
(Mechanical Engineering)
in The University of Michigan
2010

Doctoral Committee:

Professor Ellen M. Arruda, Chair
Professor John Kieffer
Professor Anthony M. Waas
Assistant Professor Samantha H. Daly

© Amit K. Kaushik 2010
All Rights Reserved

To my mom, dad, brothers and beloved wife Neeru

Acknowledgements

The last five years have been truly wonderful, all because of the support, help, love and advice from many excellent people. First and foremost, I am extremely grateful to my advisor Prof. Ellen M. Arruda for her tremendous guidance, encouragement, kindness and trust in me throughout my doctoral studies. I really appreciate her great mentorship skills from which I have drawn encouragements for academic accomplishments and personal growth. I would like to thank her for the brilliant ideas she gave to drive my research work and her accessibility whenever I needed any guidance or help. I have learnt a great deal from her and I will always cherish the long technical discussions we have had during our weekly meetings.

I also appreciate working with Prof. Anthony M. Waas and Prof. Nicholas A. Kotov of Aerospace Engineering and Chemical Engineering department respectively throughout my PhD work. Specifically, I am thankful to Prof. Waas for his wonderful guidance and brilliant ideas at numerous point of times in my thesis work. I am thankful to Prof. Kotov for helping me develop an understanding of polymer chemistry and polymer physics.

Next, I would like to thank Prof. John Kieffer, Prof. Waas and Prof. Samantha H. Daly for their valuable advice and participation in my dissertation committee. I would like to thank Prof. Martin for help with discussions and interpretations of X-ray diffraction data and participation in my preliminary exam committee. Next, I would like to thank Prof. Kieffer for letting me conduct Brillouin light scattering and Raman spectroscopy experiments in his laboratory.

I also appreciate working with Harish, Coco, Jinjin, Beth, Sarah, Fatima, Ben and Kevin from my lab; Paul, Ming Qin, Ming Yang and Jian from Prof. Kotov's group; Kyubum and Adam from Prof. Daly's group; Eugene and Amit from Prof. Waas's group; Lang from Prof. Kieffer's group and Charlie from Prof. Martin's group. I would like to thank Charlie, Kelly and Patty for their assistance. Next, I would like to thank great friends at Ann Arbor whose friendship I will always cherish: GB, Ashish, Siby, Sud, Deba, Saamil, Anurag, Naveen, Trushal, Shiva, Chandresh, Sunil among others I am sure to have left out. I will always cherish the tea session discussions I have had with GB, Ashish, Siby and Sud at the

MSE kitchen where we discussed pretty much everything one can think of: from cricket to nanotechnology.

Next, I would like to thank my wife, Neeru, for her love, patience, support and encouragement which she provided me this whole time. I can't imagine what I would be today without her love and support. Finally, I would like to thank my loving parents and parents-in-law for their support throughout these years.

This work was financially supported by the Office of Naval Research and Rackham Travel Grant.

Table of Contents

Dedication	ii
Acknowledgements	iii
List of Tables	viii
List of Figures	x
Abstract	xviii
Chapter 1 Project Motivation and Outline	1
Chapter 2 Background	4
2.1 Polymer Nanocomposites	5
2.2 The State of Deformation Mechanisms in Polymer-Clay Nanocomposites .	10
2.3 Layer-by-Layer Manufacturing	13
2.4 Purpose and Research Overview	15
2.5 Ultrastrong and Stiff PVA-MTM Nanocomposite	17
Chapter 3 Experimental Details	23
3.1 Materials	23
3.2 Synthesis of Nanocomposites	24
3.2.1 Linear LBL Nanocomposites	25
3.2.2 Exponential-LBL Nanocomposites	26
3.3 Consolidation of Thin Films	27
3.4 Sonication of MTM nanoparticles	28
3.5 Characterization	29
3.5.1 Thermogravimetric Analysis	29
3.5.2 Wide Angle X-ray Diffraction	30
3.5.3 Scanning Electron Microscopy	30

3.5.4	Low Strain-rate Mechanical Testing	30
3.5.5	High Strain-Rate Mechanical Testing	32
3.5.6	Brillouin Light Scattering	39
3.5.7	Ellipsometry	41
3.5.8	Particle Size Measurement	42
3.5.9	Differential Scanning Calorimetry	42
3.5.10	Dynamic Mechanical Analysis	43
Chapter 4 MTM Nanoparticle Volume Fraction and Layer Separation		44
4.1	Linear Layer-by-Layer Nanocomposites	44
4.2	Structural Characterization	46
4.3	Mechanical Characterization	53
4.4	Thermal Characterization	61
4.5	Thermo-Mechanical Characterization	63
4.6	Summary and Conclusions	64
Chapter 5 MTM Nanoparticle Layer Stratification		66
5.1	Structural Characterization	66
5.2	Mechanical Characterization	70
5.3	Summary and Conclusions	72
Chapter 6 Constitutive Model for PU and PU-MTM Nanocomposites		76
6.1	Constitutive Modeling of Polymers	76
6.1.1	Yield Model: Argon Model	76
6.1.2	Strain Hardening Model: Eight Chain Model	78
6.1.3	Modeling of Polyurethane	79
6.2	Modeling of Polymer-Clay Nanocomposites	81
6.3	Modeling Approach	83
6.3.1	Modeling Constituents	85
6.3.2	Material Parameters Identification	90
6.4	Modeling Results and Discussion	92
6.5	Summary and Conclusions	96
Chapter 7 Polymer-Nanoparticle Interface		99
7.1	Exponential Layer-by-Layer Nanocomposites	99
7.2	Uniform and Hierarchical-Layered Nanocomposites	101
7.3	Structural Characterization	104

7.4	Mechanical Characterization	109
7.5	High Strain-Rate Characterization and Potential Applications in Blast Mit- igation	118
7.6	Summary and Conclusions	125
Chapter 8	Summary and Future Work	130
Bibliography		134

List of Tables

Table

3.1	Densities of polymers and MTM clay used in the present work.	29
4.1	PU-MTM nanocomposite nomenclature[86].	48
4.2	Thickness of 300-bilayer PU-MTM nanocomposites and average bilayer thickness as a function of average volume fraction of MTM nanoparticles[86].	48
4.3	Summary of the mechanical properties of pure PU and PU-MTM nanocomposites at a constant strain rate of 0.005/s at room temperature ($\sim 23^\circ\text{C}$) and a humidity of $\sim 30\%$ [86].	55
4.4	Summary of the mechanical properties of pure PU and PU-MTM nanocomposites at a constant strain rate of 0.005/s at room temperature ($\sim 23^\circ\text{C}$) and a humidity of $\sim 30\%$ [86].	56
5.1	PU-SMTM nanocomposite nomenclature.	69
6.1	Summary of structural and mechanical properties of PU and PU-MTM nanocomposites at a constant strain rate of 0.005/s at room temperature ($\sim 23^\circ\text{C}$) and a humidity of $\sim 30\%$ [86].	84
6.2	Summary of constitutive model and material parameters[139].	90
6.3	Material parameters for bulk PU and effective particle[139].	94
7.1	Uniform-layered PU-PAA-MTM nanocomposite nomenclature.	103
7.2	Hierarchical-layered PU-PAA-MTM nanocomposite nomenclature.	104
7.3	Summary of the mechanical properties of PU, PU-PAA and uniform-layered PU-PAA-MTM nanocomposites at a constant strain rate of 0.005/s at room temperature ($\sim 23^\circ\text{C}$) and a humidity of $\sim 30\%$. Numbers shown indicate average volume fractions of MTM nanoparticles.	110

7.4 Summary of the mechanical properties of PU, PU-PAA and uniform-layered
PU-PAA-MTM nanocomposites at a constant strain rate of 0.005/s at room
temperature ($\sim 23\text{ }^{\circ}\text{C}$) and a humidity of $\sim 30\%$ 111

List of Figures

Figure

2.1	A scanning electron micrograph of a thermoplastic olefin[11]	5
2.2	An Ares V Cargo Launch Vehicle composed of a composite shroud[13]. . .	6
2.3	Structures of commonly used nano-fillers.	8
2.4	Structure of a Montmorillonite clay[33].	9
2.5	Schematic illustrations of the (A) intercalated and (B) exfoliated nanocomposites.	10
2.6	Modulus (shown in black circles) and ultimate stress (shown in green triangles) of intercalated epoxy-clay nanocomposites as a function of the clay concentration[56].	12
2.7	Modulus of nanocomposites of polyurethane and various organoclays as a function of clay content[58].	12
2.8	Scanning electron microscopy image of polypropylene-calcium carbonate nanocomposites with (A) 5 v.%, (B) 9 v.% and (C) 13 v.% calcium carbonate[42].	13
2.9	Schematic of the LBL manufacturing technique[61]. Deposition cycle includes: (1) deposition of positively charged polyelectrolyte, (2) rinsing with a polar solvent, (3) deposition of negatively charged polyelectrolyte, and (4) rinsing with a polar solvent.	14
2.10	(A) Photograph of a sea-shell, (B) Microstructure of Nacre[77], (C) Photograph of a poly(vinyl alcohol)-montmorillonite clay[55], and (D) Scanning electron microscope image of the cross-section of a 300-bilayer poly(vinyl alcohol)-montmorillonite nanocomposite[55].	16
2.11	An AFM phase image of a single PVA-MTM bilayer adsorbed on top of a silicon wafer. The inset shows the close up of the main image showing individual MTM platelets more clearly[55].	18
2.12	Thickness results for PVA-MTM nanocomposite for the first 10 deposition cycles from ellipsometry[55].	18

2.13	Representative nominal stress-strain constitutive response of PVA and PVA-MTM nanocomposite with 50 v.% MTM nanoparticles[55]. The dog-bone specimens were loaded at a constant strain rate of 0.005/s at room temperature ($\sim 23^\circ\text{C}$) and a humidity of $\sim 30\%$ until failure.	19
2.14	Differential scanning calorimetry analysis results for PVA and PVA-MTM nanocomposite with 50 v.% MTM nanoparticles[55].	21
2.15	Differential scanning calorimetry analysis results for Chitin and Nacre.	21
3.1	Schematic of consolidation of free-standing e-LBL films. (A) Consolidation procedure: (1) The films were taken and (2) stacked together into a sandwich structure to achieve conformal overlap, (3) the stack is hot-pressed at < 15 MPa pressure and 110°C , (4) final consolidated stack. (B) Photograph of a free-standing, 100-bilayer PU-PAA film. (C) Photograph of 100 100-bilayer free-standing films combined into a stack. (D) Photograph of a final hot-pressed stack.[85]	28
3.2	A custom-designed tensile tester to measure the mechanical properties of polymers and polymer-clay nanocomposites at low strain rates.	31
3.3	(A) A sample voltage calibration curve for a load cell used in the tensile tester. Numbers indicate weights in grams. (B) Force-voltage calibration curve for the load cell.	32
3.4	A schematic illustrating the determination of material strain in the specimens.	33
3.5	(A) A schematic of a split-Hopkinson pressure bar apparatus[11].(B) A photograph of an in-house built aluminum split-Hopkinson pressure bar apparatus.	35
3.6	A typical oscilloscope voltage output showing the incident, reflected and transmitted pulses.	36
3.7	Sketch showing the variables and constants for processing the stress, strain and strain-rate from the incident, reflected and transmitted pulses. Subscripts I, R, T and S are associated with the incident bar, reflected bar (same as incident bar), transmission bar and specimen respectively.	37
3.8	Backscattering geometry diagram for thin films S deposited on a reflecting surface (R) like Silicon wafer[92].	40
4.1	A schematic of an LBL deposition showing the electrostatic charges.	45
4.2	Ideal schematic of nanocomposite structure with (A) lower volume fraction and (B) higher volume fraction of MTM nanoparticles[86].	46

4.3	Thermogravimetric analysis for PU, a series of PU-MTM nanocomposites and MTM clay[86].	47
4.4	Typical SEM images showing cross-sections of (a) 5 v.%, (b) 7 v.%, (c) 9 v.%, (d) 12 v.% and (e) 20 v.% 300-bilayer PU-MTM nanocomposite[86].	48
4.5	Thickness of 300-bilayer PU-MTM nanocomposites as a function of volume fractions of MTM nanoparticles. Error bars indicate the uncertainty in thicknesses and volume fractions.	49
4.6	Linear growth in film thickness of PU-MTM5 nanocomposite as a function of bilayers. Error bars indicate the uncertainty in thicknesses[86].	49
4.7	Chemical Structure of cationic PU copolymer. The cationic functional group of the polymer is highlighted in red, the counter-ion in blue, the soft segment in green and the hard segment in black[86].	50
4.8	Wide angle X-ray diffraction patterns of PU, MTM clay and PU-MTM nanocomposites. Numbers indicate average volume fractions of MTM nanoparticles[86].	50
4.9	Schematic nanostructure of the PU-MTM Nanocomposite[86].	51
4.10	Representative nominal stress-strain constitutive response curves of PU and PU-MTM nanocomposites. The dog-bone specimens were loaded at a constant strain rate of 0.005/s at room temperature ($\sim 23^\circ\text{C}$) and a humidity of $\sim 30\%$ until failure. Numbers shown indicate average volume fractions of MTM nanoparticles[86].	54
4.11	Representative true stress-strain constitutive response curves of PU and PU-MTM nanocomposites. The dog-bone specimens were loaded at a constant strain rate of 0.005/s at room temperature ($\sim 23^\circ\text{C}$) and a humidity of $\sim 30\%$ until failure. Numbers shown indicate average volume fractions of MTM nanoparticles[86].	55
4.12	Representative nominal stress-strain constitutive responses for 12 v.% PU-MTM nanocomposite specimens. The dog-bone specimens were loaded at a constant strain rate of 0.005/s at room temperature ($\sim 23^\circ\text{C}$) and a humidity of $\sim 30\%$ until failure[86].	57
4.13	Comparison of enhancement in modulus of PU-MTM nanocomposites with other clay nanocomposites[86].	58
4.14	Strain energy at failure (shown as circular data points) and at 0.5 strain (shown as square data points) for PU and PU-MTM nanocomposites as a function of average volume fraction of MTM nanoparticles[86].	59

4.15	Modulus of PU and PU-MTM nanocomposites as a function of average volume fraction of MTM nanoparticles.	59
4.16	Yield strength of PU and PU-MTM nanocomposites as a function of average volume fraction of MTM nanoparticles.	60
4.17	DSC traces of pure PU and PU-MTM nanocomposites. Numbers indicate average volume fractions of MTM nanoparticles[86].	62
4.18	Area under the transition peak for Pure PU and PU-MTM nanocomposites normalized by the amount of PU present[86].	62
4.19	Storage modulus as a function of sample temperature for pure PU and PU-MTM nanocomposites. Numbers indicate average volume fractions of MTM nanoparticles[86].	63
4.20	$\tan\delta$ as a function of sample temperature for pure PU and PU-MTM nanocomposites. Numbers indicate average volume fractions of MTM nanoparticles[86].	64
5.1	Particle size in a sonicated MTM nanoparticle solution as a function of time after sonication.	67
5.2	Film thickness of 300-bilayer nanocomposites as a function of average PU bilayer thickness. Numbers indicate the average volume fraction of nanoparticles in the PU-SMTM and PU-MTM nanocomposites.	68
5.3	Wide angle X-ray diffraction patterns of PU, MTM clay, PU-MTM7 and PU-SMTM3 nanocomposites.	70
5.4	Representative nominal stress-strain responses of PU-SMTM nanocomposite as a function of volume fraction of MTM nanoparticles. The dog-bone specimens were loaded at a constant strain rate of 0.005/s at room temperature ($\sim 23^\circ\text{C}$) and a humidity of $\sim 30\%$ until failure. Numbers indicate the volume fraction of MTM nanoparticles.	73
5.5	A comparison of the modulus of PU-SMTM nanocomposites with PU-MTM nanocomposites as a function of volume fraction of nanoparticles.	74
5.6	A comparison of the ultimate yield strength of PU-SMTM nanocomposites with PU-MTM nanocomposites as a function of volume fraction of nanoparticles.	74
5.7	A comparison of the ultimate strain-to-failure of PU-SMTM nanocomposites with PU-MTM nanocomposites as a function of volume fraction of nanoparticles.	75

5.8	Film thickness of 300-bilayer nanocomposites as a function of average PU bilayer thickness. Numbers indicate the average volume fraction of nanoparticles in the PU-SMTM and PU-MTM nanocomposites. The vertical solid (in black) and dashed (in red) line shows the critical MTM layer separation in PU-MTM nanocomposites and PU-SMTM nanocomposites respectively. Below this separation, the nanocomposites demonstrate brittle behavior in the stress-strain response.	75
6.1	Argon kink pair yield model of intermolecular resistance in glassy polymers[108].	77
6.2	The unit cell of eight chain rubber elasticity model in an undeformed isotropic state and deformed state[114].	80
6.3	(A) A schematic of nanostructure of the PU-MTM nanocomposite[86]. (B) An equivalent representative volume element of the PU-MTM nanocomposite illustrating the interphase and effective particle concepts.	84
6.4	Mechanical analog of the proposed three-dimensional constitutive model for predicting the finite deformation response of PU-MTM nanocomposites[139].	86
6.5	Material parameter identification and parametric study for the non-linear elastic spring for the bulk PU[139].	91
6.6	True stress-strain constitutive response of PU-MTM nanocomposites with 5 v.% MTM nanocomposites. The dog-bone specimens were loaded at a constant strain rates of = 0.005/s, = 0.01/s and 0.05/s at room temperature ($\sim 23^\circ\text{C}$) and a humidity of $\sim 30\%$ until failure[139].	93
6.7	E_{ep} as a function of volume fraction of MTM nanoparticles, v_p and interphase thickness, t	95
6.8	Model results (in black) and experimental results (in color) for the finite deformation constitutive response of PU and PU-MTM nanocomposites at a strain rate of = 0.005/s at room temperature ($\sim 23^\circ\text{C}$) and a humidity of $\sim 30\%$ [139].	95
6.9	Model results (in black) and experimental results (in color) for the finite deformation constitutive response of PU and PU-MTM nanocomposites at a strain rate of = 0.005/s at room temperature ($\sim 23^\circ\text{C}$) and a humidity of $\sim 30\%$. The model results are without any amplified stretch, i.e. $X = 1$ [139].	97

6.10	Model predictions (in black) and experimental results (in color) for the finite deformation constitutive response of PU-MTM5 at strain rates of $= 0.01/s$ and $0.05/s$ at room temperature ($\sim 23^\circ C$) and a humidity of $\sim 30\%$ [139].	98
7.1	Schematic illustration of (A) a uniform-layered PU-PAA-MTM nanocomposite with a deposition sequence of $(PU/PAA/PU/MTM)_m$; and (B) a hierarchical-layered PU-PAA-MTM nanocomposite with a deposition sequence of $(PU/PAA/(PU/MTM)_5)_p$	102
7.2	Ideal schematic of structure of (A) PU-PAA nanocomposite with 0 v.% MTM nanoparticles; uniform-layered PU-PAA-MTM nanocomposite with (B) lower volume fraction and (C) higher volume fraction of MTM nanoparticles	103
7.3	Ideal schematic of nanocomposite structures of (A) PU-PAA-MTM6(h); and (B) PU-PAA-MTM8(h) hierarchical-layered nanocomposites	105
7.4	Film thickness for PU-PAA as function of number of bilayers. The growth is observed to be exponential for the first few bilayers[145].	106
7.5	Film thickness in e-LBL PU-PAA nanocomposites as a function of the number of bilayers. Film thicknesses in the traditional PU-MTM LBL nanocomposite with 5 v.% and 20 v.% MTM nanoparticles as a function of the number of bilayers are also shown for comparison.	107
7.6	Film thickness in an e-LBL nanocomposite with and with out MTM nanoparticles as function of number of bilayers.	108
7.7	Representative nominal stress-strain response of PU, PU-PAA and uniform-layered PU-PAA-MTM nanocomposites. The dog-bone specimens were loaded at a constant strain rate of $0.005/s$ at room temperature ($\sim 23^\circ C$) and a humidity of $\sim 30\%$ until failure. Numbers shown indicate average volume fractions of MTM nanoparticles.	111
7.8	Representative true stress-strain response of PU, PU-PAA and uniform-layered PU-PAA-MTM nanocomposites. The dog-bone specimens were loaded at a constant strain rate of $0.005/s$ at room temperature ($\sim 23^\circ C$) and a humidity of $\sim 30\%$ until failure. Numbers indicate the volume fraction of MTM nanoparticles.	112
7.9	Comparison of modulus of PU, PU-PAA and uniform-layered PU-PAA-MTM nanocomposites.	113

7.10	Comparison of yield strength of PU, PU-PAA and uniform-layered PU-PAA-MTM nanocomposites.	114
7.11	Comparison of ultimate strain-to-failure of PU, PU-PAA and uniform-layered PU-PAA-MTM nanocomposites.	115
7.12	A schematic showing uniform-layered (A) PU-PAA-MTM3 and (B) PU-PAA-MTM6 nanocomposite, and a (C) hierarchical-layered PU-PAA-MTM6(h) nanocomposite.	116
7.13	Representative stress strain constitutive response of PU-PAA-MTM3, PU-PAA-MTM6 and PU-PAA-MTM6(h) nanocomposites. The dog-bone specimens were loaded at a constant strain rate of 0.005/s at room temperature ($\sim 23^\circ\text{C}$) and a humidity of $\sim 30\%$ until failure.	118
7.14	Comparison of modulus of PU-PAA-MTM3, PU-PAA-MTM6 and PU-PAA-MTM6(h) nanocomposites.	119
7.15	Comparison of yield strength of PU-PAA-MTM3, PU-PAA-MTM6 and PU-PAA-MTM6(h) nanocomposites.	120
7.16	Comparison of ultimate strain-to-failure of PU-PAA-MTM3, PU-PAA-MTM6 and PU-PAA-MTM6(h) nanocomposites.	121
7.17	Representative stress strain constitutive response of PU-PAA-MTM3, PU-PAA-MTM8 and PU-PAA-MTM8(h) nanocomposites.	122
7.18	Representative nominal stress-strain response of polyurea, PU, PU-PAA and PU-PAA-MTM nanocomposites at high impact rate of about 6200 s^{-1} at room temperature ($\sim 23^\circ\text{C}$) and a humidity of $\sim 30\%$. The curves are labeled as (material, strain rate) and a and h in $a(h)$ represents the average volume fraction of MTM nanoparticles and hierarchical-layered nanocomposite.	123
7.19	Representative nominal stress-strain response of polyurea and PU at high impact rates of about 6200 s^{-1} and 7500 s^{-1} at room temperature ($\sim 23^\circ\text{C}$) and a humidity of $\sim 30\%$. The curves are labelled as (material, strain rate).	124
7.20	Comparison of yield strength of polyurea, PU, PU-PAA and PU-PAA-MTM nanocomposites at high impact rates of about 6200 s^{-1} and 7500 s^{-1}	126
7.21	Energy at 0.5 strain for PU, Polyurea, PU-PAA and uniformly and hierarchically layered PU-PAA-MTM nanocomposites.	127
7.22	Residual strain at unloading for Polyurea, PU, PU-PAA and PU-PAA-MTM nanocomposites.	128

8.1 In-plane (E_1 , shown in circles) and out-of-plane (E_2 , shown in triangles) modulus of PU-MTM nanocomposites as a function of volume fraction of MTM nanoparticles. 133

Abstract

Nanoscale control of structure in polymer nanocomposites is critical for their performance but has been difficult to investigate systematically due to the lack of suitable experimental models. This thesis investigated the roles of various structural parameters in finite deformation response of layered polymer-montmorillonite (MTM) clay nanocomposites manufactured using a layer-by-layer (LBL) manufacturing technique. A constitutive model was then developed to predict the uniaxial stress-strain response of the nanocomposites at low strain-rates.

The systematic control over the nano-structure using the LBL method allowed an explicit investigation of the role of parameters like MTM nanoparticle volume fraction, MTM nanoparticle layer separation, MTM nanoparticle layer stratification and the polymer and MTM nanoparticles interfacial interactions. A series of multi-layered polyurethane (PU)-MTM nanocomposites was manufactured, with alternating PU and MTM nano-layers, using the LBL manufacturing technique. The systematic variation in MTM nanoparticle volume fraction was achieved by varying the thickness of the PU nano-layer and therefore the MTM layer separation. Traditional polymer nanocomposite blending techniques result in a wide variation in nanoparticle separation for a given nanocomposite. In this investigation, the MTM nanoparticle layer separation was controlled, which allowed the examination of its effect on the nanocomposite response over a broad range in nanoparticle volume fraction. The PU-MTM nanocomposites demonstrated an increasing yield strength and modulus with increased MTM nanoparticle volume fraction or reduced nanoparticle layer separation. A transition from ductile to brittle behavior in the stress-strain constitu-

tive response was observed at a high volume fraction of MTM nanoparticles. A critical nanoparticle layer separation was found to exist, below which brittle behavior dominated the response of PU-MTM nanocomposites. The MTM layer consisted of stratified layers of MTM nanoparticles which are believed to provide an additional slip mechanism, resulting in an increased ductility in the nanocomposites.

The interface between the polymer matrix and the MTM nanoparticles layers was altered by incorporating a polyacrylic acid (PAA) using an exponential (e)-LBL method. The presence of a stronger interface resulted in an enhanced modulus and strength in the nanocomposites. The e-LBL nanocomposites, at high impact rates in uniaxial compression, demonstrated an increasing modulus, strength and strain-hardening response with increased MTM nanoparticle volume fraction. The presence of MTM nanoparticles led to large strain-gradients during the finite deformation of nanocomposites resulting in an increased strain-hardening response.

A constitutive model was developed to predict the finite deformation response of the PU-MTM nanocomposites. In PU-MTM nanocomposites, the PU matrix in the vicinity of the MTM nanoparticles was modified leading to an interphase region, and its effect on the finite deformation response of these nanocomposites is largely neglected in many existing models. In this work, the nanocomposite volume was assumed to be occupied by multi-layers of bulk PU and effective particles which consisted of MTM layers and the modified PU interphase region. A hyperelastic model was used to capture the large stretch hyperelastic behavior of bulk PU. The effective particle component of the model consisted of a linear elastic spring to capture the initial elastic response, a non-linear viscoplastic dash-pot for the strain-rate dependent yield strength of nanocomposites, and a non-linear spring element in parallel to the dash-pot for the strain-hardening response. The model adopted the concept of amplified strain of the confined PU chains to accommodate the applied strain, owing to the limited strain in the MTM nanoparticles. The constitutive model predicted all the major features of the uniaxial stress-strain constitutive response of

a family of PU-MTM nanocomposites including the initial linear elastic response, yield strength and post yield strain hardening for all volume fractions of MTM nanoparticles, thus confirming the efficacy of the proposed constitutive model.

The research presented in this thesis addresses several issues facing the design of polymer-clay nanocomposites by focussing on the fundamental understanding of the deformation mechanisms in these nanocomposites. The outcome of this investigation included the determination of role of several structural and material properties in controlling their mechanical properties, thus enabling design optimization of materials in terms of tailoring mechanical properties, e.g., stiffness, strength and toughness. The future work entails developing advanced composites that could challenge the existing materials.

Chapter 1

Project Motivation and Outline

Nature, over a million years of evolution, has optimized mechanical design principles to develop advanced materials with superior mechanical properties. Examples of materials that are renowned for their high strength and toughness include seashells, spider silk, teeth, turtle shells, armored fish and many others [1]. Spider dragline silk, for instance, has a tensile strength (per unit weight) five times higher than that of high-grade steel [2]. Moreover, spider silk has a breakage energy per unit weight two orders of magnitude greater than that of steel [3]. Nacre, also known as Mother-of-Pearl, is a naturally occurring composite in sea shells. It is composed of about 95 wt.% inorganic aragonite hexagonal platelets ($CaCO_3$) separated by sheets of organic matrix (5 wt.%) composed of elastic biopolymers (e.g. chitin, lustrin, etc.) organized in a brick-and-mortar architecture that is believed to provide high strength, hardness and toughness to Nacre [4] [5]. With about 5 wt.% of biopolymer, Nacre is twice as hard and 3000 times as tough as its constituent phases [5].

It is interesting to note that most of these advanced natural materials are complex, hierarchical, multilayered nanocomposites in which the smallest building blocks are generally on the nanometer length scale. The thickness of the aragonite platelets in Nacre is around a few nanometers. This is just one example of many in which nature demonstrates a tendency to arrange itself into nanostructures. This observation led to the following universal questions in the mechanics and material science community: why is the nanometer scale

so important to such materials? What underlying mechanisms at the nanoscale are responsible for such advanced properties? Is it possible to produce similar nanomaterials in the laboratory? These questions have motivated the current research, in which we have made an effort to investigate the underlying deformation mechanisms in polymeric nanocomposites reinforced with nanoparticles having size scales below a fraction of a micron. We have prepared these polymer nanocomposites in the laboratory; giving us the flexibility to tune the structural and material parameters according to our requirements. Using experimental and computational tools, it has been successfully demonstrated that on the nanoscale, the mechanical properties of nanoparticles are superior from those on the bulk scale because of decreased size and reduced probability of flaws [6] [7]. We believe that several other design parameters may control the mechanical properties of these nanocomposites in addition to utilizing the superior mechanical properties of nanoparticles. The outcome of the current investigation is an understanding of the role of several structural and material properties that control the mechanical properties of these nanocomposites. This will enable design optimization of materials in terms of tailoring mechanical properties, e.g., stiffness, strength and toughness, and develop artificial nanostructured materials that could potentially compete with the properties of advanced materials found in nature.

In order to understand the behavior of polymer nanocomposites at different loading environments, the objective of this thesis is the understanding of deformation mechanisms in polymer-clay nanocomposites at low and high strain-rates. Chapter 2 introduces the subject of polymer nanocomposites and reviews the current state of deformation mechanisms in polymer-clay nanocomposites. The traditional methods of manufacturing the polymer-clay nanocomposites are discussed and a layer-by-layer manufacturing technique is discussed in detail.

Chapter 3 details the materials, synthesis of polymer-clay nanocomposites and various experimental characterization techniques. The characterization techniques include mechanical, thermal, morphological and structural characterization. Emphasis is placed on

the use of an in-house built tensile tester and an Aluminum split-Hopkinson pressure bar (ASHPB). The tensile tester is used to characterize low-rate mechanical tests in a uniaxial tension deformation state. The ASHPB is used to analyze the impact response of polymer-clay nanocomposites.

Chapter 4 investigates the role of montmorillonite (MTM) clay nanoparticle volume fraction and layer separation in controlling the finite deformation response of polyurethane (PU) - MTM nanocomposites. The effects of volume fraction of MTM nanoparticles on the stiffness and strength of PU-MTM nanocomposites are discussed and analyzed.

Chapter 5 describes the role of stratified layer of MTM nanoparticles on the finite deformation response of PU-MTM nanocomposites. The presence of a slip mechanism in the stratified layer of MTM nanoparticles is detailed in relation to the stiffness, strength and ultimate strain-to-failure of the PU-MTM nanocomposites.

Chapter 6 describes a constitutive model to predict the finite deformation response of PU-MTM nanocomposites, experimentally characterized in Chapter 4. The constitutive model predicts the major features of the constitutive response of PU-MTM nanocomposites at low strain-rates including: the initial elastic response, yield strength and the post-yield strain hardening response, thus confirming the efficacy of the proposed constitutive model.

Chapter 7 introduces an exponential (e)-LBL manufacturing technique to manufacture PU/poly(acrylic acid) (PAA)/MTM nanocomposites. The PU/PAA/MTM nanocomposites are used to investigate the role of interface in controlling the finite deformation response of LBL nanocomposites at low strain-rates. The high strain-rate characterization is performed using the ASHPB in uniaxial compression.

Finally, Chapter 8 briefly summarizes the work presented in this thesis, highlighting the significance of the results obtained and suggesting future efforts in probing polymer nanocomposite deformation mechanisms.

Chapter 2

Background

The ability to tune the properties of polymers has afforded their numerous practical applications ranging from household products to biomedical materials, defense materials and aircraft components. However, for certain applications, the inherent properties of the pristine polymer are not sufficient and are needed to be modified via blending or incorporation of an appropriate material. Examples include thermoplastic olefins (TPO) and polymer composites. A TPO is a blend of a thermoplastic matrix like isotactic polypropylene (iPP), an elastomer like ethylene-propylene-diene monomer (EPDM) and high density polyethylene (HDPE) (Figure 2.1). The elastomer is added to toughen the thermoplastic matrix either by extensive shear yielding [8], by crazing [9] or by a combination of both [10, 11]. HDPE is added in order to improve the miscibility and to reduce the shrinkage mismatch between iPP and elastomers and improve the overall low temperature performance [11]. TPOs have attracted a lot of interest in the Automotive industry due to their potential applications in the interior and exterior parts of an automobile like bumpers, dashboards, etc.

Similarly, the reinforcement of polymers using strong and stiff fillers, resulting in polymer composites, is also common to enhance their mechanical, structural and thermal properties. Carbon fiber is one of the most common fillers used to reinforce polymers [12]. The polymer composites are finding increasing applications in the defense and aerospace industries [13] (Figure 2.2). These materials are light weight compared to the traditionally used metallic materials and thus enable airplanes, spacecrafts to operate with less fuel or

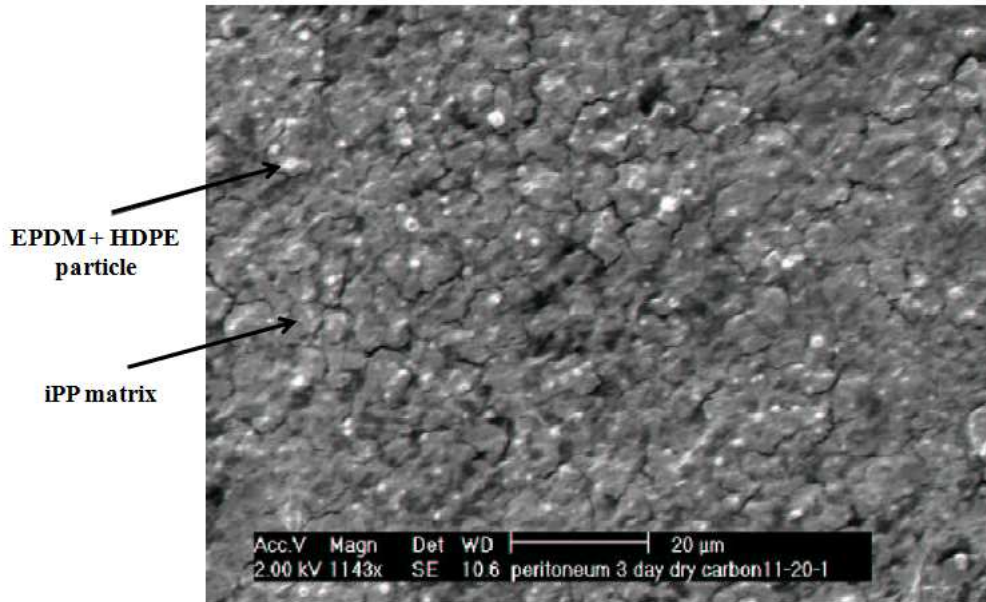


Figure 2.1: A scanning electron micrograph of a thermoplastic olefin[11] .

increased payload [14]. Several strides have been made to use these materials to develop defense materials like light weight body armors. The primary requirements in aerospace and defense materials are high thermal stability and superior mechanical properties. For example, the material required for body armor should specifically possess high impact strength, stiffness and toughness besides being light-weight. With the advent of new technologies, however, the stringent demands on the performance of polymeric materials has increased tremendously. This has led to drive the ongoing development of polymer composite materials, which are multi-functional and utilize the properties of nanoscale building blocks. These materials provide structural integrity, exhibit superior properties than the bulk scale and are found to be more effective owing to less vulnerability to defects [6].

2.1 Polymer Nanocomposites

Polymer composites in which the size of the reinforcement is on the order of nanometers are called polymer nanocomposites. These materials are generally light weight, are often

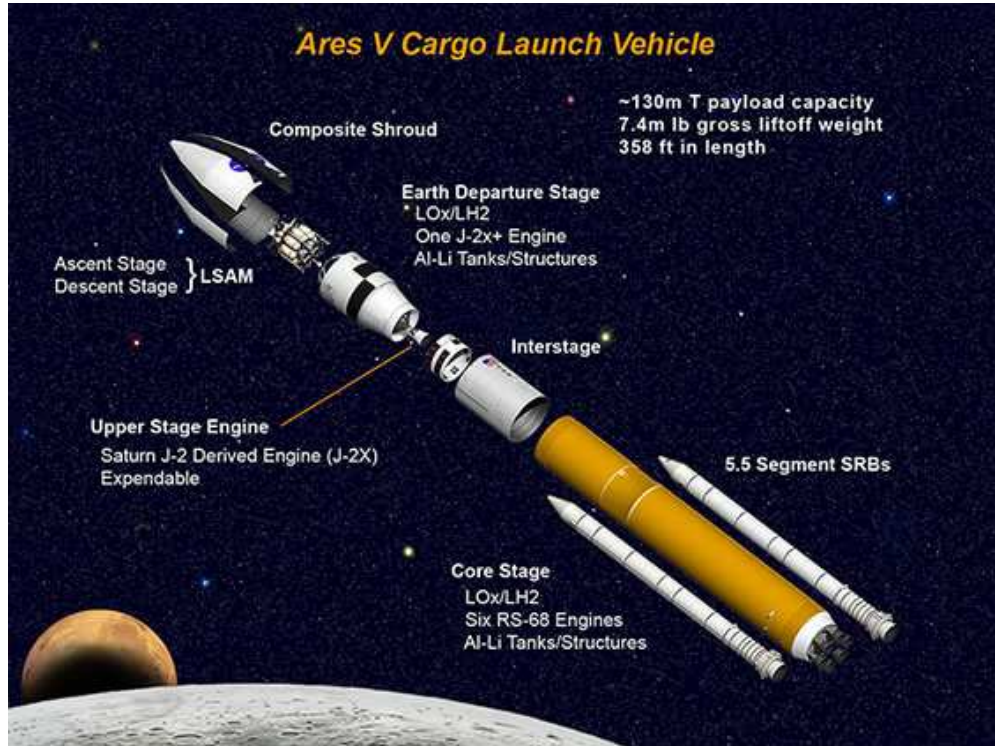


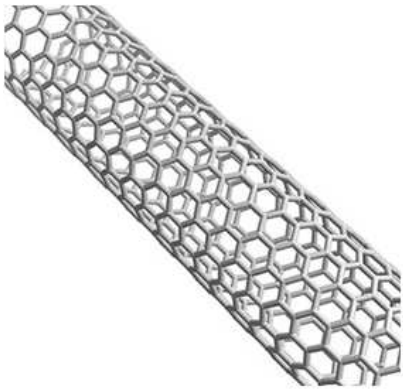
Figure 2.2: An Ares V Cargo Launch Vehicle composed of a composite shroud[13].

easy to process and provide property enhancements extending orders of magnitude beyond those realized with traditional polymer composites. Examples of commonly used reinforcements, often termed nano-fillers, include carbon nanotubes (CNTs) [15–17], layered silicate clay nanoparticles [18–20], cellulose nanocrystals [21], graphite nanoflakes [22–24], etc. These nano-fillers have at least one characteristic dimension on the order of nanometers and can range from isotropic elements to highly anisotropic needle-like or sheet-like elements. While CNTs and cellulose nanocrystals are generally cylindrical in shape, clay nanoparticles are disk-shaped with a high aspect ratio.

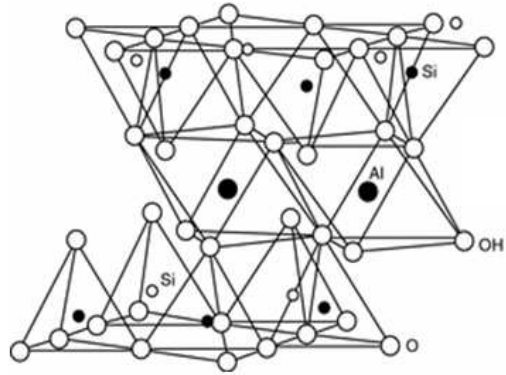
The structures of some of these nano-fillers are shown in Figure 2.3. CNTs, discovered by Sumio Iijima in the early 1990s [25], are primarily rolled graphite sheets, which are composed of millions or more carbon atoms arranged in a hexagonal pattern. CNTs are classified as single walled carbon nanotubes (SWNTs) and multi-walled carbon nan-

otubes (MWNTs). SWNTs are single rolled graphite sheets. MWNTs consist of concentric shells of rolled graphite sheets. While the diameter of an SWNT is typically of the order of 1 – 2 nm with variable length, the diameter of an MWNT can be much larger. The SWNTs have been heralded to be the strongest material on earth with ultimate tensile strengths in the range of 10-300 GPa and Young's modulus of approximately 1,100 GPa. Cellulose nanocrystals, naturally occurring nanofillers, have a Young's modulus of approximately 150 GPa [26, 27]. Other exceptionally strong nano-fillers include graphite flakes and graphene sheets with Young's modulus of 1100 GPa and clay nanosheets with a Young's modulus of 150-300 GPa. Given these exceptional mechanical properties coupled with additional properties originating from nanostructures, there has been increasing interest in incorporating them in polymer matrices to develop high performance multi-functional composites.

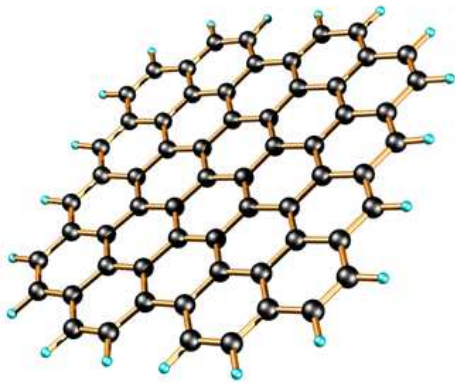
Over the last 2 decades, clay nanoparticles have attracted great interest in academia and industry because of the relatively easy processibility, low cost and fairly predictable stiffening behavior when introduced into polymers [28–32]. A clay nanoparticle is composed of stacked structures of ~ 1 nm thick silicate layers with a variable basal distance. Montmorillonite (MTM), shown in Figure 2.4, is an example of a clay nanoparticle generally used in polymer-clay nanocomposites because it is readily available and has exceptional mechanical properties [33]. The in-plane modulus of elasticity has been estimated to be ~ 270 GPa by Monte Carlo simulations [7]. MTM, a member of the smectite family, is a 2:1 clay, meaning that its crystal structure consists of layers made up of two tetrahedrally coordinated silicon atoms fused to an octahedral sheet of aluminum. Each silicate layer, around 1 nm thick, is regarded as a rigid inorganic polymer consisting of mainly silicon and oxygen, and a small amount of aluminum, magnesium and other metal ions. An alkali metal cation (typically, Na^+) holds the silicate layers together by an intermolecular force. In a polar solvent, such as water, this intermolecular force is broken and the basal distance of the silicate layers expands by solvation of the cation leading to exfoliation of silicate lay-



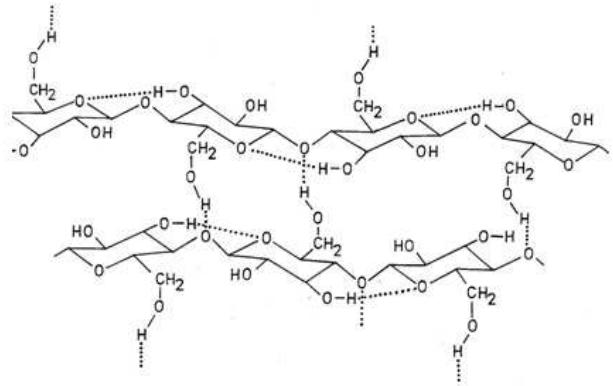
Single-walled carbon nanotube



Layered silicate



Graphene sheet



Cellulose nanocrystals

Figure 2.3: Structures of commonly used nano-fillers.

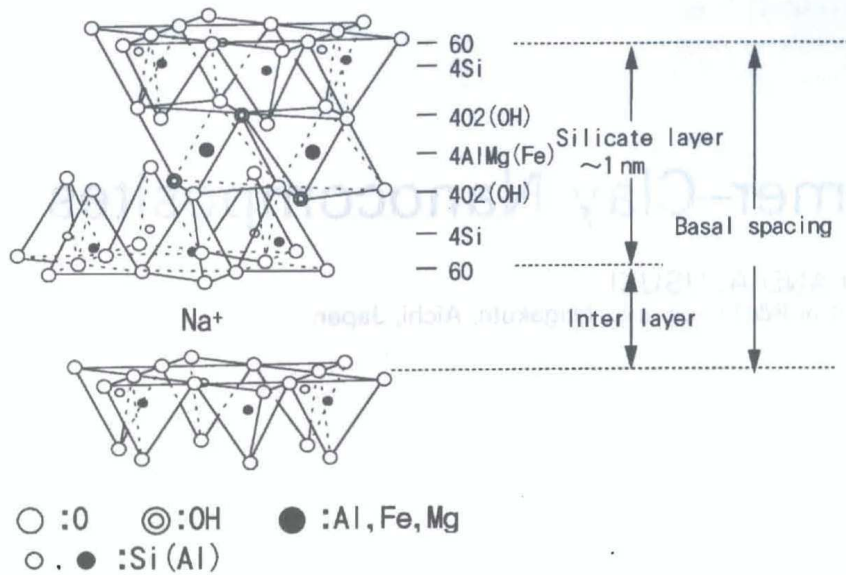


Figure 2.4: Structure of a Montmorillonite clay[33].

ers into individual sheets. The individual sheet of silicate layer contains a negative charge and has an aspect ratio of 100 : 1 to 1000 : 1.

The use of clay nanoparticles as precursors to nanocomposite formation has been extended into various polymer systems including nylon 6 [29, 30, 34, 35]; epoxys [36, 37]; polyamides [38, 39]; polystyrenes [40]; polyurethanes [41–46]; polyolefins such as polypropylene [47–51], polyethylene [52–54]; among others. Although the first clay-reinforced resin known as Bakelite was introduced in early 1900’s, the research on polymer-clay nanocomposites was stimulated by the pioneering work at Toyota. Kojima et al. showed a combined enhancement of modulus, strength and toughness in a Nylon 6-clay nanocomposite [34]. At a loading of 4.2 wt.% (~1.5 v.%) clay, the modulus doubled and the ultimate tensile strength increased more than 50%. These results sparked the research in the nanocomposites area and since then the manufacture of polymer nanocomposites has received much attention both by academics and industry[28–31, 54].

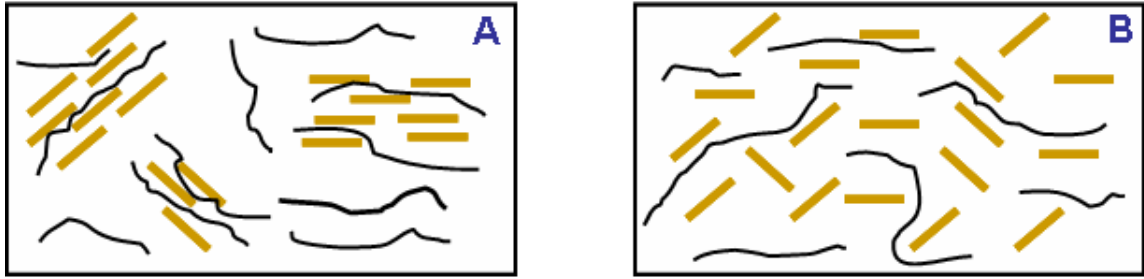


Figure 2.5: Schematic illustrations of the (A) intercalated and (B) exfoliated nanocomposites.

2.2 The State of Deformation Mechanisms in Polymer-Clay Nanocomposites

Polymer-clay nanocomposites represent a relatively new class of hybrid materials that has received widespread interest in the research community [29–31, 36, 41–43, 46, 54, 55]. This interest is fueled by the promise of unprecedented performance, design flexibility and optimization. The mechanical property enhancement in polymer-clay nanocomposites strongly depends on the dispersion of the clay nanoparticles in the polymer matrix and on the effective load transfer from the polymer matrix to the nanoparticles. The dispersion of the clay nanoparticles can be classified as intercalation and exfoliation, as illustrated in Figure 2.5. Intercalated nanocomposites are formed when the polymer chains are inserted into the layered silicate structure with fixed inter-layer spacings. On the other hand, exfoliated nanocomposites are formed when the individual silicate layers are individually dispersed in the polymer matrix.

The key to the successful development of polymer-clay nanocomposites is to achieve complete exfoliation and uniform dispersion of the clay nanoparticles in the polymer matrix. For polymer nanocomposites, strides have been made to incorporate large volume fractions of nano-fillers into various polymer matrices, thereby enhancing their physical, thermal and mechanical properties. However, despite consistent efforts by research groups

world-wide, persistent challenges with poor miscibility and dispersion of nanoparticles especially at high volume fractions have prevented nanocomposites from realizing their full potential. Notwithstanding a decent increase in properties at low volume fractions of clay nanoparticles, most reported nanocomposites exhibit marginally increased or even decreased mechanical properties at high volume fractions [31, 46, 56, 57]. In general, less than ~ 5 v.% of clay nanoparticles can be dispersed uniformly into the polymer matrix [42, 45], beyond which the properties usually begin degrading [46, 57]. This problem is largely related to the difficulty of obtaining well-dispersed large volume fractions of clay nanoparticles and a lack of structural control over the internal organization of the nanocomposites. This is largely due to strong tendency of clay nanoparticles to phase segregate and aggregate above certain concentrations, leading to formation of defects. Following are few of the many examples of nanocomposites in which the mechanical properties tend to degrade at large volume fractions of clay nanoparticles:

Zerda et. al. investigated the mechanical properties of the intercalated epoxy nanocomposites with an increase in the loading of clay nanoparticles [56] (c.f. Figure 2.6). The modulus showed a marginal increase of ~ 1.4 times with 12 wt.% (~ 6 v.%) clay nanoparticles. The tensile strength, however, decreased ~ 0.3 times at the same loading of clay nanoparticles suggesting that the intercalated morphology does not significantly improve the mechanical properties of the system. Similar results were demonstrated for polyurethane-clay systems by Chang et. al. as shown in Figure 2.7 [58]. They attributed the agglomeration of clay nanoparticles above critical points of organoclay contents as the reason for a decrease in ultimate tensile strengths of the nanocomposites. Similarly Tortora et al. showed via scanning electron microscopy results that in a polypropylene-calcium carbonate nanocomposite, the dispersion of calcium carbonate particles changed from a uniform to an aggregated state at ~ 9 v.% of particles (Figure 2.8) [42].

In summary, the uniform dispersion of clay nanoparticles in the polymer matrix has a tremendous positive effect on the mechanical properties of nanocomposites, yet it has

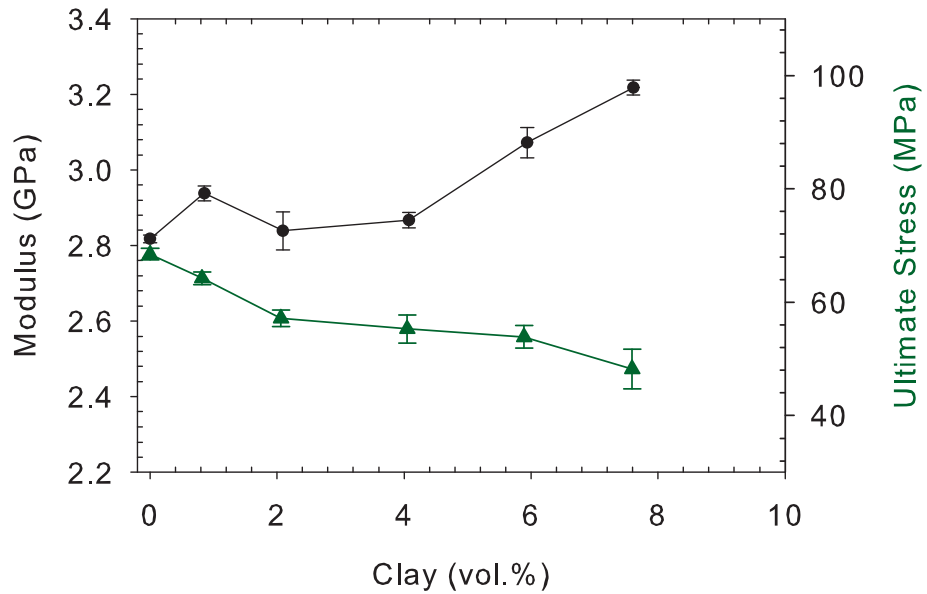


Figure 2.6: Modulus (shown in black circles) and ultimate stress (shown in green triangles) of intercalated epoxy-clay nanocomposites as a function of the clay concentration[56].

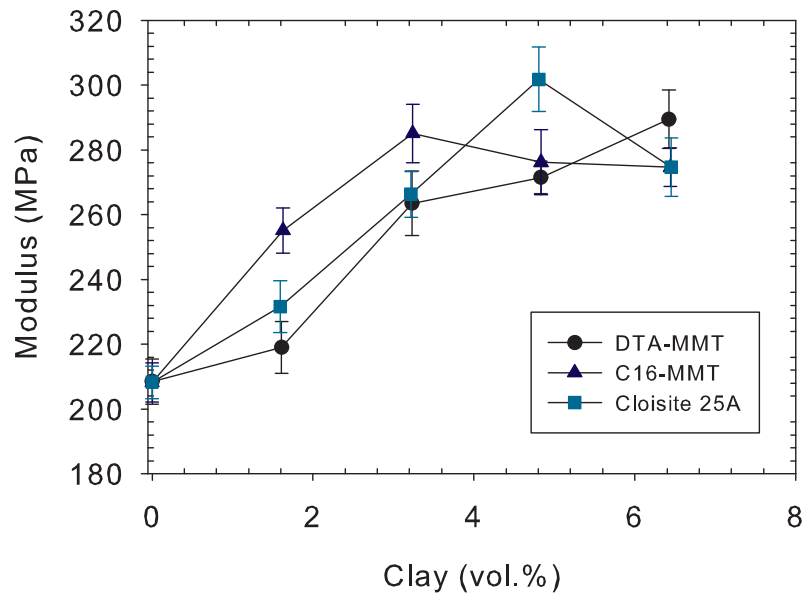


Figure 2.7: Modulus of nanocomposites of polyurethane and various organoclays as a function of clay content[58].

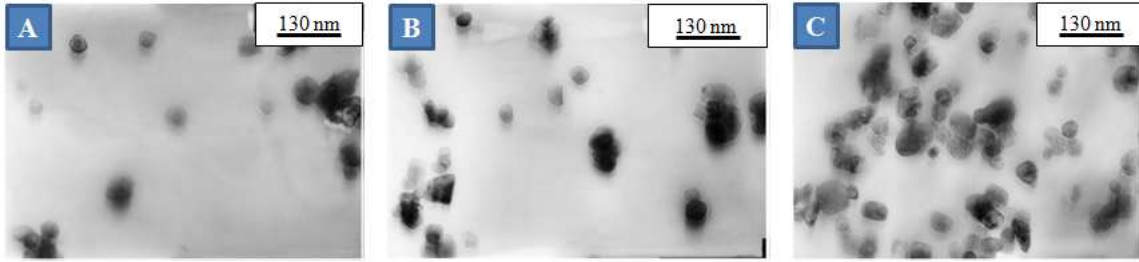


Figure 2.8: Scanning electron microscopy image of polypropylene-calcium carbonate nanocomposites with (A) 5 v.%, (B) 9 v.% and (C) 13 v.% calcium carbonate[42].

proven difficult to disperse these nanoparticles consistently and uniformly. The traditional preparation methods like intercalation of polymer, melt intercalations etc. are simply not capable of fully exploiting the superior properties of clay nanoparticles. Hence, a “smart” nanocomposite preparation method which enables the ability to disperse a wide range of volume fractions of nanoparticles within a polymer matrix while retaining consistent structural organization is crucial to optimally design nanocomposites for their various applications. In this research, we approach the preparation of polymer-clay nanocomposites using a layer-by-layer (LBL) manufacturing technique [59–61]. The striking characteristic of the LBL that separates it from the traditional preparation methods is the unprecedented control it provides over the structure at the nano-scale. It provides the capacity to combine macromolecules that are otherwise difficult or impossible to combine at the level of nanometer scale homogeneity. LBL manufacturing is described, in detail, in the next section.

2.3 Layer-by-Layer Manufacturing

Nanoscale control of structure in polymer nanocomposites is critical for their performance but has been difficult to investigate systematically due to the lack of a suitable experimental model. Layer-by-layer (LBL) manufacturing is one of few techniques which provides unprecedented control over the structure at nanoscale. LBL is currently one of the most dynamic techniques for the preparation of multilayered nanocomposites because of

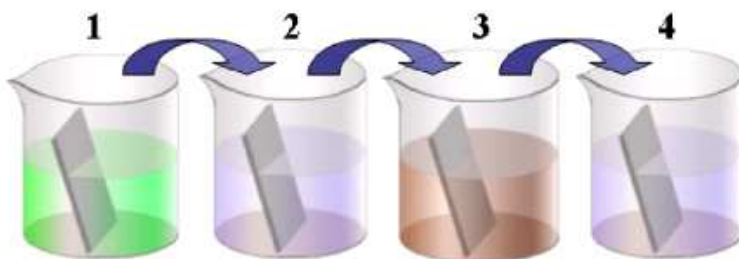


Figure 2.9: Schematic of the LBL manufacturing technique[61]. Deposition cycle includes: (1) deposition of positively charged polyelectrolyte, (2) rinsing with a polar solvent, (3) deposition of negatively charged polyelectrolyte, and (4) rinsing with a polar solvent.

its versatility, simplicity and robustness besides its nano-structural controllability. The versatility of LBL manufacturing was first realized by Decher and co-workers in the early 1990s [60]. LBL is basically a sequential deposition of oppositely charged polymers onto a surface to form a multi-layered material. Besides polymers, this technique has been successfully applied to many other materials including nanoparticles [62], nanotubes and nanowires [63], clay nanoplatelets [64], proteins [65, 66], DNA [59], dyes [67] and viruses [68, 69]. The LBL assembly generally consists of the steps of deposition, rinsing and drying. A schematic of a typical LBL deposition cycle is shown in Figure 2.9.

A charged substrate is first immersed into a solution of a oppositely charged polyelectrolyte (step 1). The oppositely charged polyelectrolyte, thus, covers a large area of the substrate and forms a charged layer on the surface for subsequent deposition of other materials. The substrate is then rinsed with pure solvent like de-ionized water to remove the weakly bound material (step 2). This rinsing step is followed by immersion in the oppositely charged solution to that used in step 1 (step 3). This step is again followed by rinsing with pure solvent (step 4). The rinsing steps are followed by drying, if desired, with compressed air to remove excess water (not shown in Figure 2.9). Each deposition cycle, consisting of steps 1-4, resulted in the deposition of a bilayer. Due to the molecular nature of the layers deposited in each cycle, the LBL manufacturing technique affords nanometer

scale precision in the thin film thickness. With the recovery of the surface charge, the deposition cycle can be repeated as many times as required to build a multi-layered nanocomposite of desired thickness. There seems to be no limitation to the maximum number of layers that can be deposited; films with up to 1000 layers have been assembled [70, 71]. Once the desired thickness of the nanocomposite is manufactured, the free-standing films are separated from the substrate using hydrofluoric acid (HF) [72].

Although the primary source of interaction in an LBL is electrostatic, other types of interactions can also be used in the LBL assembly. Stockton and Rubner successfully demonstrated the LBL assembly of poly(aniline) (PAn) with nonionic water-soluble polymers such as poly(vinyl pyrrolidone), poly(vinyl alcohol) and poly(ethylene oxide) [73]. The presence of hydrogen bonding interactions between PAn and the nonionic polymers was identified using infrared spectroscopy. Other LBL assemblies, especially in protein components, have also been reported that utilize interactions other than electrostatic [74–76].

2.4 Purpose and Research Overview

The previous sections provided a brief account of the traditional polymer nanocomposites and the LBL deposition method. The unprecedented control of the structure at the nanoscale using LBL assembly was also emphasized. The goal of the present thesis work is to investigate the deformation mechanisms in polymer-clay nanocomposites. In view of this, nanoscale control of structure is vital to understanding the roles of various design parameters in controlling the finite deformation response of polymer nanocomposites.

This work focuses on the development and investigation of inherent deformation mechanisms in polymer-clay nanocomposites. The nanocomposites are prepared using the LBL assembly method for several reasons. First, recent advances in the manufacturing of polymer nanocomposites using LBL manufacturing have resulted in unprecedented control over structure at nanoscale. The LBL system offers the potential to conduct well-controlled

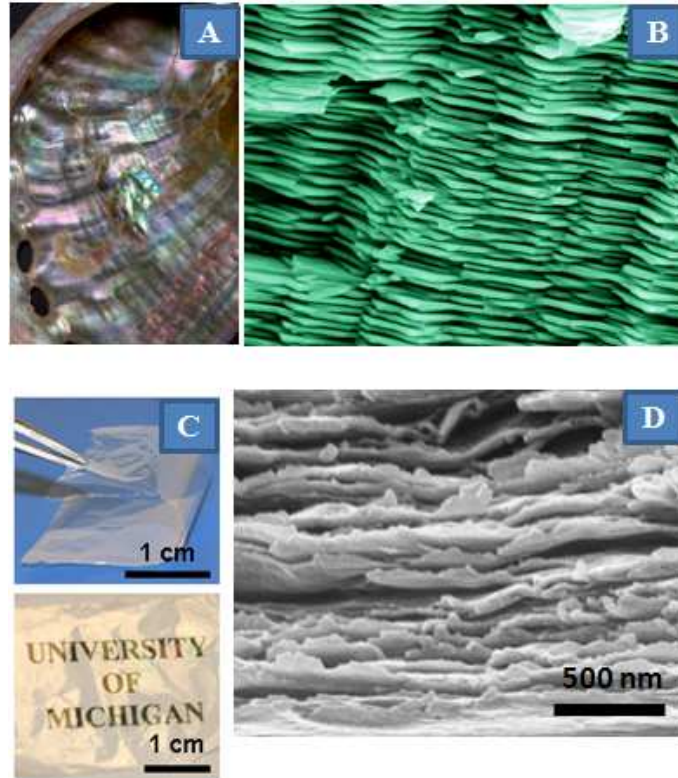


Figure 2.10: (A) Photograph of a sea-shell, (B) Microstructure of Nacre[77], (C) Photograph of a poly(vinyl alcohol)-montmorillonite clay[55], and (D) Scanning electron microscope image of the cross-section of a 300-bilayer poly(vinyl alcohol)-montmorillonite nanocomposite[55].

experiments to examine deformation mechanisms in the reinforced polymers. Moreover, these nanocomposites have been fashioned to structurally resemble the morphology of the very tough biocomposite shell, Nacre [77]. This is shown in Figure 2.10. Figure 2.10 (B) shows the brick-and-mortar microstructure of Nacre and Figure 2.10 (D) shows the cross-section of a 300-bilayer poly(vinyl alcohol)-montmorillonite clay nanocomposite [55].

The research presented in this work can be generally divided into two main themes: the experimental investigation of deformation mechanisms in polymer-clay nanocomposites and development of a constitutive model to predict the finite deformation response at low strain-rates. We initiate our research by investigating the capability of the LBL manufacturing technique to uniformly disperse large volume fractions of clay nanoparticles in a

polymer matrix. Once this investigation is established, we systematically develop a series of multi-layered polymer-clay nanocomposites with a consistent uniform dispersion and wide range of volume fractions of clay nanoparticles. This development enables the investigation of the role of structural parameters in controlling the deformation mechanisms in polymer-clay nanocomposites.

2.5 Ultrastrong and Stiff PVA-MTM Nanocomposite

Previous work in our research group involved an investigation of the capability of LBL assembly to systematically and uniformly reinforce large volume fractions (~ 50 v.%) of MTM nanoparticles in a PVA matrix [55]. More information about the PVA and MTM used and the experimental techniques can be found in the experimental section of this thesis or elsewhere [55].

The characterization of PVA-MTM nanocomposites using atomic force microscopy verified the planar orientation and dense coverage of MTM nanoparticles in the PVA matrix (Figure 2.11). The linear growth in the film thickness as a function of bilayers as revealed by Ellipsometry studies is shown in Figure 2.12.

The PVA-MTM nanocomposite with 50 v.% MTM nanoparticles demonstrated remarkable mechanical properties over pure PVA when tested in tension using the Tensile Tester (refer Chapter 3) at a strain rate of 0.005/s. Figure 2.13 shows the nominal stress-strain curves and Table 1 summarizes the mechanical properties of the PVA and the PVA-MTM nanocomposite. The nanocomposite displayed ~ 10 times higher ultimate tensile strength (400 ± 40) and nearly two orders of magnitude higher modulus (106.0 ± 11 GPa) when compared with pure PVA. For comparison, the modulus of the nanocomposite is comparable to that of various grades of Kevlar i.e. 80-220 GPa [78–80] and exceeds the stiffness of the strongest CNT-based nanocomposites [81]. The inclusion of ~ 50 v.% MTM nanoparticles, however, decreased the ultimate strain to failure of the nanocomposite by 99% as compared to the pure PVA, resulting in a brittle nanocomposite with a strain to failure of

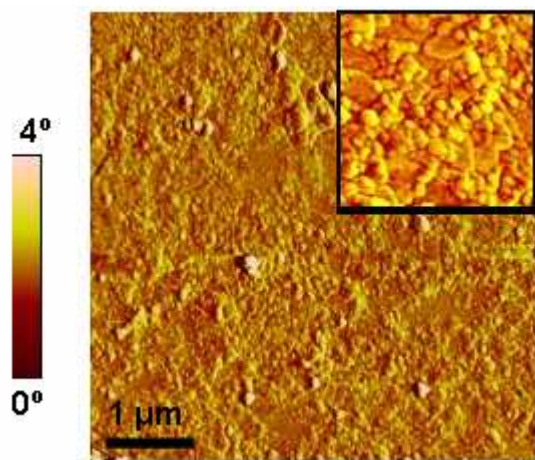


Figure 2.11: An AFM phase image of a single PVA-MTM bilayer adsorbed on top of a silicon wafer. The inset shows the close up of the main image showing individual MTM platelets more clearly[55].

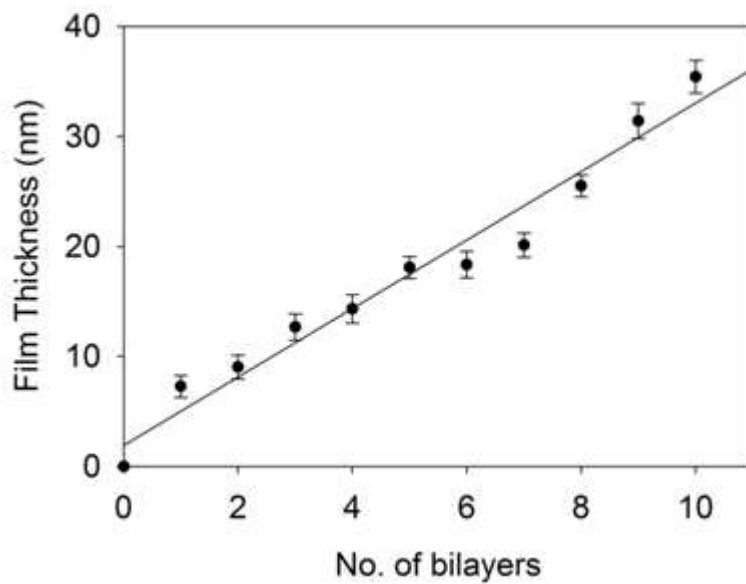


Figure 2.12: Thickness results for PVA-MTM nanocomposite for the first 10 deposition cycles from ellipsometry[55].

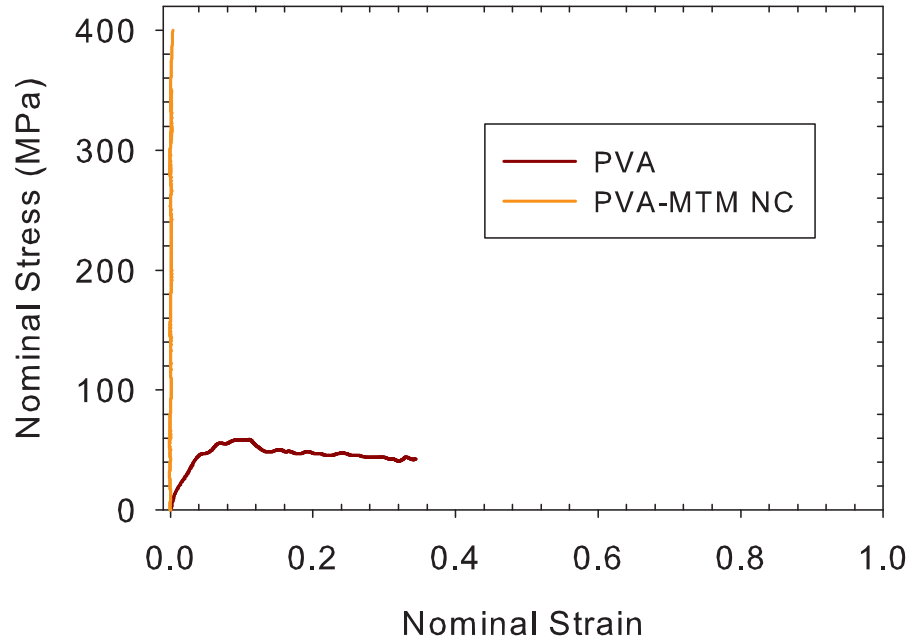


Figure 2.13: Representative nominal stress-strain constitutive response of PVA and PVA-MTM nanocomposite with 50 v.% MTM nanoparticles[55]. The dog-bone specimens were loaded at a constant strain rate of 0.005/s at room temperature ($\sim 23^\circ\text{C}$) and a humidity of $\sim 30\%$ until failure.

0.0033 ± 0.0004 .

A theoretical analysis using the rule of mixtures is employed to estimate the properties of PVA-MTM nanocomposite with ~ 50 v.% of MTM nanoparticles. The upper bound rule of mixtures equation gives the following for the modulus of the nanocomposite:

$$E_c = v_f E_f + (1 - v_f) E_m \quad (2.1)$$

where E_c is the modulus of the nanocomposite, E_m is the modulus of PVA, E_f is the modulus of MTM nanoparticles, v_f is the volume fraction of MTM nanoparticles in a PVA-MTM nanocomposite. Applying this equation to determine the modulus of 50 v.% PVA-MTM nanocomposite gives a modulus of 135 GPa. The modulus of ~ 50 v.% PVA-

MTM nanocomposite (106.0 ± 11) is close to the upper bound for composites. These enhancements in the mechanical properties can be explained via effective stiffening of the PVA matrix. The PVA matrix was highly constrained and effectively stiffened because of its close proximity to the MTM nanoparticles. This was evident from the differential scanning calorimetry (DSC) study shown in Figure 2.14. Figure 2.14 shows a sharp and well-defined endothermic melting peak at $T_m \sim 225^\circ\text{C}$. The PVA-MTM nanocomposite shows a strong suppression and broadening of this peak suggesting constrained thermal motions in the PVA matrix in the nanocomposite.

Besides the effective stiffening of PVA by MTM nanoparticles, the enhancement of modulus and ultimate tensile strength was also due to the presence of enhanced interactions that led to an efficient load transfer between PVA and MTM nanoparticles. These interactions included epitaxial hydrogen bonding between PVA and MTM nanoparticles, and the effective cross-linking by glutaraldehyde that formed covalent acetal bridges between $-OH$ groups of the PVA chains as well as the hydroxyl groups present on the MTM nanoparticles. Detailed information about these interactions can be found in [55] and [82].

A similar suppression of polymer motion was also observed in Nacre. Figure 2.15 compares the DSC traces of Nacre vs. the protein present in it, i.e., chitin. Here also, the well-defined peak of chitin at a temperature of $\sim 77^\circ\text{C}$ was suppressed in Nacre because of the presence of 95 wt.% of the inorganic aragonite hexagonal platelets in Nacre.

Here, we have demonstrated that it is possible to systematically and uniformly disperse large volume fractions of nanoparticles in a polymer matrix using the LBL manufacturing technique. We have demonstrated that reinforcement in polymer-nanoparticle systems such as PVA-MTM is a result of several mechanisms operating at the nanoscale. The incorporation of these reinforcing mechanisms along with the degree of structural organization afforded by LBL assembly enabled the preparation of a nanocomposite that reaches mechanical properties close to the upper bound formulation. In the subsequent sections, we will utilize these qualities of the LBL process to investigate the deformation mechanisms in

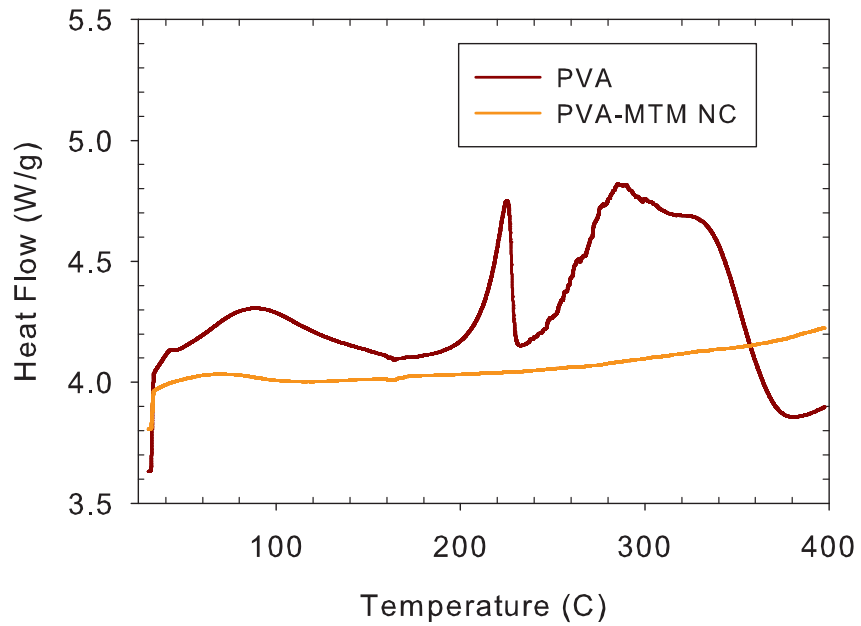


Figure 2.14: Differential scanning calorimetry analysis results for PVA and PVA-MTM nanocomposite with 50 v.% MTM nanoparticles[55].

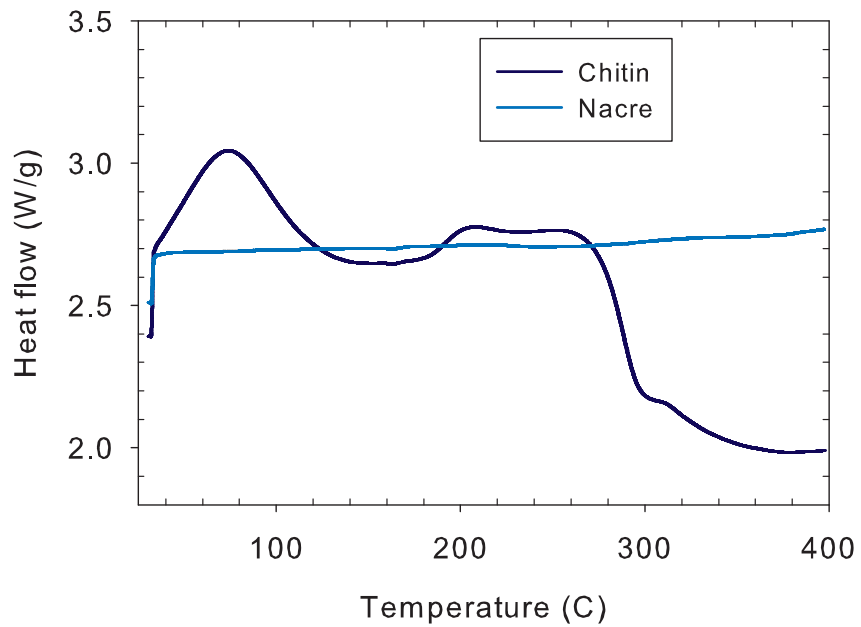


Figure 2.15: Differential scanning calorimetry analysis results for Chitin and Nacre.

polymer-clay nanocomposites. We will demonstrate the role of various structural parameters in controlling the finite deformation mechanisms in polymer-clay nanocomposites and focus on addressing the issues facing the design of optimum nanocomposite systems.

Chapter 3

Experimental Details

3.1 Materials

Poly(vinyl alcohol) PVA with molecular weight of 70,000 was purchased from Sigma-Aldrich (St. Louis, MO) and was used as received. 1 wt.% PVA solution used for the preparation of LBL nanocomposites was prepared by dissolving 10 g of PVA powder in 1 L of 18 M Ω cm^{-1} , pH = 5.6 de-ionized water under vigorous stirring. Poly(acrylic acid) (PAA) with a concentration of 35 wt.% and molecular weight of 60,000 was also purchased from Sigma-Aldrich. A semi-transparent cationic Polyurethane (PU) dispersion with a specific gravity of 1.02 g/cm³ (at 25 °C) was obtained from HEPCE CHEM Co. Ltd. (Kyungki-Do, Korea). The PU was prepared from Isophorene Diisocyanate (IPDI), Polytetra Ethylene Glycol (PTMG) and 3-Diethylamine-1,2-Propanediol (DEAPD). Ethylene di-amine was added as a chain extender. The concentration and molecular weight of as-received PU was 35 wt.% and 90,000 respectively. Various concentrations of PU were prepared by adding the required amount of 18 M Ω cm^{-1} , pH = 5.6 de-ionized water to it and stirring before use. Nacre shells, in the form of oysters, were purchased from Real Sea Food Company (Ann Arbor, MI). Chitosan powder, with an average molecular weight of 5,000, was purchased from Sigma-Aldrich. Polyurea used for high strain-rate investigations was purchased from Air Products and Chemicals Inc. (Allentown, PA).

Na^+ -Montmorillonite (MTM) (Cloisite Na^+) clay with a specific gravity of 2.86 g/cm³

was purchased from Southern Clay Products (Gonzales, TX). The as-received MTM nanoparticles were disk-like elements of thin silicate layers, 1 nm thick and ranging in diameter from 100-1000 nm, the average diameter being 110 nm as described by the manufacturer. A 0.5 wt.% dispersion of MTM nanoparticles was used for the preparation of nanocomposites. 5g of the as-received MTM clay was dissolved in 1L of 18 M Ω cm⁻¹, pH = 5.6 de-ionized water under vigorous stirring for one week. This resulted in the exfoliation of clay into silicate layers due to the solvation of Na⁺ cations holding them together (refer Figure 2.4) [83]. After one week, the insoluble fraction was allowed to precipitate and the supernatant was collected.

Nanocomposites were prepared on 25mm X 75mm microscope glass slides obtained from Fisher Scientific (Waltham, MA). Hydrogen peroxide and concentrated sulfuric acid used for cleaning the glass slides were purchased from Sigma-Aldrich (St. Louis, MO). 1 v.% concentrated hydrofluoric acid (Sigma-Aldrich), prepared by appropriately diluting with de-ionized water, was used for detaching the nanocomposite films from the glass slides. Isopropanol, A.C.S. grade, used for the treatment of PU-MTM nanocomposite films, was also purchased from Sigma-Aldrich. Glutaraldehyde, used for the treatment of PVA-MTM nanocomposites was purchased from Fluka (currently part of Sigma-Aldrich). 5 v.% glutaraldehyde solution was prepared by diluting the stock solution with de-ionized water prior to use.

3.2 Synthesis of Nanocomposites

Pure PU films were casted from the as-received dispersion by diluting with the de-ionized water and drying overnight in an oven at a temperature of ~ 80 °C.

The nanocomposites were synthesized using layer-by-layer (LBL) manufacturing [59–61, 84]. While several modifications of LBL techniques have been proposed, the linear-LBL and exponential-LBL (e-LBL) synthesis techniques have been utilized to fabricate multi-layered polymer-clay nanocomposites in this research work.

3.2.1 Linear LBL Nanocomposites

The synthesis sequence of polymer-clay nanocomposites using the linear LBL method is illustrated in Figure 2.9. A microscopic glass substrate was first immersed into a solution of polymer leading to deposition of a nano-layer of the polymer on the glass slide (step 1). The glass substrate was then rinsed with de-ionized water to remove the excess material (step 2). The rinsing step was followed by immersion in the clay dispersion (step 3), resulting in deposition of a nano-layer of clay nanoparticles on the PU nano-layer. This step was again followed by rinsing with de-ionized water (step 4). The rinsing steps were followed by drying with compressed air to remove excess water. Each deposition cycle, consisting of steps 1-4, resulted in the deposition of a nanocomposite bilayer. The deposition cycle can be repeated as many times as required to build a multi-layered nanocomposite of desired thickness. The preparation of the nanocomposites was accomplished using a StratoSequence IV, a robotic dipping machine, from Nanostrata Inc. (Tallahassee, FA).

PVA-MTM nanocomposites were fabricated by immersion of the glass substrate in 1 wt.% solution of PVA, for 5 min, rinsing with de-ionized water for 2 min, drying with compressed air for 1 minute, immersion in 0.5 wt.% MTM dispersion for 5 min, followed by rinsing with de-ionized water and drying by compressed air for 2 min and 1 minute respectively. After the synthesis of every 10 bilayers until 300 bilayers, the substrate was immersed into the 5 v.% solution of glutaraldehyde for 30 min to allow for cross-linking. The 300-bilayer nanocomposite films were separated from the microscopic glass slide using HF [72]. The free-standing films were then dried in a drying oven at 60 °C and then set aside to equilibrate in ambient conditions ($\sim 23^\circ\text{C}$ temperature and $\sim 30\%$ humidity) prior to characterization.

In the preparation of PU-MTM nanocomposites, the glass substrate was alternately immersed in PU and 0.5 wt.% MTM dispersion. The immersion time in the PU and MTM nanoparticles dispersion was 5 min; the rinsing and drying times were 2 min and 1 min respectively. In a typical PU-MTM nanocomposite fabrication, the deposition cycle was

repeated 300 times to produce 300-bilayer nanocomposites. The 300-bilayer nanocomposites were separated from the microscopic glass slide using HF. The free-standing nanocomposite films were then treated overnight with isopropanol followed by drying in an oven at 60 °C and then set aside to equilibrate in ambient conditions (~ 23 °C temperature and $\sim 30\%$ humidity) prior to characterization. The loading of MTM nanoparticles was varied in the PU-MTM nanocomposites by varying the dilution of the PU in the LBL manufacturing process. The PU was diluted using de-ionized water to 3 to 75 times the as-received concentration to manufacture PU-MTM nanocomposites with various loadings of MTM nanoparticles. For example, a 50 times dilution was prepared by diluting 10 ml of the as-received PU with 490 ml of the de-ionized water.

3.2.2 Exponential-LBL Nanocomposites

PU-PAA and PU-PAA-MTM nanocomposites were manufactured via the e-LBL manufacturing technique. In the PU-PAA nanocomposite fabrication, the glass substrate was immersed in the PU solution for 30 sec, rinsed with de-ionized water for 2 min, immersed in PAA solution for 30 sec and again rinsed with water for 2 min. For the PU-PAA fabrication, PU was diluted to 10 times the as-received concentration.

The PU-PAA-MTM nanocomposites were manufactured depending on their deposition sequence. Uniform layered PU-PAA-MTM nanocomposites with a deposition sequence of PU/PAA/PU/MTM were manufactured by immersing the glass substrate in PU solution for 30 sec, rinsing with de-ionized water for 2 min, immersing in PAA solution for 30 sec, rinsing with de-ionized water for 2 min, immersing in PU solution again for 30 sec, again rinsing with water for 2 min, immersing in MTM dispersion for 1 min followed by rinsing with de-ionized water for 2 min. The loading of MTM nanoparticles was varied in the PU-MTM nanocomposites by varying the dilution of the PU in the LBL manufacturing process. The PU was diluted to 10 to 40 times the as-received concentration to manufacture PU-MTM nanocomposites with various loadings of MTM nanoparticles.

Hierarchical-layered PU-PAA-MTM with a deposition sequence of PU/PAA/(PU/MTM)_{*n*} were manufactured by immersing the glass substrate in PU solution for 30 sec, rinsing with de-ionized water for 2 min, immersing in PAA solution for 30 sec, rinsing with de-ionized water for 2 min, followed by repeating this sequence *n* times: immersing in PU solution again for 30 sec, again rinsing with water for 2 min, immersing in MTM dispersion for 1 min followed by rinsing with de-ionized water for 2 min. For the hierarchical-layered nanocomposites, PU was diluted to 10 times the as-received concentration.

The e-LBL nanocomposite films were separated from the microscopic glass slide using HF and the free-standing films were further dried in a drying oven at 60 °C and then set aside to equilibrate in ambient conditions (~ 23 °C temperature and $\sim 30\%$ humidity) prior to characterization. A Midas II automatic slide stainer was used to manufacture the e-LBL nanocomposites.

3.3 Consolidation of Thin Films

Some nanocomposite films, primarily e-LBL nanocomposites, exhibited non-uniform thickness and required consolidation after formation and removal from the glass substrates. The consolidation process was accomplished using a hot-press. The hot-press was unloaded and pre-heated to a temperature of ~ 110 °C. The sample required for consolidation was carefully placed within the hot plates of the press. Ceramic plates coated with teflon sheets were used to reduce friction and sticking of sample to the ceramic plates. For the preparation of consolidated stack to characterize the e-LBL nanocomposites in high strain-rate compression, the films were stacked on top of each other. Once the sample was placed, a pressure of ~ 15 MPa was applied for 30 min, after which the sample was allowed to cool down to room temperature. The consolidation process is depicted in Figure 3.1 [85]. The applied pressure and temperature represent the optimal conditions to enable the successful consolidation of films. Below 110 °C, there was no consolidation and the films were easily peeled apart, and above 120 °C, the consolidated stacks showed signs of de-

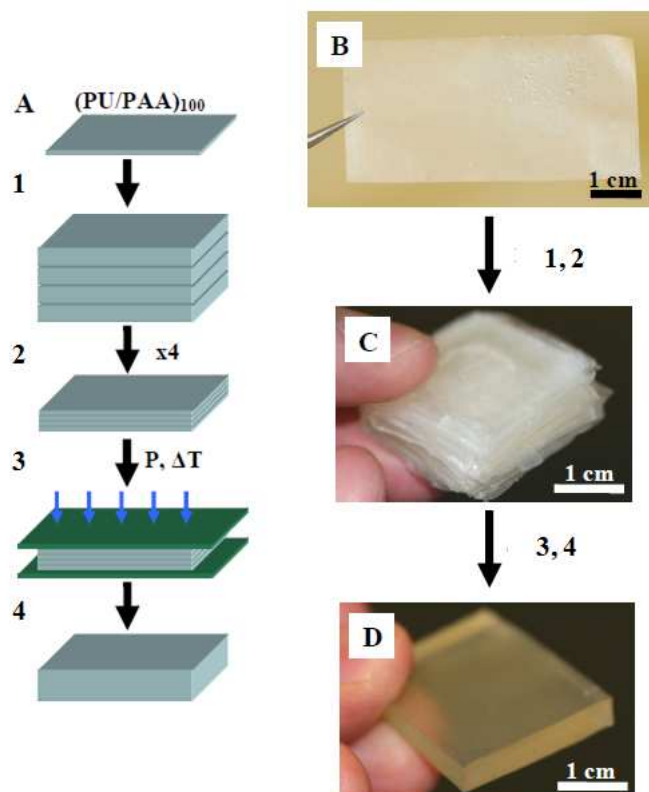


Figure 3.1: Schematic of consolidation of free-standing e-LBL films. (A) Consolidation procedure: (1) The films were taken and (2) stacked together into a sandwich structure to achieve conformal overlap, (3) the stack is hot-pressed at < 15 MPa pressure and 110°C , (4) final consolidated stack. (B) Photograph of a free-standing, 100-bilayer PU-PAA film. (C) Photograph of 100 100-bilayer free-standing films combined into a stack. (D) Photograph of a final hot-pressed stack.[85]

composition. Successful consolidation resulted in a homogenous and transparent material, indicating that the hot-pressing procedure removed the defects such as water molecules and voids originating from the e-LBL assembly.

3.4 Sonication of MTM nanoparticles

The sonication of MTM nanoparticles was required to separate the stacked silicate sheets in the stirred MTM solution. 0.5 wt.% MTM dispersion was sonicated at a frequency of 40 KHz for 5 hours using a VWR ultrasonic cleaner.

Material	Density (g/cm ³)
PVA	1.20
PU	1.02
PAA	1.05
MTM	2.96

Table 3.1: Densities of polymers and MTM clay used in the present work.

3.5 Characterization

3.5.1 Thermogravimetric Analysis

The volume fraction of MTM nanoparticles in the nanocomposites was determined using a Thermogravimetric Analyzer (TGA) Pyris 1 from Perkin Elmer (Waltham, MA). Samples with weights ranging from 0.1 to 0.5 mg were heated at a temperature rate of 10 °C/min and to a final temperature of 1000 °C while being purged with air at a flow rate of 20 mL/min. Sample weight was recorded as a function of temperature. The MTM volume fraction was determined by measuring the loss in nanocomposite sample weight with temperature as compared to that of the pure polymer sample. The polymer burnt off completely after a certain temperature and the remaining weight was used to determine the weight fraction of MTM nanoparticles. The measured weight fraction was converted to the volume fraction by the following formula [86]:

$$v_c = \frac{w_c \rho_p}{\rho_c(1 - w_c) + w_c \rho_p} \quad (3.1)$$

where v_c is the volume fraction of MTM nanoparticles, w_c is the weight fraction of MTM nanoparticles obtained from TGA and ρ_c and ρ_p are the densities of MTM clay and polymer respectively. The densities of polymers and MTM clay used in the present work are shown in Table 3.1. The data are represented as mean \pm SD, each of them determined from three different samples.

3.5.2 Wide Angle X-ray Diffraction

The morphological characterization of bulk polymer, nanocomposites and MTM clay was performed using a rotaflex Cu K α rotating anode diffractometer ($\lambda = 1.54\text{\AA}$). Samples were tested on the surface perpendicular to the thickness direction and were scanned from 3° to 35° at a scanning rate of $3^\circ/\text{min}$ with a sampling interval of 0.05° . The detector and sample rotated simultaneously such that the angle between the beam and the sample surface was the same as the angle between the sample surface and the detector.

3.5.3 Scanning Electron Microscopy

The thickness of the PU-MTM nanocomposites was determined using a FEI Nova Nanolab dual-beam FIB and scanning electron microscope (SEM). Because of the non-conductive nature of the PU-MTM nanocomposites, a few nanometers thick layer of gold was sputtered onto their cross-sections prior to imaging. The thicknesses are represented as mean \pm SD, each of them determined from at least three different samples. The average bilayer thickness was determined by dividing the mean value of nanocomposite thickness by its number of bilayers.

3.5.4 Low Strain-rate Mechanical Testing

Mechanical characterization was performed using an in-house designed tensile tester shown in Figure 3.2[87]. The tensile tester was built around a Nikon SMZ 800 dissecting microscope that was fitted with a Basler A102fc digital video camera. Dual actuators were driven by MicroMo stepper motors and mounted on Del-Tron crossed roller slides that enabled the specimen to stay in the center of view. Grips were machined out of stainless steel and placed at the interior ends of both actuators. The axial motors were controlled using LAB-VIEW software on a Dell Precision 300 pc which also synchronized data acquisition from the load element with image acquisition from the digital camera.

The dog bone specimens were loaded at constant low strain-rates at room temperature

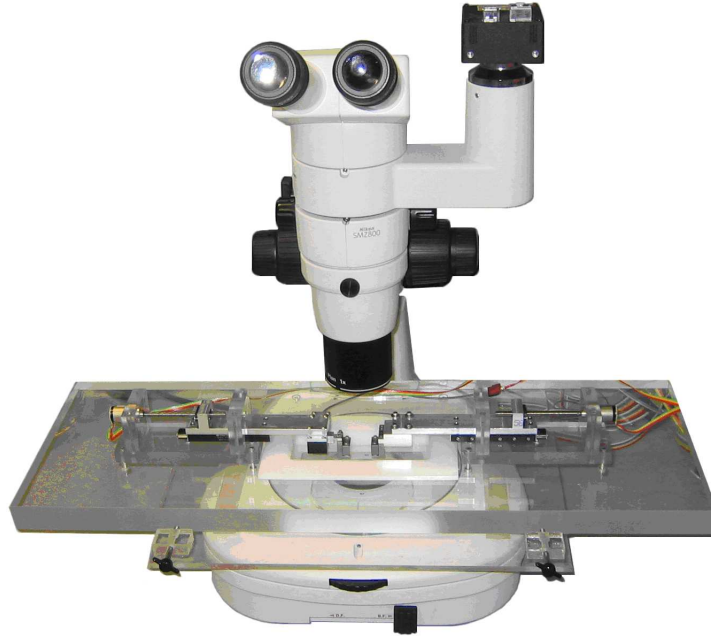


Figure 3.2: A custom-designed tensile tester to measure the mechanical properties of polymers and polymer-clay nanocomposites at low strain rates.

($\sim 23^\circ\text{C}$) and humidity of $\sim 30\%$ until failure and the synchronized voltage and image recordings were compiled using LABVIEW. The voltage was converted to force data using a calibration equation relating the force with the registered voltage. Load cell was calibrated every day the tests were performed. The calibration was performed by monitoring the change in voltage over a range of known weights. One such calibration curve is shown in Figure 3.3. Analysis of actual material strain was achieved by adhering $25\ \mu\text{m}$ diameter microspheres on the specimen surface. The specimen images were analyzed with Metamorph software from Meta Imaging to track the micro-sphere positions (c.f. Figure 3.4). At least 3 dog-bone specimens with a gauge length of $\sim 7\ \text{mm}$ and width of $\sim 1\ \text{mm}$ were tested in order to produce each representative stress-strain curve. The raw force vs. image data were converted to nominal stress (force/cross-section area) vs. nominal strain data (change in separation of microspheres/initial separation). Modulus was determined by calculating the initial slope of the nominal stress vs. nominal strain data. At least 3 dog-bone

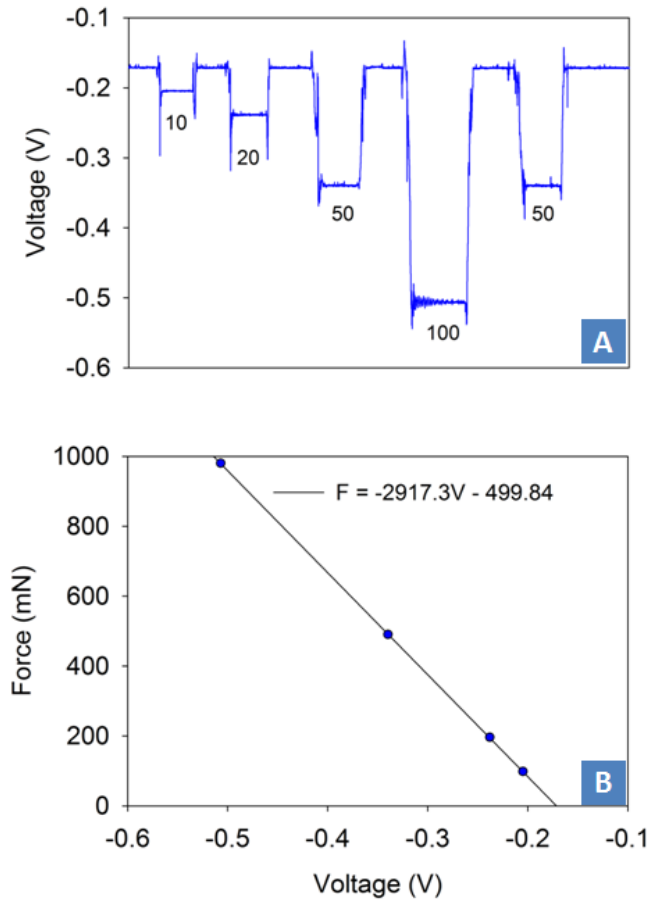


Figure 3.3: (A) A sample voltage calibration curve for a load cell used in the tensile tester. Numbers indicate weights in grams. (B) Force-voltage calibration curve for the load cell.

specimens were tested in order to produce each representative stress-strain curve. The gage section of the dog bone specimens deformed homogeneously with no predominant necking phenomena. The true stress-strain representative curves were determined as true stress = nominal stress(1 + nominal strain) and true strain = $\ln(1 + \text{nominal strain})$ [88].

3.5.5 High Strain-Rate Mechanical Testing

Mechanical characterization at high-strain rates was performed using an in-house designed and built aluminum split-Hopkinson pressure bar (ASHPB) apparatus [11, 89]. The design, setup, data processing and one-wave theory for the ASHPB is well established in [11]

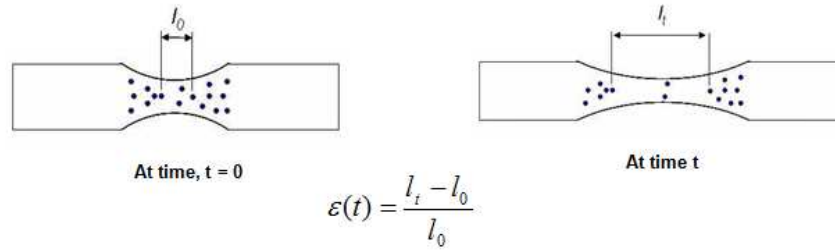


Figure 3.4: A schematic illustrating the determination of material strain in the specimens.

and [90]. These aspects have been briefly described here for completeness. In order to design an SHPB for polymeric materials, special care needs to be taken to minimize the geometrical and friction effects. The traditional SHPBs, commonly made of steel, suffer from unacceptably high noise-to-signal ratios and short loading times when used for polymeric materials. The short loading times limit the maximum achievable strains. In order to overcome these difficulties, an aluminum SHPB was used for this investigation. Aluminum lowers the bar-specimen acoustic impedance mismatch and ensures that the bar deforms linearly elastically as the polymer nanocomposite is subjected to large deformations.

Set Up of ASHPB

A schematic of the ASHPB is shown in Figure 3.5 (A) and a photograph of the actual apparatus is shown in Figure 3.5 (B). The SHPB included an incident bar (3.6 m), a transmission bar (1.2 m) and striker bars of various lengths; all with a diameter of 6.35 mm. The incident and transmission bars were mounted and aligned longitudinally in Teflon bushings that supported the two bars while permitting free axial movement only. Two electrical resistance precision strain gauges (Measurements Group, Inc.) were mounted each on the surfaces of the incident and transmission bars. Two 2310 bridge signal conditioning amplifiers (Measurement Group, Inc.) were used to amplify the strain gage signals and send them to two channels of a 5464A100 MHz digital oscilloscope (Hewlett Packard). The screen image on the oscilloscope was recorded on a pc platform through an HP-IB communication link

provided by HP BenchLink Scope software.

The test specimens, cylindrical in shape with length-to-diameter ratio close to 1 : 2, were punched using steel hole punches (McMaster-Carr Supply Company, Inc). A specimen was placed between the incident bar and transmission bar. The specimen-bar interfaces were lubricated with Teflon grease prior to loading the specimen in order to allow free radial expansion of the specimen and consequently generate homogeneous uniaxial compression conditions. The small diameter of the specimen also reduced the friction at the specimen-bar interfaces. The striker bar was accelerated to the desired impact velocity by a nitrogen air gun. A series of impact compression tests was successfully achieved at approximately constant strain rates and at a temperature of $\sim 23^\circ\text{C}$. The ASHPB alignment was checked periodically to insure testing repeatability.

Calibration of ASHPB and High-rate Data Processing

Static calibration of the ASHPB was conducted on a 2 m long horizontal, servohydraulic testing machine [90]. The incident and transmission bars were subjected to both tensile and compressive deformations and a calibration factor relating the voltage out-put from the surface strain-gages on the bars to the strain measured by the machine was identified.

The accelerated striker bar, on impact with the incident bar generates the incident pulse in the incident bar. The amplitude of the incident pulse is proportional to the striker bar velocity. When the incident pulse encounters the bar-specimen interfaces, one portion of the pulse is reflected back (reflection pulse) to the incident bar and the other portion of the pulse is transmitted (transmission pulse) to the transmission bar. While the reflected pulse is out-of-phase, the transmitted pulse is in-phase to the incident pulse. Figure 3.6 displays a typical oscilloscope output including the incident, reflected and transmitted pulses, all exhibiting high signal-to-noise ratios. The incident pulse was clear and square verifying that the impact test occurred at approximately constant strain rate. A long duration incident pulse ensured that large specimen deformations can be achieved with the current ASHPB

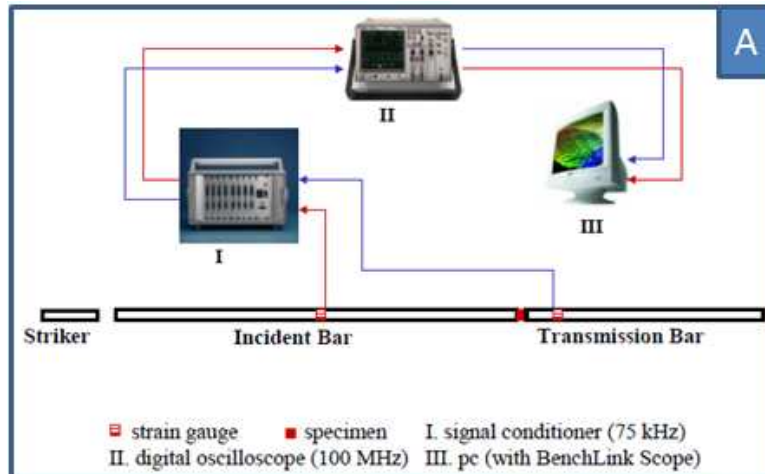


Figure 3.5: (A) A schematic of a split-Hopkinson pressure bar apparatus[11].(B) A photograph of an in-house built aluminum split-Hopkinson pressure bar apparatus.

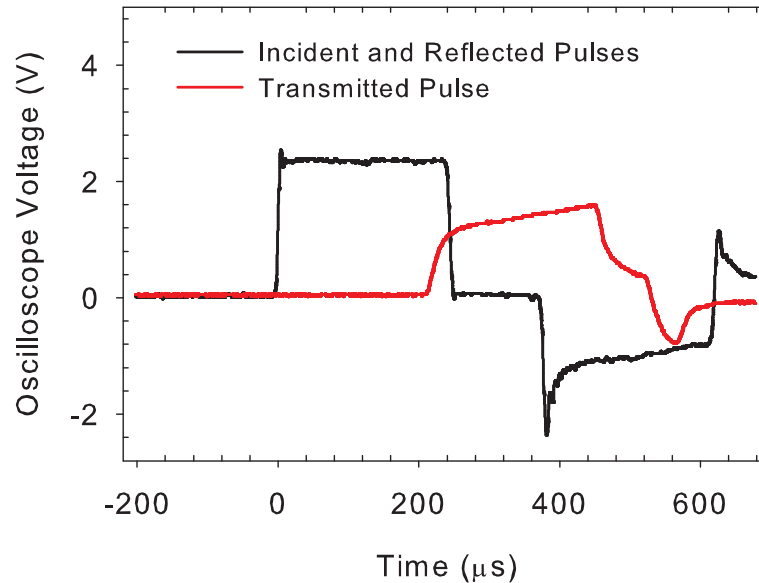


Figure 3.6: A typical oscilloscope voltage output showing the incident, reflected and transmitted pulses.

apparatus.

The degree of compatibility between the bar and specimen, and equilibrium within the specimen are crucial in impact testing via SHPB. At the onset of impact compression, the specimen surface in contact with the incident bar begins moving while the surface in contact with the transmission bar is at rest. If the equilibrium within the specimen is not established, the interaction of the pulse with the free surfaces of the bar leads to release pulses that trail the main pulse, resulting in a dispersion effect [11, 91]. To minimize the dispersion effect, the equilibration time in the specimen is ensured to be a very small fraction of the overall impact event. This is accomplished by selecting small specimen length to pulse duration ratio. Figure 3.6 demonstrates that the dispersion effect was negligible from the current ASHPB apparatus. Moreover, high signal-to-noise ratio of the pulses demonstrate that the apparatus was able to provide the large deformation stress-strain response of the polymers and polymer-clay nanocomposites at high strain-rates.

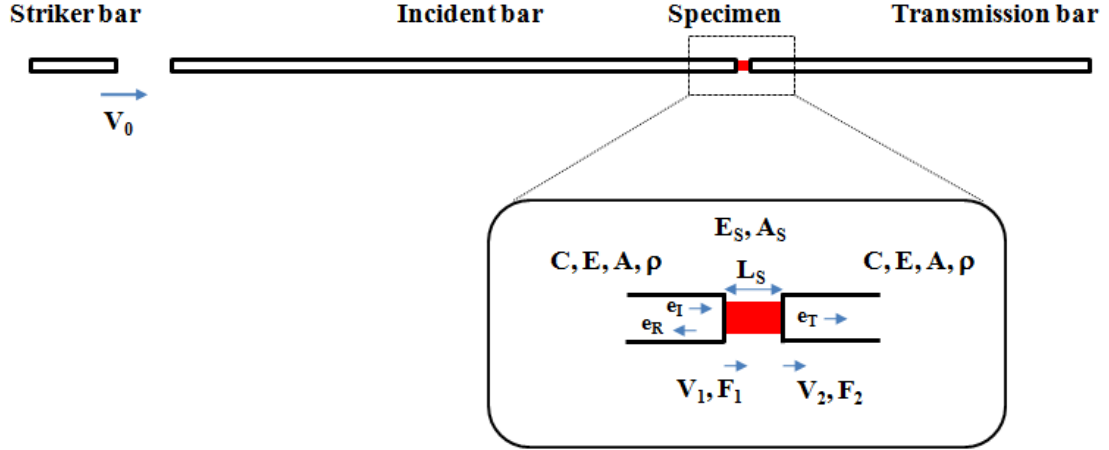


Figure 3.7: Sketch showing the variables and constants for processing the stress, strain and strain-rate from the incident, reflected and transmitted pulses. Subscripts I, R, T and S are associated with the incident bar, reflected bar (same as incident bar), transmission bar and specimen respectively.

The raw data obtained from the oscilloscope were processed using a Matlab code to obtain stress-strain responses at high impact rates. First, the data were shifted in time to account for the distances traveled by the pulses to reach the strain gages. The shifted data were then converted to stress-strain responses using the classical three-wave theory. In the three-wave theory, the average stress in the specimen is derived from the average of the sum of the three pulses. The determination of stress-strain responses from the data is detailed below.

Figure 3.7 shows all the variables and constants used in the processing of the stress, strain and strain-rate from the pulses. Based on the calibration of the ASPB, the strains $e_I(t)$, $e_R(t)$ and $e_T(t)$ associated with the incident, reflected and transmitted pulses were obtained. Nominal strain in the specimen is given as:

$$\dot{e}_S(t) = \frac{de(t)}{dt} = \frac{V_1(t) - V_2(t)}{L_S} \quad (3.2)$$

where V_1 and V_2 are the specimen face velocities, which are functions of time t and L_S is specimen length. The elastic wave speed C in the bar is given as $C = \sqrt{E/\rho}$, where E

and ρ are the elastic modulus and density of the bar. Since the incident bar experiences an elastic strain $e_I(t)$, it deforms by an elastic stress given as:

$$\sigma_I = Ee_I = C^2\rho e_I(t) \quad (3.3)$$

Moreover, e_I can also be related to the striker bar velocity, V_0 by the conservation of linear momentum as:

$$\sigma_I = \rho V_0 C \quad (3.4)$$

Equating Equations 3.3 and 3.4 gives

$$V_0 = Ce_I(t) \quad (3.5)$$

Similarly the specimen face velocities V_1 and V_2 can be related to e_I , e_R and e_T by

$$V_1(t) = C[e_I(t) - e_R(t)] \quad (3.6)$$

and

$$V_2(t) = Ce_T(t) \quad (3.7)$$

Substituting V_1 and V_2 from Equations 3.6 and 3.7 into 3.2, the nominal strain rate in the specimen can be rewritten as

$$\dot{e}_S = \frac{C}{L_S} [e_I(t) - e_R(t) - e_T(t)] \quad (3.8)$$

Integrating the above expression yields

$$e_S = \frac{C}{L_{S0}} \int_0^t [e_I(t) - e_R(t) - e_T(t)] dt \quad (3.9)$$

where L_{S0} is the initial length of the specimen. Equilibrium across the specimen gives the nominal stress in the specimen as [11],

$$\sigma_S(t) = \frac{F_1(t) + F_2(t)}{2A_{S0}} = \frac{AE}{2A_{S0}} [e_I(t) + e_R(t) + e_T(t)] \quad (3.10)$$

where A_{S0} is the initial specimen area and A is the cross-sectional area of the bar. Once the equilibrium is established in the specimen, $F_1(t) = F_2(t)$ and $e_I(t) + e_R(t) = e_T(t)$. The nominal stress and nominal strain rate in the specimen can then be reduced as

$$\sigma_S(t) = \frac{AE}{A_{S0}} e_T(t) \quad (3.11)$$

and

$$\dot{e}_S = -\frac{2C}{L_S} e_R(t) \quad (3.12)$$

respectively; and the nominal strain is given as

$$e_S = -\frac{2C}{L_{S0}} \int_0^t e_R(t) dt \quad (3.13)$$

3.5.6 Brillouin Light Scattering

Brillouin light scattering (BLS) was used to determine the in-plane (E_1) and out-of-plane (E_2) moduli of the nanocomposites. Although the Tensile tester was also used to determine E_1 , BLS was specifically used to determine E_2 which was otherwise not possible to determine by mechanical tests, owing to the micron-level thicknesses of the nanocomposite thin films. Nanocomposite thin films with a thickness 1 μm were grown on a silicon substrate and were used to perform the BLS characterization. Brillouin spectra were recorded using a Sandercock tandem 6 pass Fabry-Perot interferometer. The samples were illuminated using a solid-state laser with a wavelength, λ , of 532 nm, with a polarizer placed in the path of the beam to horizontally polarize the light. The samples were placed behind a 50 mm focus

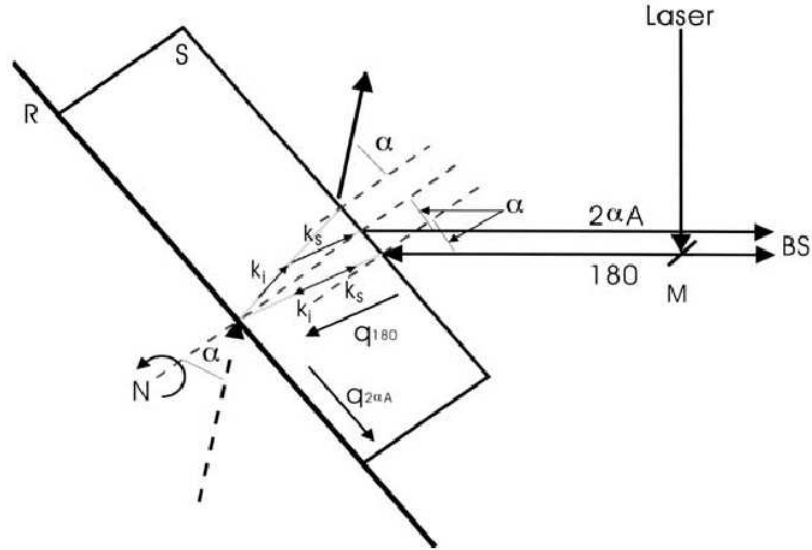


Figure 3.8: Backscattering geometry diagram for thin films S deposited on a reflecting surface (R) like Silicon wafer[92].

lens, with the polished side facing the laser. The 50 mm focusing lens was used to focus the laser light onto the sample with a focusing spot of $\sim 30 \mu\text{m}^2$; the focussing lens also acted as the collection lens. For the thin film measurements, BLS spectra were collected using a backscattering geometry, which is explained below.

The backscattering geometry used for BLS is schematically shown in Figure 3.8 [92]. When the LBL film is deposited on a reflecting substrate like the silicon wafer, the backscattering setup gives a $2\alpha A$ scattering geometry besides usual 180 scattering geometry. BLS works on the principle of inelastic scattering of light off of propagating phonons in matter [93]. In the bulk, phonons can propagate parallel and perpendicular to the direction of motion, leading to longitudinal (LA) and transverse acoustic (TA) waves. When a beam of monochromatic light (k_i) enters a medium, phonons will act as optical scattering centers. If the incident light strikes a phonon that propagates with wavevector \mathbf{q} , the scattered light leaves the medium with a change in frequency ($\Delta\omega$) and wave vector of k_s .

The frequency shift of the scattered light can be related to the longitudinal and transverse

sound velocities, v_l and v_t , inside the medium using Equations 3.14 and 3.15:

$$v_l = \frac{\Delta\omega\lambda}{2\sin(\alpha)} \quad (3.14)$$

$$v_2 = \frac{\Delta\omega\lambda}{2n} \quad (3.15)$$

where α is the scattering angle, taken to be $\alpha = 45^\circ$ for the experiments, n is the refractive index of the medium. The refractive index of the medium was determined using an Ellipsometer (refer section 3.5.7). The sound velocities were then used to determine the longitudinal (in-plane) and transverse (out-of-plane) moduli of the nanocomposites as:

$$E_1 = \rho v_l^2 \quad (3.16)$$

$$E_2 = \rho v_t^2 \quad (3.17)$$

where ρ is the density of the medium. The density of the nanocomposites, ρ_c , was determined according to the following formula:

$$\rho_c = v_f \rho_f + (1 - v_f) \rho_m \quad (3.18)$$

where v_f and ρ_f are the volume fraction and density of the MTM nanoparticles respectively and ρ_m is the density of the polymer matrix.

3.5.7 Ellipsometry

According to Equation 3.15, the refractive index of the nanocomposite films must be known to calculate the velocity of sound from the frequency shift, and ultimately yield the out-of-plane moduli. The refractive index was determined using a Nanofilm Technologie GmbH Ellipsometer. Moreover, the ellipsometer was also used to measure the film's thickness

for the first few bilayers. Thin samples deposited on Si with the polished side in the same manner as on the glass substrates and were placed in the path of the incoming laser beam. A 4-zone analysis between the angles of 45 - 90 with a step count of 2 was used for the data collection. The thickness and refractive index were determined by curve fitting the calculated Cauchy model to the experimental data.

3.5.8 Particle Size Measurement

The size of the MTM nanoparticles before and after ultra-sonication was compared using a Zetasizer Nano ZS from Malvern Instruments. The size measurements were performed using a dynamic light scattering (DLS). The DLS measures Brownian motion and relates this to the particle size in sample through a correlation function. The sample was filled to appropriate level in a standard cell provided with the instrument and was illuminated with a laser light of wavelength, λ , of 532 nm and the intensity fluctuation in the scattered light were analyzed to determine the particle size. The particle measurement in a DLS instrument is the diameter of the sphere that diffuses at the same speed as the particle being measured.

3.5.9 Differential Scanning Calorimetry

A TA instruments Q200 differential scanning calorimeter (DSC) was used to analyze the thermal transitions in the PU and the PU-MTM nanocomposites. A small amount (5-10 mg) of the sample was encapsulated in an aluminum pan placed in an insulated chamber and heated from -90°C to 300°C at a temperature rate of $10^{\circ}\text{C}/\text{min}$ and the difference in heat between the sample and an empty aluminum pan in an identical chamber per unit weight was recorded as a function of sample temperature. Data acquisition was performed using TA instruments software. The enthalpy was obtained by integration of the area under the thermal peaks.

3.5.10 Dynamic Mechanical Analysis

A TA instruments RSA3 Dynamic Mechanical Analyzer (DMA) was used to measure the storage modulus (E') and $\tan\delta$ (ratio of loss (E'') to the storage moduli) of the PU-MTM nanocomposites. Samples were tested in a uniaxial tension mode with LN2 gas cooling accessory in the temperature range $-100\text{ }^{\circ}\text{C}$ to $150\text{ }^{\circ}\text{C}$ at a temperature ramp-up rate of $3\text{ }^{\circ}\text{C}/\text{min}$. A constant strain amplitude of 0.25% at a frequency of 1 Hz was applied throughout the test with an initial static force of 0.01 N. The size of the specimens was about 15 mm long and 4 mm wide. At least 3 samples were tested in order to produce each representative curve. Data acquisition was performed using TA Orchestrator software from TA instruments.

Chapter 4

MTM Nanoparticle Volume Fraction and Layer Separation

LBL manufacturing allows the preparation of multi-layered structures with unprecedented control over the structure at the nano-scale. The organization of LBL nanocomposites has been shown to be strikingly analogous to the structure of one of the toughest natural mineral-based materials, nacre [55, 72]. In Chapter 2 we used the LBL technique to prepare the polyvinyl alcohol (PVA)-MTM nanocomposite with 50 v.% MTM clay nanoparticles that demonstrated a record high average ultimate tensile strength of 400 MPa and an average stiffness of 106 GPa at room temperature ($\sim 23^\circ\text{C}$) and humidity of $\sim 30\%$ [55]. This nanocomposite, although stiff and strong, was brittle with an average ultimate strain-to-failure of 0.003 and was only investigated at a high volume fraction of MTM nanoparticles. In this section, we utilize a positively charged polymer, polyurethane (PU), to prepare a series of PU-MTM nanocomposites and investigate the role of MTM nanoparticle volume fraction and layer separation on their finite deformation response.

4.1 Linear Layer-by-Layer Nanocomposites

The linear LBL method of nanocomposite fabrication primarily works on the principle of electrostatic attraction, although other types of interactions may also be present. Positively and negatively charged polyelectrolytes are sequentially deposited on to form a multilayered material. This is depicted by a schematic shown in Figure 4.1. In this Chapter, the

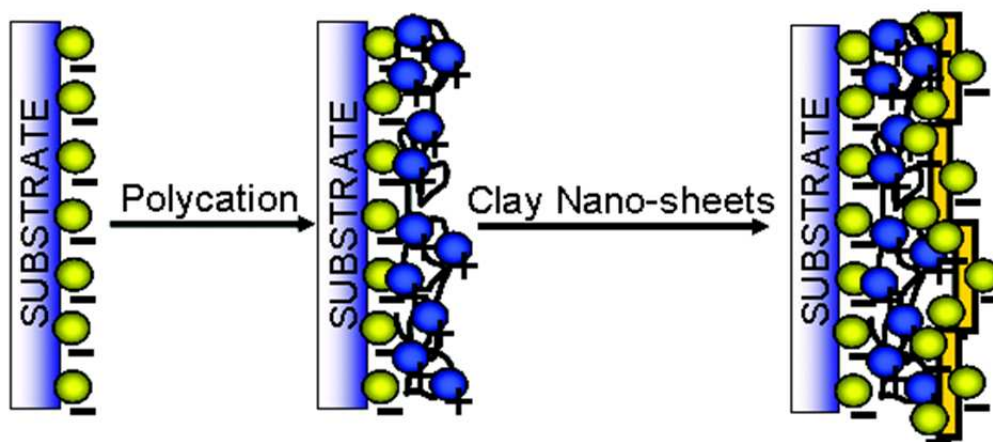


Figure 4.1: A schematic of an LBL deposition showing the electrostatic charges.

characteristic of LBL to provide an unprecedented control over the structure at nanoscale is utilized to fabricate a series of 300-bilayer PU-MTM nanocomposites with a wide range of volume fractions (ranging from 5 v.% to 20 v.%) of MTM nanoparticles.

The systematic variation in MTM nanoparticle volume fraction was employed by varying the concentration of PU in solution to vary the thickness of the PU layer deposited in LBL manufacturing (Figure 4.2). The volume fraction of MTM nanoparticles was inversely related to the thickness of the PU layer in the nanocomposite. The nanocomposite with a smaller PU layer thickness had a higher volume fraction of MTM nanoparticles than the one having a larger PU layer thickness (Figure 4.2). The entire series of nanocomposites, however, had a constant MTM dispersion in each nanolayer and constant clay nanolayer thickness. This structural variation facilitated the study of the effect of MTM nanoparticle separation on the mechanics of the PU-MTM nanocomposites.

For a successful LBL deposition, the MTM nanoparticles must create a densely packed layer on the surface of the underlying polymer, which is analogous to Langmuir adsorption [94]. Decreasing the concentration of the MTM dispersion beyond 0.5 wt.% while keeping the immersion time constant would lead to incomplete surface coverage with the MTM nanoparticles and while this may result in an initial build up of a few layers, it would even-

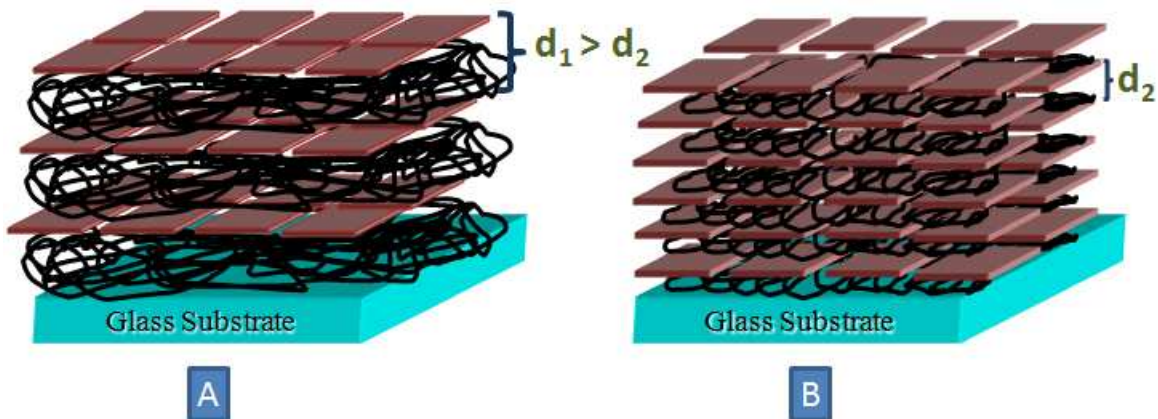


Figure 4.2: Ideal schematic of nanocomposite structure with (A) lower volume fraction and (B) higher volume fraction of MTM nanoparticles[86].

tually lead to termination of the growth process. Increasing the concentration of the MTM dispersion may not affect its loading because after saturation of the adsorbent (MTM) on the surface, mutual repulsion of negatively charged MTM nanoparticles would prevent absorption of further stacks. Additionally, any loosely bound excess MTM nanoparticles are removed from the surface during the rinsing step. Hence, variation in MTM nanoparticle concentration in solution was not a feasible method for changing the volume fraction of MTM nanoparticles.

4.2 Structural Characterization

The TGA thermogram of pure PU revealed poor thermal insulation with almost complete decomposition at $\sim 500^\circ\text{C}$ (Figure 4.3). Pure MTM clay, on the other hand, didn't fully decompose even at a temperature as high as 850°C and showed a ~ 5 percent decrease in weight. This information was used to determine the volume fraction of MTM nanoparticles in the PU-MTM nanocomposites. A series of PU-MTM nanocomposites with MTM volume fractions ranging from 5 v.% to 20 v.% was manufactured as listed in Table 4.1. The decomposition onset temperature of the nanocomposites increased with increased volume fractions of MTM nanoparticles as can be seen in Figure 4.3. This enhancement of ther-

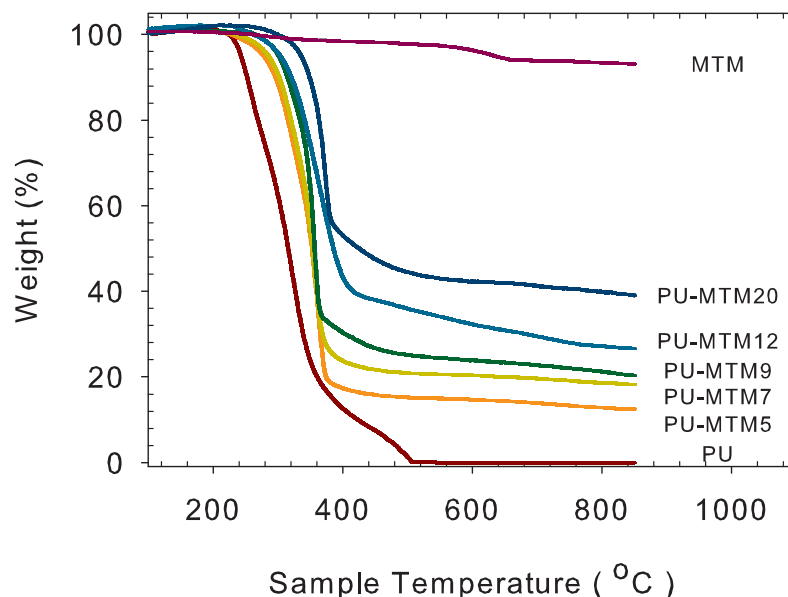


Figure 4.3: Thermogravimetric analysis for PU, a series of PU-MTM nanocomposites and MTM clay[86].

mal stability provided evidence of thermo-mechanical interactions between PU and MTM nanoparticles.

SEM images of the cross-sections of 300-bilayer PU-MTM nanocomposites revealed uniform thicknesses (Figure 4.4). The nanocomposites thicknesses decreased with an increase in loading of MTM nanoparticles and was consistent with an increased thickness of the deposited PU layer (Figure 4.5 and Table 4.2). In Figure 2.12, it was shown via Ellipsometry studies that LBL manufactured PVA-MTM nanocomposite demonstrated a linear growth for the first few bilayers. Figure 4.6 shows the film thickness measured using the SEM for the PU-MTM7 nanocomposite as a function of the number of bilayers and verified the linear growth for subsequent layers and much larger thicknesses.

For traditional LBL manufacturing, the polymer should be water-soluble and preferably charged. The present PU satisfied these requirements (Figure 4.7). The presence of a tertiary ammonium group in the short side chain and high density of hydrophilic groups

Sample Name	MTM loading (wt.%)	MTM loading (v.%)
PU-MTM5	13	5
PU-MTM7	18	7
PU-MTM9	21	9
PU-MTM12	27	12
PU-MTM20	41	20

Table 4.1: PU-MTM nanocomposite nomenclature[86].

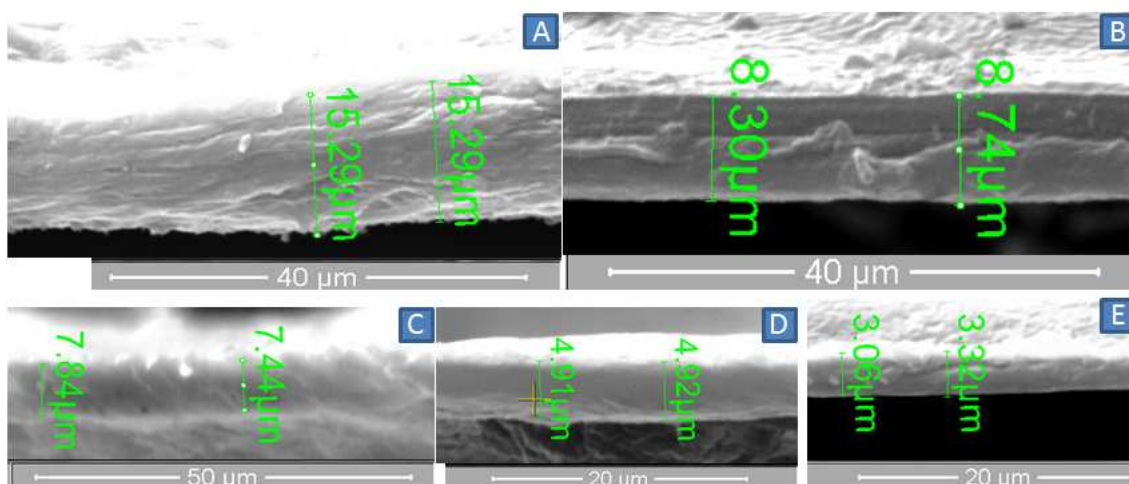


Figure 4.4: Typical SEM images showing cross-sections of (a) 5 v.%, (b) 7 v.%, (c) 9 v.%, (d) 12 v.% and (e) 20 v.% 300-bilayer PU-MTM nanocomposite[86].

Sample Name	Film Thickness (μm)	Average Bilayer Thickness, t_b (nm)
PU-MTM5	16.1 \pm 1.2	53
PU-MTM7	8.7 \pm 0.7	31
PU-MTM9	6.8 \pm 0.7	24
PU-MTM12	5.1 \pm 0.3	17
PU-MTM20	3.2 \pm 0.1	11

Table 4.2: Thickness of 300-bilayer PU-MTM nanocomposites and average bilayer thickness as a function of average volume fraction of MTM nanoparticles[86].

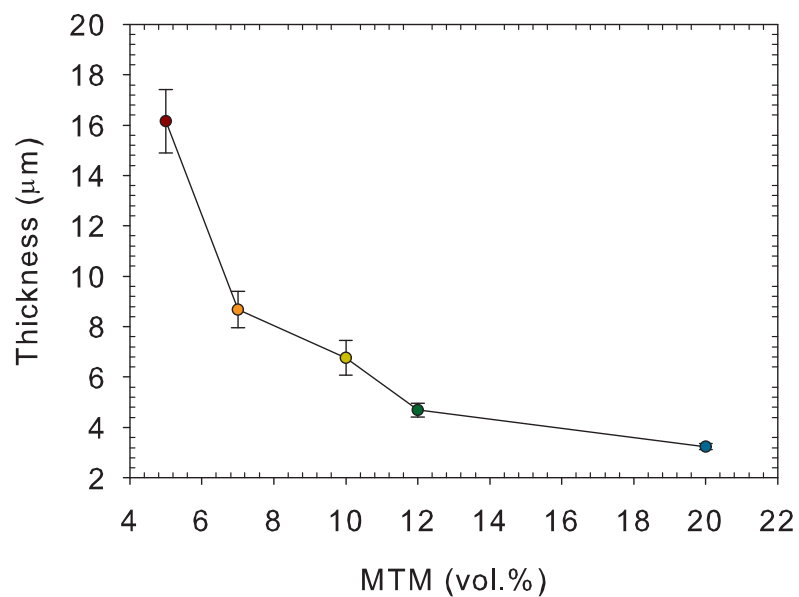


Figure 4.5: Thickness of 300-bilayer PU-MTM nanocomposites as a function of volume fractions of MTM nanoparticles. Error bars indicate the uncertainty in thicknesses and volume fractions.

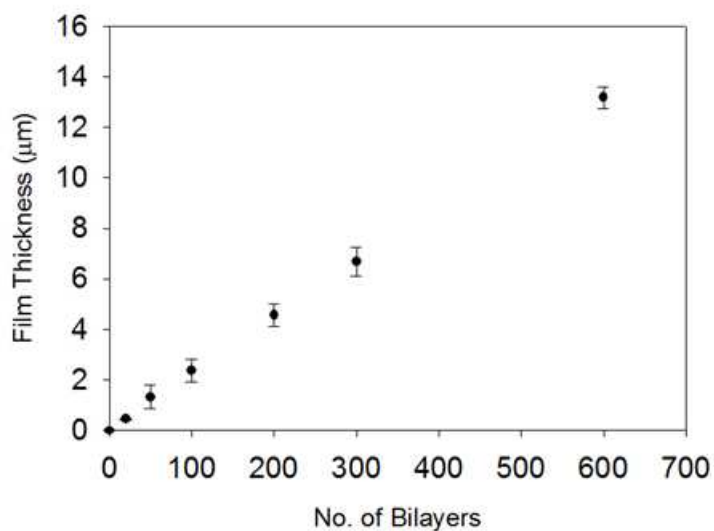


Figure 4.6: Linear growth in film thickness of PU-MTM5 nanocomposite as a function of bilayers. Error bars indicate the uncertainty in thicknesses[86].

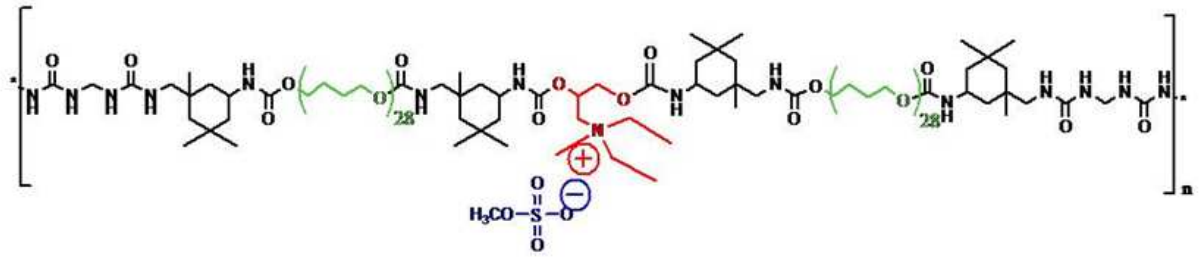


Figure 4.7: Chemical Structure of cationic PU copolymer. The cationic functional group of the polymer is highlighted in red, the counter-ion in blue, the soft segment in green and the hard segment in black[86].

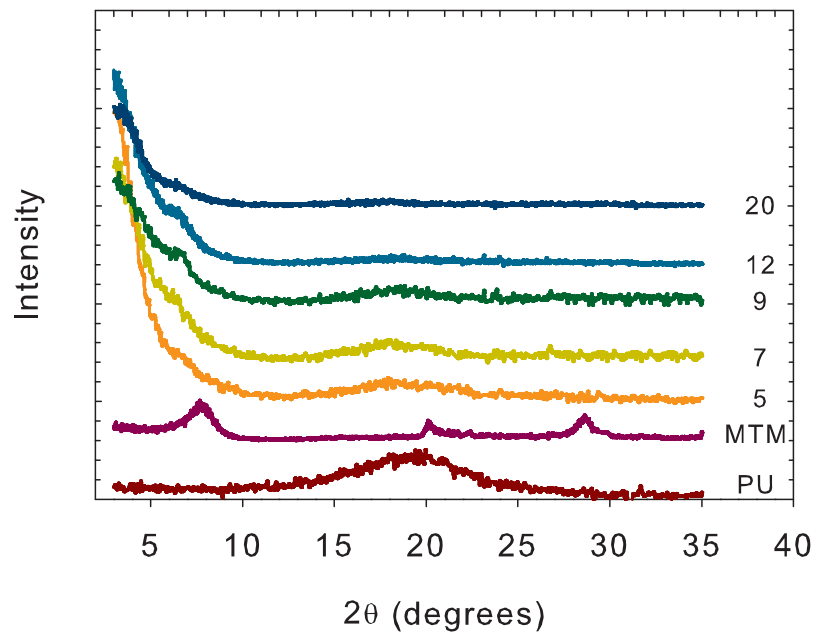


Figure 4.8: Wide angle X-ray diffraction patterns of PU, MTM clay and PU-MTM nanocomposites. Numbers indicate average volume fractions of MTM nanoparticles[86].

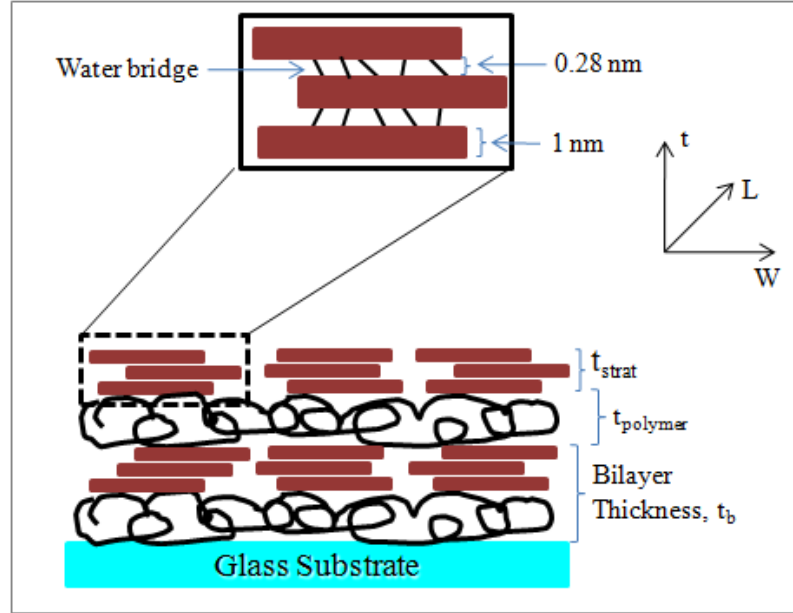


Figure 4.9: Schematic nanostructure of the PU-MTM Nanocomposite[86].

along the backbone impart high solubility in water. The present PU is a block copolymer with alternating soft and hard segments. While the hard segments provided stiffness and strength, large soft segments imparted high ductility to PU. These large proportions of soft segments formed an amorphous domain as examined using wide angle x-ray diffraction (WAXD) (Figure 4.8). An amorphous peak spanning over a 2θ angle of approximately 10° (from 15° to 25°) was observed in the case of pure PU. The WAXD pattern for the MTM clay showed three distinct peaks in the scan range shown. The lowest angle diffraction peak at a 2θ angle of 7.66° corresponded to a basal (001) spacing of 11.5 \AA , suggesting a gallery spacing (i.e. the distance between the silicate layers) of 1.5 \AA . The (004) reflection peak was weakly present at a 2θ angle of 19.96° with a calculated basal spacing of 4.45 \AA [95, 96]. Other higher-order reflections were very weak reflecting the disorder present in the MTM clay powder [95, 96]. In addition to the (001) and (004) reflection peaks, there was a two-dimensional band (02,11) at a 2θ angle of 28.6° , signifying a disordered stacking of the silicate layers [95, 96]. The entire series of PU-MTM nanocomposites

(Figure 4.8) exhibited a small shoulder at a 2θ angle of 6.86° corresponding to a basal (001) spacing of 12.8 \AA . This confirmed a constant MTM dispersion within each bilayer in the PU-MTM nanocomposites irrespective of the volume fraction of MTM nanoparticles, as discussed earlier. The disappearance of higher angle (004) and two-dimensional (02,11) diffraction peaks confirmed complete exfoliation of silicate in the PU matrix [95, 96]. The presence of small-angle shoulder in the PU-MTM nanocomposites indicates that for each MTM nanoparticle deposition step MTM nanoparticles were deposited in multiple layers, suggesting that the multi-layered structure of PU-MTM nanocomposites consisted of stratified layers of silicate nanoparticles (each of 1 nm thickness) forming each clay nanolayer (4.9). The basal spacing of 12.8 \AA , or 1.28 nm was accounted for by the likely presence of water bridges of 0.28 nm between the silicate layers which is reasonably close to the reported values of 1.26 nm for hydrated montmorillonite [97]. The lower bound on the number of silicate layers in each stratified layer may be determined from the minimum average bilayer thickness (c.f. Table 4.2 and Figure 4.9) and volume fraction of MTM nanoparticles associated with it as follows:

$$t_{strat} + t_{pu} = \min(t_b) \quad (4.1)$$

$$L_{strat} = L_{pu} \quad (4.2)$$

$$W_{strat} = W_{pu} \quad (4.3)$$

where t_{strat} is the thickness of the stratified layer (c.f. 4.9), t_{pu} is the thickness of the PU layer, t_b is the average bilayer thicknesses and $\min(t_b)$ is the smallest value of t_b in Table 4.2. L_{strat} and L_{pu} are the lengths of the stratified layer and PU layer respectively; and W_{strat} and W_{pu} are the widths of the stratified layer and PU layer respectively. Here, in order to simplify our calculations, we make an assumption that the stratified layer is

occupied entirely by MTM nanoparticles.

Using Equations (2), (3) and (4),

$$\frac{t_{strat}}{\min(t_b)} = v_f \quad (4.4)$$

where v_f is the volume fraction of MTM nanoparticles associated with $\min(t_b)$. t_{strat} is determined as (c.f. 4.9):

$$t_{strat} = 1(n_s) + 0.28(n_s - 1) \quad (4.5)$$

where n_s is the number of silicate layers in each stratified layer. Substituting the value of t_{strat} from Equation (5) in (6), a lower bound on n_s is

$$n_s = 2.55 \quad (4.6)$$

The upper bound on the number of silicate layers has been determined to be 3 based on a representative volume element description of the nanocomposite structure that differs slightly from that shown in Figure 4.9 [98]. It is worth emphasizing here that the deposition of the stratified layers of nanoparticles was the same for all nanocomposites. Therefore, the study of the effect of volume fraction of MTM nanoparticles reduced to a study of the effect of the polymer layer thickness or MTM nanoparticle spacing on the finite deformation response of PU-MTM nanocomposites.

4.3 Mechanical Characterization

PU-MTM nanocomposites demonstrated an increase in stiffness, yield strength and ultimate tensile strength when compared with pure PU (Figures 4.10 and 4.11, Tables 4.3 and 4.4). With only 5 v.% of MTM nanoparticles, there was a 10.5-fold increase in the yield strength and an 18-fold increase in the stiffness of the PU-MTM nanocomposite com-

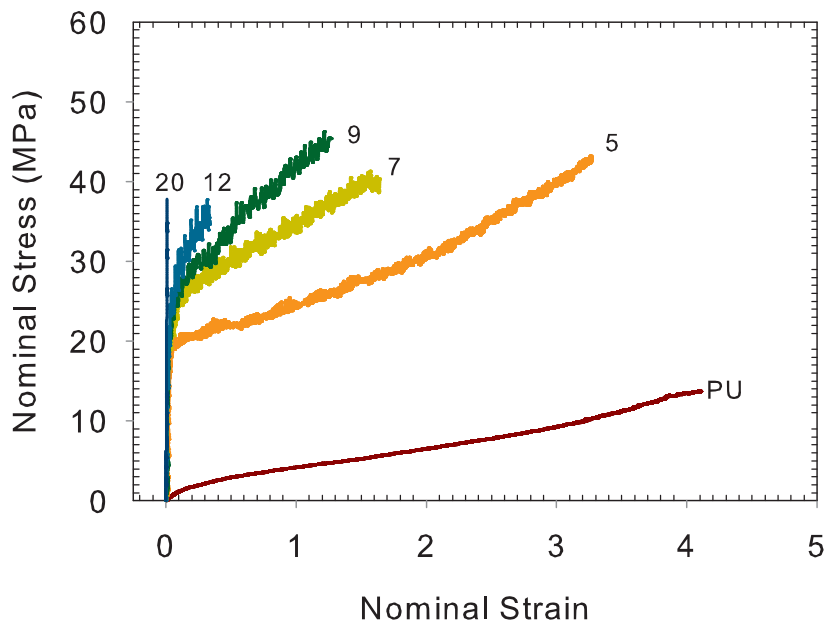


Figure 4.10: Representative nominal stress-strain constitutive response curves of PU and PU-MTM nanocomposites. The dog-bone specimens were loaded at a constant strain rate of 0.005/s at room temperature ($\sim 23^\circ\text{C}$) and a humidity of $\sim 30\%$ until failure. Numbers shown indicate average volume fractions of MTM nanoparticles[86].

pared to pure PU. The ultimate (nominal) tensile strength increased by a factor of 3.1. The stiffness and yield strength continued to increase with an increase in the volume fraction of MTM nanoparticles (Figures 4.15 and 4.16). With 9 v.% MTM nanoparticles, the yield strength and stiffness increased 14 and 40 times respectively over pure PU. This enhancement in mechanical properties, viz., stiffness, yield strength and ultimate strength is attributed to strong PU and MTM nanoparticle interaction and MTM nanoparticles alignment parallel to the direction of applied load that allowed a substantial fraction of the load to be transferred to the stiffer, stronger MTM nanoparticles. The ultimate strain-to-failure, however, decreased with increased volume fraction of MTM nanoparticles.

PU-MTM nanocomposites with less than 12 v.% MTM nanoparticles failed in tension with a pronounced yielding of the polymer phase. At 12 v.%, some of the specimens frac-

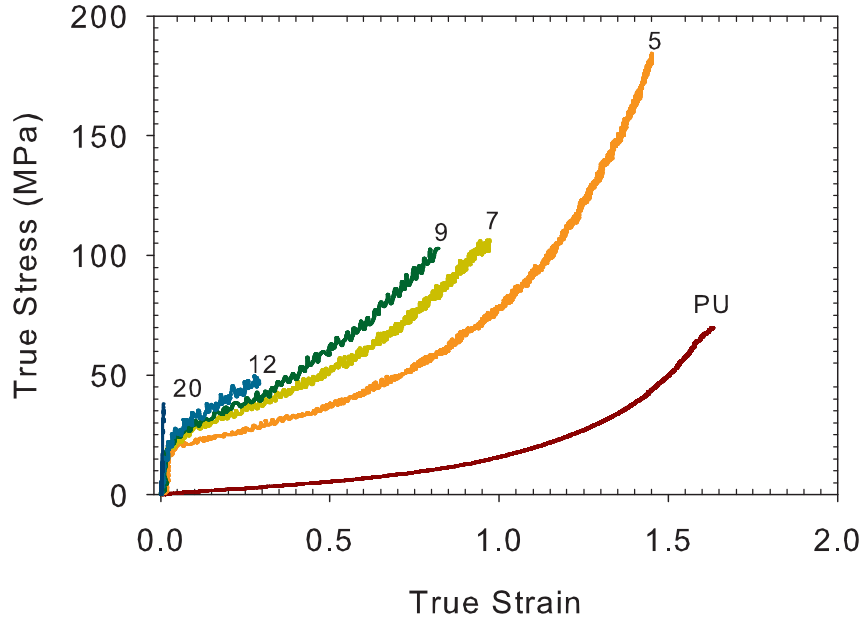


Figure 4.11: Representative true stress-strain constitutive response curves of PU and PU-MTM nanocomposites. The dog-bone specimens were loaded at a constant strain rate of 0.005/s at room temperature ($\sim 23^\circ\text{C}$) and a humidity of $\sim 30\%$ until failure. Numbers shown indicate average volume fractions of MTM nanoparticles[86].

Sample Name	Modulus (GPa)	Yield Strength (MPa)	Modulus Ratio (E_{nc}/E_{pu})
PU	0.025 ± 0.005	2.0 ± 0.1	1
PU-MTM5	0.45 ± 0.05	21.1 ± 0.3	18
PU-MTM7	0.74 ± 0.10	25.2 ± 0.4	30
PU-MTM9	1.0 ± 0.2	27.3 ± 0.4	40
PU-MTM12	1.65 ± 0.15	28.5 ± 0.7	66
PU-MTM20	3.6 ± 0.2	— — —	144

Table 4.3: Summary of the mechanical properties of pure PU and PU-MTM nanocomposites at a constant strain rate of 0.005/s at room temperature ($\sim 23^\circ\text{C}$) and a humidity of $\sim 30\%$ [86].

Sample Name	Ultimate Tensile Strength (MPa)	Ultimate Strain
PU	13.2 \pm 0.9	4.10 \pm 0.10
PU-MTM5	41.2 \pm 3.8	3.16 \pm 0.10
PU-MTM7	39.5 \pm 3.0	1.56 \pm 0.08
PU-MTM9	41.0 \pm 2.7	1.11 \pm 0.09
PU-MTM12	37.4 \pm 2.9	0.15 \pm 0.14
PU-MTM20	34.2 \pm 9.3	0.008 \pm 0.003

Table 4.4: Summary of the mechanical properties of pure PU and PU-MTM nanocomposites at a constant strain rate of 0.005/s at room temperature ($\sim 23^\circ\text{C}$) and a humidity of $\sim 30\%$ [86].

tured with no yielding while a few specimens failed after yielding (c.f. Figure 4.12). This is also evident from a large standard deviation on the strain-to-failure value for only this nanocomposite in Table 4.3. The large variation in strain-to-failure indicates a transition at this volume fraction from ductile to brittle behavior. Further increase in the volume fraction of MTM nanoparticles resulted in brittle nanocomposites. The 20 v.% MTM nanocomposite had a strain-to-failure of 0.008 and a stiffness increase of more than two orders of magnitude over pure PU. Thus, these nanocomposites demonstrated an increasing stiffness (and yield strength) with nanoparticle volume fraction, in contrast to previously published (Figure 4.13) [41, 42, 45, 46, 56–58, 99]. The strain energy at failure (area under the true stress-strain curves) increased 3.25-fold with an incorporation of 5 v.% of MTM nanoparticles when compared with PU (Figure 4.14). Further increase in the volume fraction of MTM nanoparticles decreased the toughness due to the decrease in the ultimate strain-to-failure. The strain energy at moderate strains, however, increased with increasing MTM volume fraction until the volume fraction reached the transition point from ductile to brittle. The energy at 0.5 strain, $U_{0.5}$, increased ~ 10 times with 12 v.% MTM nanoparticles when compared with pure PU (Figure 4.14).

We believe that simultaneous improvement in stiffness, strength and toughness in these PU-MTM nanocomposites is the result of both a strong interaction between the MTM

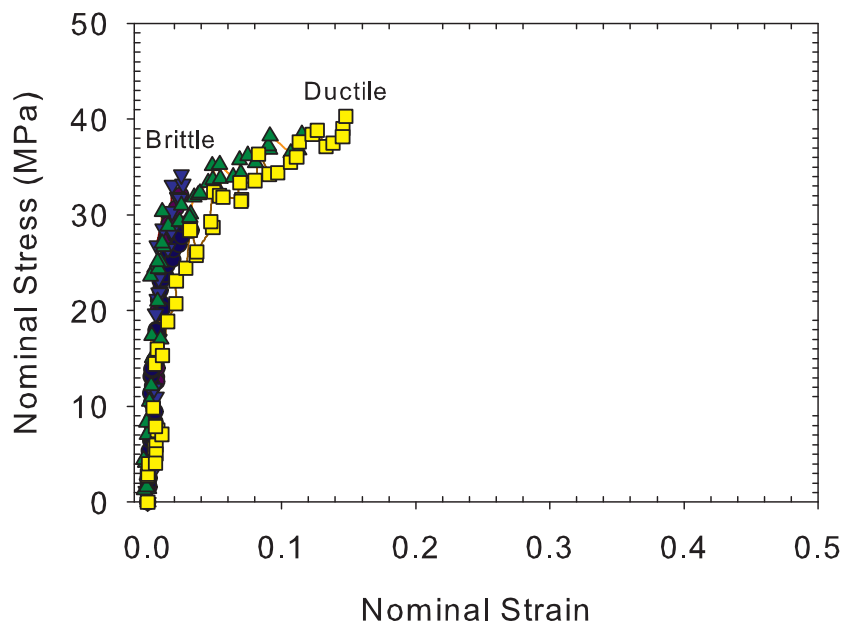


Figure 4.12: Representative nominal stress-strain constitutive responses for 12 v.% PU-MTM nanocomposite specimens. The dog-bone specimens were loaded at a constant strain rate of 0.005/s at room temperature ($\sim 23^\circ\text{C}$) and a humidity of $\sim 30\%$ until failure[86].

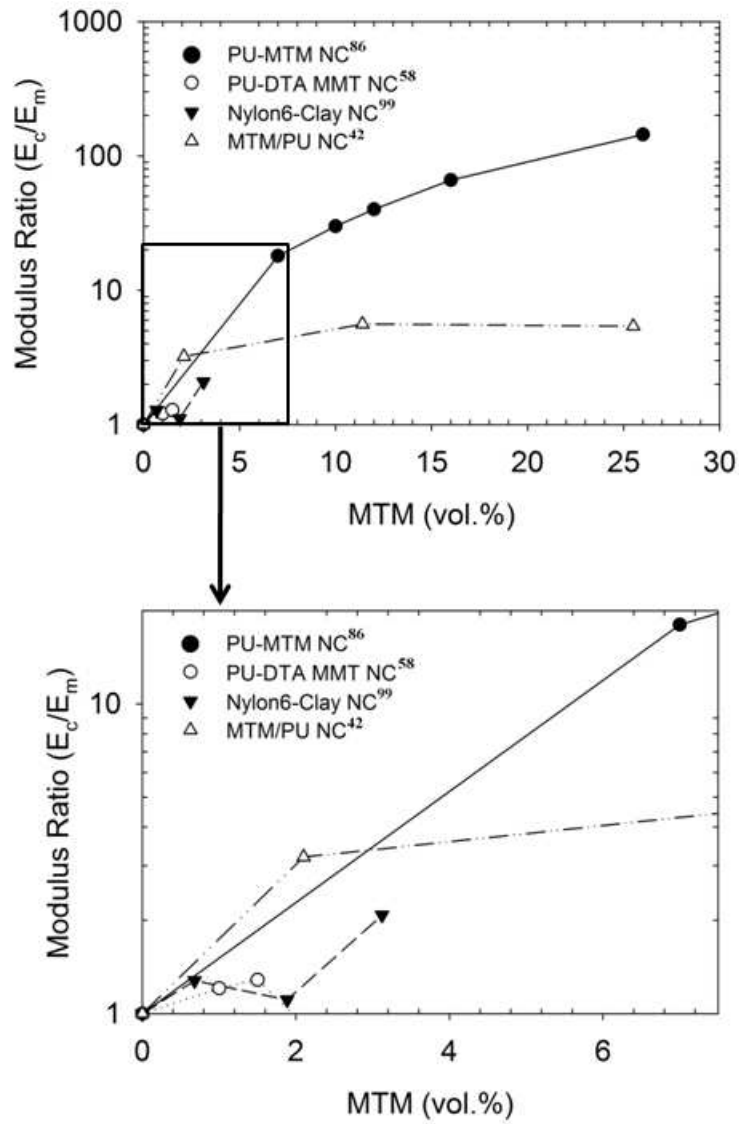


Figure 4.13: Comparison of enhancement in modulus of PU-MTM nanocomposites with other clay nanocomposites[86].

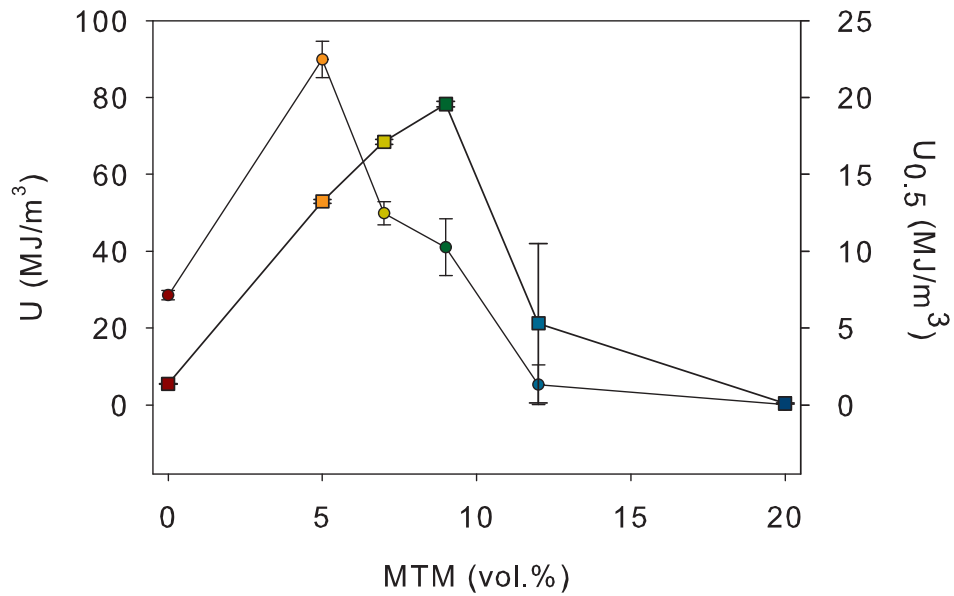


Figure 4.14: Strain energy at failure (shown as circular data points) and at 0.5 strain (shown as square data points) for PU and PU-MTM nanocomposites as a function of average volume fraction of MTM nanoparticles[86].

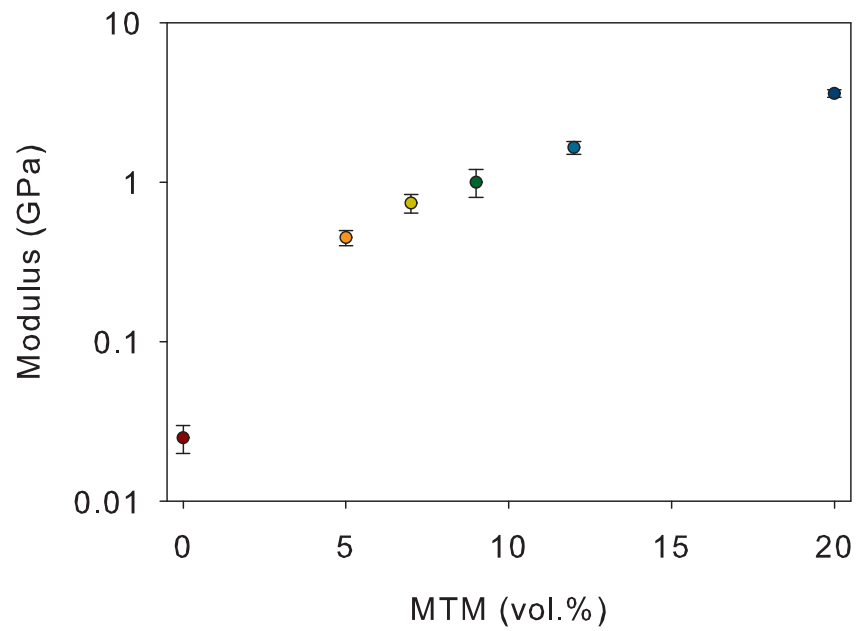


Figure 4.15: Modulus of PU and PU-MTM nanocomposites as a function of average volume fraction of MTM nanoparticles.

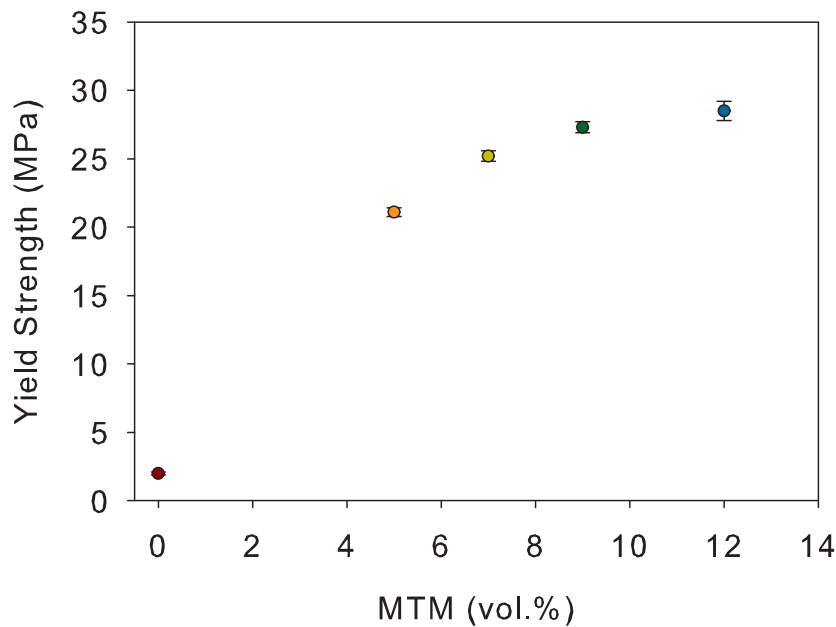


Figure 4.16: Yield strength of PU and PU-MTM nanocomposites as a function of average volume fraction of MTM nanoparticles.

nanoparticles and the PU and the control of defects such as regions of particle agglomeration and particle occlusions. The presence of MTM nanoparticles in alternate nanolayers modified the bulk PU in close proximity to the nanoparticles to that of a material composed of confined and stiffened PU chains with restricted mobility [40, 45, 100, 101]. The PU particle size measured by dynamic light scattering suggested that PU chains attained a similar conformation at all MTM loadings [102]. Since the thickness of the PU layer decreased with an increase in MTM loading, the volume of confined PU chains increased with increased volume fractions of MTM nanoparticles or decreased PU layer thicknesses. An increase in the MTM loading or decrease in the polymer layer thickness gradually resulted in a transition of bulk PU into confined PU chains, thus resulting in brittle nanocomposites with enhanced stiffness and reduced ultimate strain-to-failure. This transition occurred at 12 v.% MTM nanoparticles corresponding to a polymer layer thickness or MTM nanoparticle separation of ~ 13 nm (assuming 3 silicate sheets in each clay nano-layer). Below this

thickness, brittle behavior dominated the nanocomposite response. At low levels of MTM nanoparticle loadings, the bulk polymer regions were sufficiently mobile and flexible to plastically deform and provide ductility to the nanocomposite response.

The formation of confined polymer chains and their reduced mobility in close proximity to nanoparticles has been addressed previously [45, 100, 101, 103, 104]. For example, Efremov et al. observed the emergence of a pronounced glass transition for polystyrene, poly(2-vinyl pyridine) and poly(methyl methacrylate) up to thicknesses of 3 nm in close proximity to a platinum surface [104]. However, the present investigation allowed the polymer layer thickness to be the only adjustable parameter in a series of PU-MTM nanocomposites. This study of the effect of polymer layer thickness on the finite deformation response can further explain the premature failure of nanocomposites containing non-uniform dispersions of nanoparticles as being the result of defects leading to crack formation within regions of poor particle separation, initiating early failure [56–58, 105, 106].

4.4 Thermal Characterization

The effect of polymer layer thickness on the thermal properties of PU-MTM nanocomposites was determined by conducting differential scanning calorimetry (DSC) measurements on pure PU and the PU-MTM nanocomposites (Figure 4.17). PU exhibited an endotherm at approximately 90 °C indicating a transition to increased thermal motion of PU chains. This thermal transition was suppressed in the case of PU-MTM nanocomposites (Figures 4.17 and 4.18). Figure 4.18 shows the area under the endotherm peak (normalized with PU weight) as a function of the MTM nanoparticle volume fraction. The area under the peak was found to decrease with an increase in the loading of MTM nanoparticles or decreased polymer layer thickness.

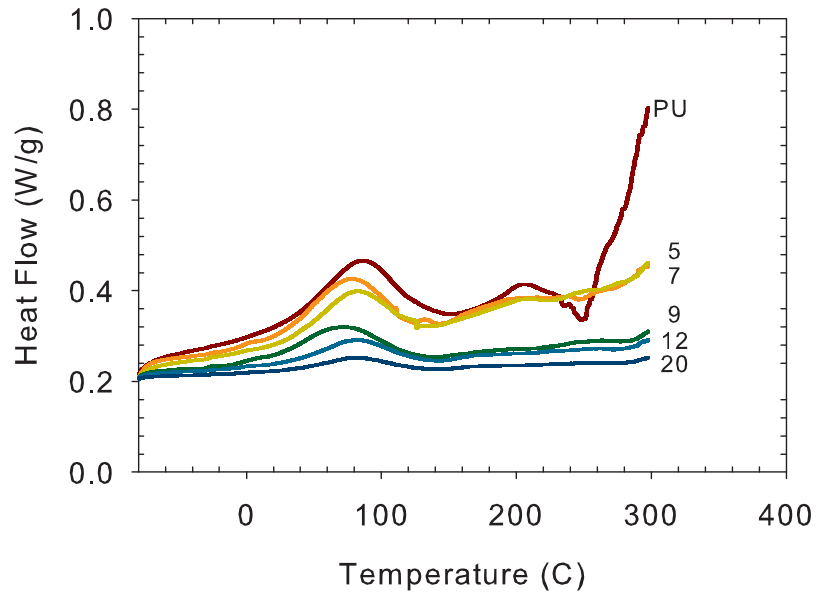


Figure 4.17: DSC traces of pure PU and PU-MTM nanocomposites. Numbers indicate average volume fractions of MTM nanoparticles[86].

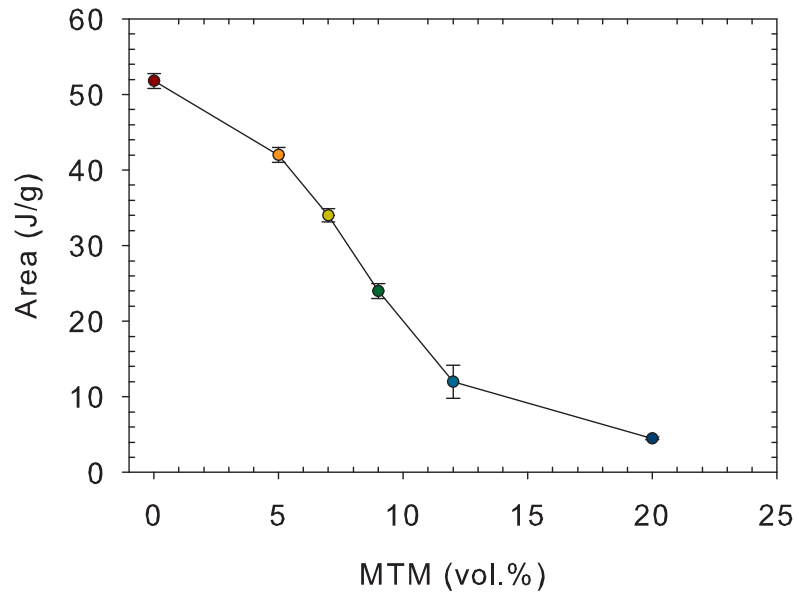


Figure 4.18: Area under the transition peak for Pure PU and PU-MTM nanocomposites normalized by the amount of PU present[86].

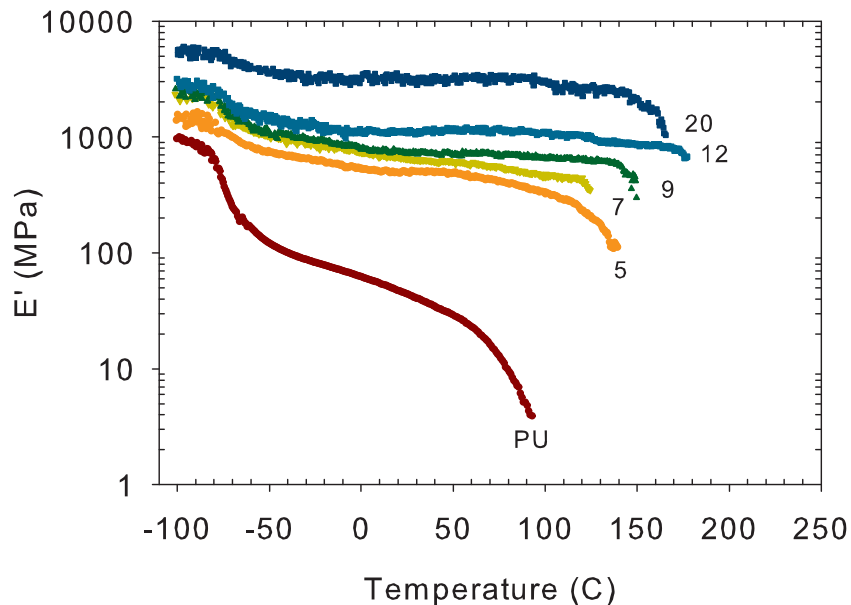


Figure 4.19: Storage modulus as a function of sample temperature for pure PU and PU-MTM nanocomposites. Numbers indicate average volume fractions of MTM nanoparticles[86].

4.5 Thermo-Mechanical Characterization

The reinforcing effect of MTM nanoparticles was prominent at the entire observed range of temperatures (Figure 4.19). The storage modulus was enhanced at all temperatures and showed an increased thermal stability with an increase in the volume fraction of MTM nanoparticles. The $\tan\delta$ for the pure PU curve showed a peak at about -76°C , which is attributed to its glass transition temperature (Figure 4.18). For the PU-MTM nanocomposites, $\tan\delta$ was shifted to a slightly higher temperature. This shift of the peak was due to the hindered cooperative motion of the PU chains. The peak value of $\tan\delta$ was also found to decrease with an increased volume fraction of MTM nanoparticles. This was due to the interfacial interactions between the PU and MTM nanoparticles also observed in the TGA and DSC results.

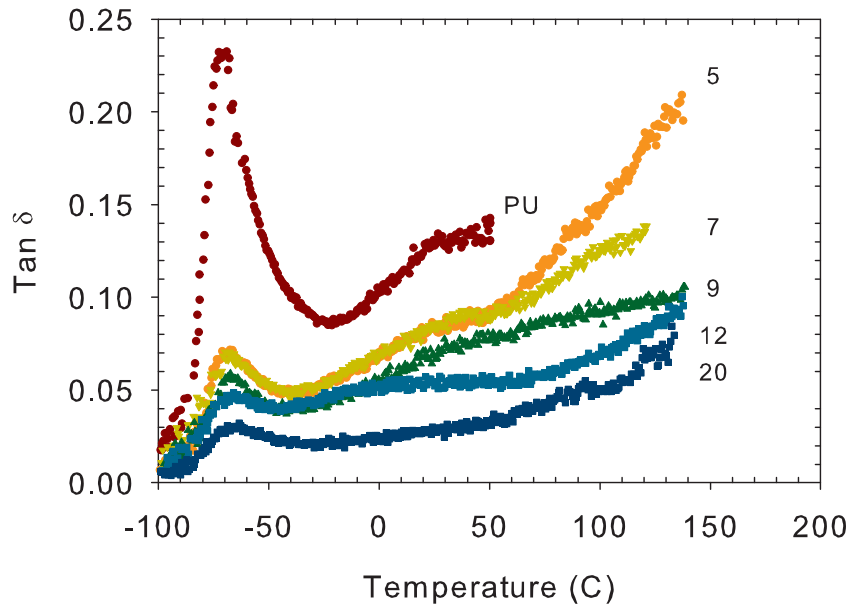


Figure 4.20: $\tan\delta$ as a function of sample temperature for pure PU and PU-MTM nanocomposites. Numbers indicate average volume fractions of MTM nanoparticles[86].

4.6 Summary and Conclusions

In summary, the role of MTM nanoparticle separation in controlling the finite deformation constitutive response of polymer-clay nanocomposites has been demonstrated. A series of PU-MTM nanocomposites, with alternating PU and MTM nano-layers, was prepared using the LBL manufacturing technique. LBL allowed us to vary the MTM nanoparticle volume fraction by systematically varying the MTM nanoparticle separation while retaining the structural organization at all volume fractions. The PU-MTM nanocomposites demonstrated enhanced mechanical properties at all volume fractions of MTM nanoparticles, e.g. the yield strength and stiffness increased 14 and 40 times respectively over pure PU with 9 v.% of MTM nanoparticles. The PU-MTM nanocomposite with 20 v.% MTM nanoparticles demonstrated a stiffness increase of more than two orders of magnitude.

A transition from ductile to brittle behavior in deformation response was observed at 12

v.% of MTM nanoparticles. We demonstrated the existence of a critical MTM nanoparticle separation below which brittle behavior dominated the nanocomposite response. Further reduction in MTM nanoparticle separation led to an increased restricted motion of PU chains, resulting in brittle fracture of PU-MTM nanocomposites.

The current investigation addresses the issues facing the design of polymer-clay nanocomposites. The constant dispersion of MTM nanoparticles over a wide range of volume fractions and the role of the polymer layer thickness in controlling the finite deformation response of nanocomposites enabled design optimization in terms of tailoring stiffness, strength and toughness of these nanocomposites. We have also illustrated the current limit of the LBL technology to manufacture PU-MTM nanocomposites with simultaneously improved stiffness, strength and toughness. The next Chapter will focus on investigating the role of the stratified layer of MTM nanoparticles on controlling the finite deformation response of PU-MTM nanocomposites. A constitutive model for the finite deformation response of these nanocomposites will also be developed in Chapter 6.

Chapter 5

MTM Nanoparticle Layer Stratification

The previous chapter dealt with investigating the role of the MTM nanoparticle layer separation in controlling the finite deformation response of multi-layered PU-MTM nanocomposites. It was also demonstrated that the MTM layer in these nanocomposites, although consistently dispersed irrespective of the MTM volume fraction, consisted of stratified layer of MTM nanoparticles. In this section, the dispersion of MTM nanoparticles in each layer has been improved by reducing the number of MTM nanoparticles in each layer. The stratified layer of silicate sheets is removed by ultra-sonication of the MTM dispersion prior to the preparation of multi-layered nanocomposites. A series of nanocomposites with alternate layers of PU and sonicated MTM (labeled herein after as SMTM) was prepared with a wide range of MTM volume fractions. For consistent comparison with the series of PU-MTM nanocomposites, the same PU layer thicknesses were deposited in the preparation of PU-SMTM nanocomposites.

5.1 Structural Characterization

A solution of MTM nanoparticles was ultra sonicated for several hours and the particle size as a function of sonication time was determined using the zetasizer (c.f. Figure 5.1). The average particle size decreased from ~ 300 nm to ~ 150 nm in approximately 5 hrs of sonication, and remained constant for several days after sonication. The reduction of particle size is attributed to the possible delamination of the stacked silicate sheets that were present before the ultrasonication. It is important to note here that the understanding

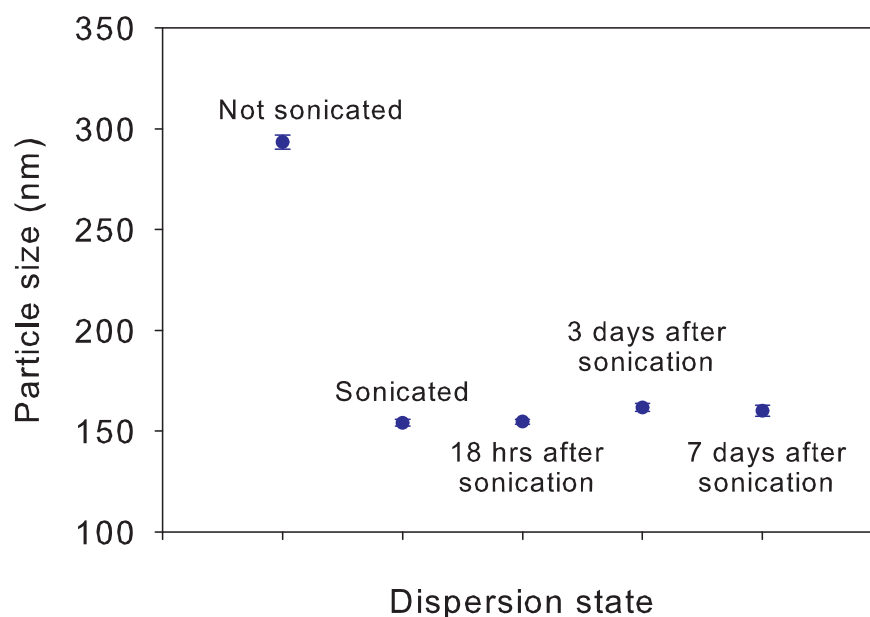


Figure 5.1: Particle size in a sonicated MTM nanoparticle solution as a function of time after sonication.

of the particle size in an absolute sense, especially for the case of disc-shaped particles, is questionable. This is owing to the fact that the particle measurement in a DLS instrument is the diameter of the sphere that diffuses at the same speed as the particle being measured. The particle size remained unchanged after 7 days (and even several weeks) after sonication suggesting the permanent delamination of MTM nanoparticles and avoiding the possibility of re-assembly of MTM nanoparticles during nanocomposite fabrication.

Using the sonicated clay solution, a series of PU-SMTM nanocomposites was prepared with the same series of PU layer thicknesses as before. Table 5.1 shows the SMTM volume fractions fabricated in the series of PU-SMTM nanocomposites. The PU-SMTM nanocomposites show a reduction in the MTM volume fraction for the same PU layer thickness in comparison with the PU-MTM nanocomposites. This confirmed that the number of nanoparticles in the stratified layer is decreased in PU-SMTM nanocomposites. This was also validated by comparing the overall thicknesses of the 300 bi-layer films of the PU-MTM and PU-SMTM nanocomposites. The thicknesses of PU-MTM and PU-SMTM

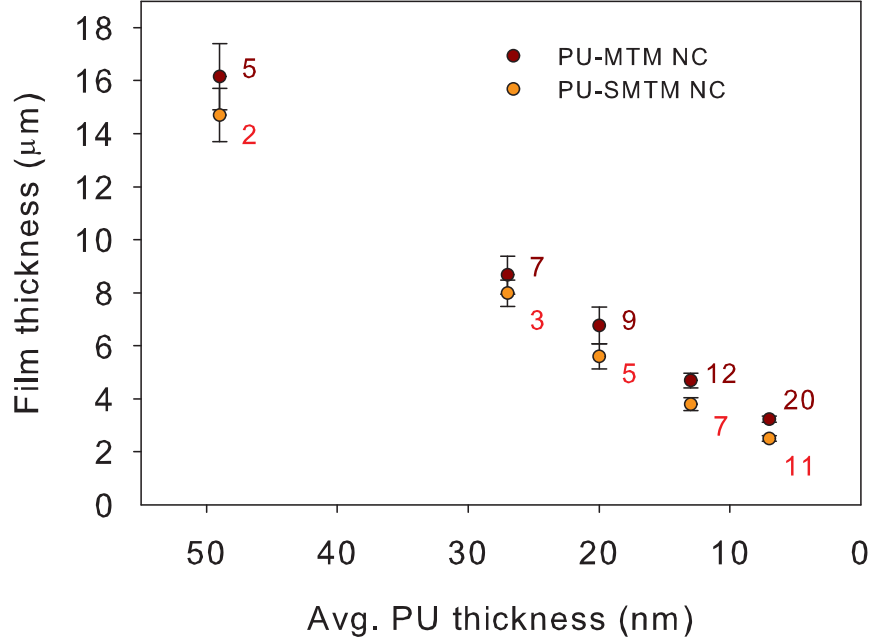


Figure 5.2: Film thickness of 300-bilayer nanocomposites as a function of average PU bilayer thickness. Numbers indicate the average volume fraction of nanoparticles in the PU-SMTM and PU-MTM nanocomposites.

nanocomposites as a function of average PU layer thickness is shown in Figure 5.2.

The number of silicate sheets in each nanoparticle layer is determined by comparing PU-MTM and PU-SMTM nanocomposites having the same average PU layer thickness. This calculation is shown below:

The average 300-bilayer film thicknesses of PU-MTM7 and PU-SMTM3 nanocomposites are $8.67 \mu\text{m}$ and $7.99 \mu\text{m}$ respectively with the same PU layer thickness. The thickness of the stratified layer in a PU-MTM7 nanocomposite is given by:

$$t_{strat} = 3 * 1nm + (3 - 1) * 0.28nm = 3.56nm \quad (5.1)$$

Since the average PU layer thickness remains the same for both nanocomposites, the number of silicate sheets in the stratified layer of PU-SMTM nanocomposites, given by n_{ss} , can

Sample Name	Avg. PU layer thickness (nm)	MTM loading (vol.%)
PU-SMTM2	49	2
PU-SMTM3	27	3
PU-SMTM5	20	5
PU-SMTM7	13	7
PU-SMTM11	7	11

Table 5.1: PU-SMTM nanocomposite nomenclature.

be calculated by

$$\frac{(8.67 - 7.99)}{300} * 1000 = 3.56 - (1 * n_{ss} + 0.28 * (n_{ss} - 1)) \quad (5.2)$$

This gives $n_{ss} = 1.25$. Hence, each layer of the nanoparticle contains approximately 1 silicate sheet and the series of PU-SMTM nanocomposites consisted of one SMTM nanoparticle layer in each layer.

The WAXD pattern for the PU-SMTM nanocomposites demonstrated a sharp peak at a 2θ angle of angle of 6.86° corresponding to a basal (001) spacing of 12.8 \AA . Figure 5.3 compares the WAXD pattern for PU-SMTM3 nanocomposite with that of PU-MTM7 nanocomposite. These two nanocomposites have the same PU layer thickness. The WAXD patterns for PU and MTM clay are also shown for reference. The increase in the intensity of the 6.86° peak in the PU-SMTM3 nanocomposite suggested a more in-plane orientation of MTM nanoparticles in the PU-SMTM nanocomposites in comparison to that in the PU-MTM nanocomposites. It should however be noted that single layer of silicate sheet should scatter x-ray at an angle lower than 6.86° and basal spacing of less than 12.8 \AA . The current result suggest that some of the MTM layers may consist of 2 silicate sheets. This requires further investigation and forms a part of the future work.

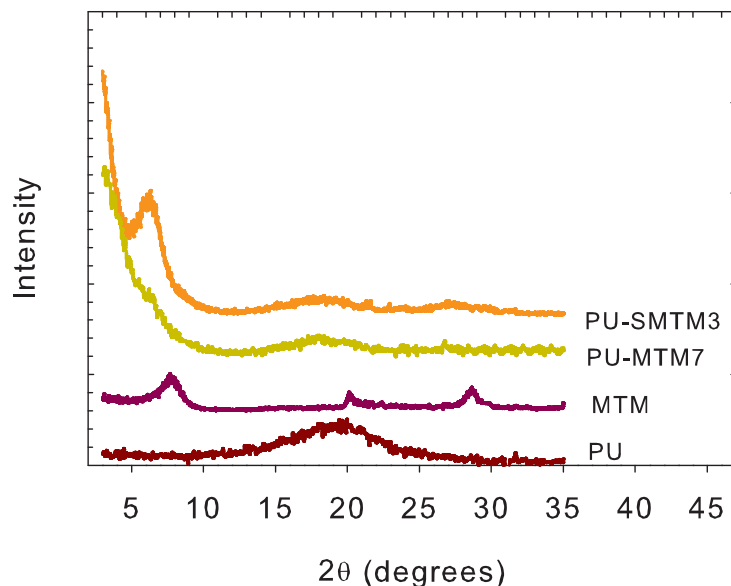


Figure 5.3: Wide angle X-ray diffraction patterns of PU, MTM clay, PU-MTM7 and PU-SMTM3 nanocomposites.

5.2 Mechanical Characterization

The series of PU-SMTM nanocomposites was tested in uniaxial tension at a strain rate of 0.005/s. The nominal stress-strain curves are shown in Figure 5.4 and the mechanical properties are compared with those of PU-MTM nanocomposites in Figures 5.5, 5.6 and 5.7.

The PU-SMTM nanocomposites demonstrated an increased yield strength and stiffness with an increase in volume fraction of nanoparticles. This is attributed to the constant dispersion of nanoparticles in the PU matrix. The stiffness, yield strength and the ultimate tensile strength increased beyond what was achieved for PU-MTM nanocomposites with similar PU layer thicknesses as shown in Figures 5.5, 5.6 and 5.7. For example, the PU-SMTM nanocomposite with 2 v.% nanoparticles demonstrated twice the modulus of a PU-MTM nanocomposite with 5 v.% MTM nanoparticles. The yield strength for this same pair of nanocomposites was ~ 1.6 times higher for the PU-SMTM nanocomposite than

that of the PU-MTM nanocomposite. Interestingly, the PU-SMTM nanocomposite even with a lower volume fraction of nanoparticles (i.e. 2 v.%) was less ductile than the PU-MTM nanocomposite (with 5 v.% nanoparticles) with the similar PU layer thickness (c.f. Figure 5.7). The ductile-to-brittle transition volume fraction and the MTM layer separation have reduced to lower values as depicted in Figure 5.8. While the critical MTM layer separation for PU-MTM nanocomposites was ~ 13 nm, it was found to be between 8 nm and 13 nm for the PU-SMTM nanocomposites.

Several important aspects can be assessed from these comparisons. It is important to experimentally probe the differences in the mechanical properties in PU-SMTM nanocomposites, which forms a part of the future work. Nevertheless, a hypothesis is presented below to explain the above results. The increase in stiffness and strength, even with a lower volume fraction of nanoparticles, in the PU-SMTM nanocomposites may be attributed to the removal of excess silicate sheets within a nanoparticle layer in SMTM layer. The nanoparticle layer in PU-SMTM nanocomposites is composed of only one silicate sheet as compared to the stratified layer of three silicate sheets in the PU-MTM nanocomposites. The increased number of silicate sheets in each layer (held together by water bridges) may have resulted in a reduced effective stiffness of MTM layer. Moreover, since there is only one MTM nanoparticle in each layer of PU-SMTM nanocomposite, each of these may be more tightly held to the PU matrix thus providing a larger stiffening and strengthening effect. The large stiffening effect is also attributed to the more ordered in-plane orientation of MTM nanoparticles as revealed by the X-ray diffraction data (c.f. Figure 5.3). This increase in the effective stiffening effect of nanoparticle layer may have resulted in larger stiffness and strength in the PU-SMTM nanocomposites. The shift of the critical separation to lower value in the PU-SMTM nanocomposites suggested further control of defects in this nanocomposites.

Moreover, we believe that the presence of stratified layer of MTM nanoparticles, held together by water bridges, in PU-MTM nanocomposites may have provided an additional

slip mechanism. As soon as a threshold load of the water bridges is reached, the MTM nanoparticles may have slipped providing additional deformation to these nanocomposites, leading to increased ductility. Moreover in such a configuration, the PU chains are more likely attached to several MTM nanoparticles and the relative slippage between the MTM nanoparticles may have resulted in additional deformation prior to failure. The absence of this mechanism in the PU-SMTM nanocomposites may possibly has resulted in the reduced ductility of PU-SMTM nanocomposites.

5.3 Summary and Conclusions

In this chapter, the role of stratified layers of nanoparticles in controlling the finite deformation response of layered nanocomposites has been investigated. The presence of stratified layers of nanoparticles lower the stiffness and strength but improves the ductility of the PU-MTM nanocomposites. The results have been explained via a hypothesis of the presence of a slip mechanism in the PU-MTM nanocomposites.

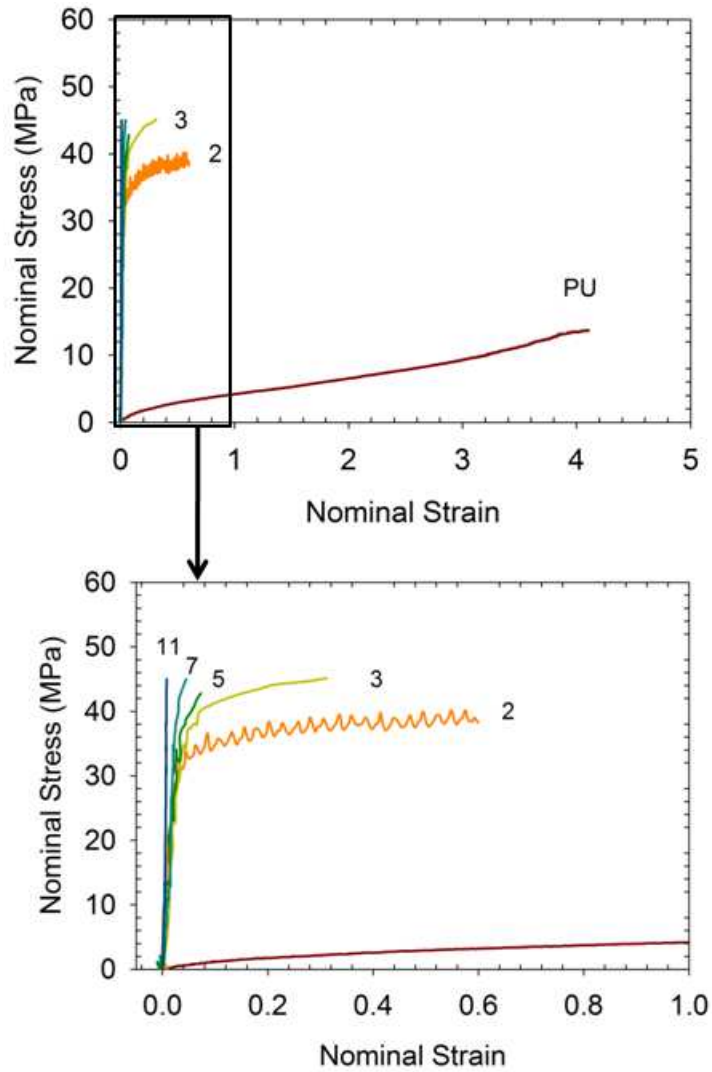


Figure 5.4: Representative nominal stress-strain responses of PU-SMTM nanocomposite as a function of volume fraction of MTM nanoparticles. The dog-bone specimens were loaded at a constant strain rate of 0.005/s at room temperature ($\sim 23^\circ\text{C}$) and a humidity of $\sim 30\%$ until failure. Numbers indicate the volume fraction of MTM nanoparticles.

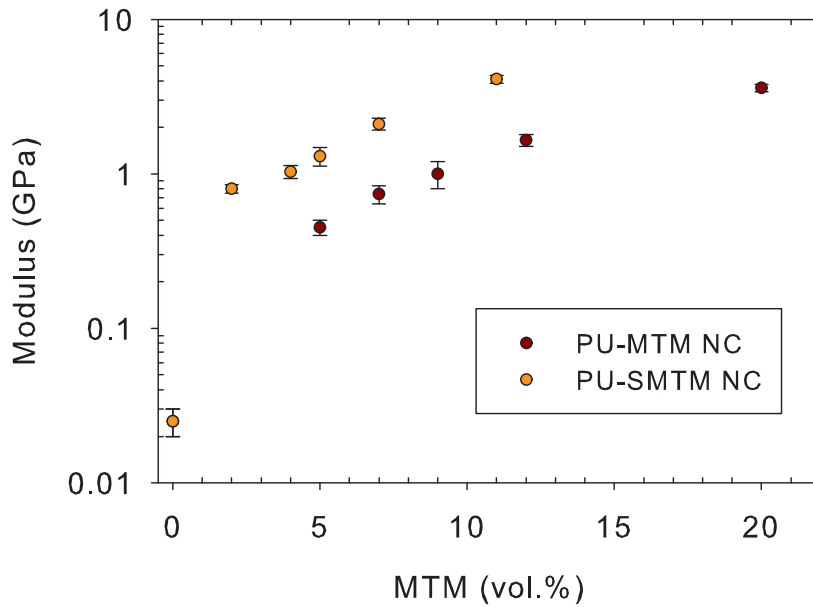


Figure 5.5: A comparison of the modulus of PU-SMTM nanocomposites with PU-MTM nanocomposites as a function of volume fraction of nanoparticles.

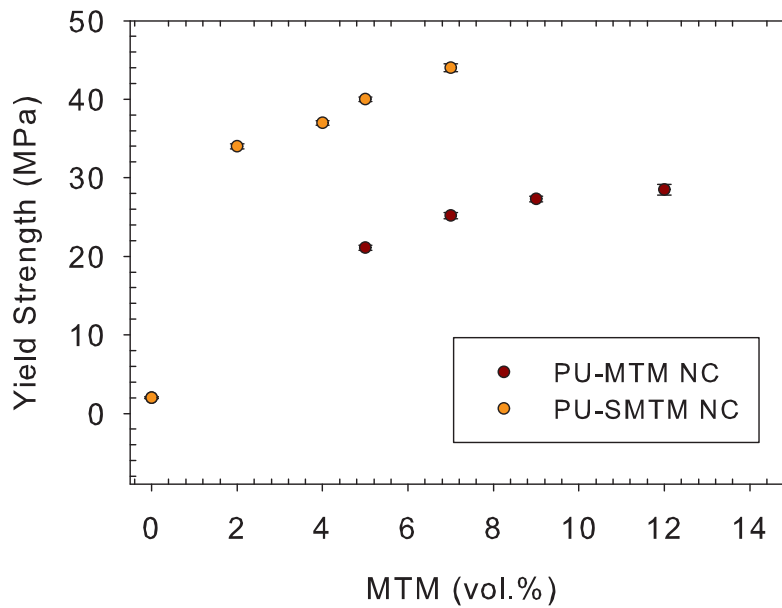


Figure 5.6: A comparison of the ultimate yield strength of PU-SMTM nanocomposites with PU-MTM nanocomposites as a function of volume fraction of nanoparticles.

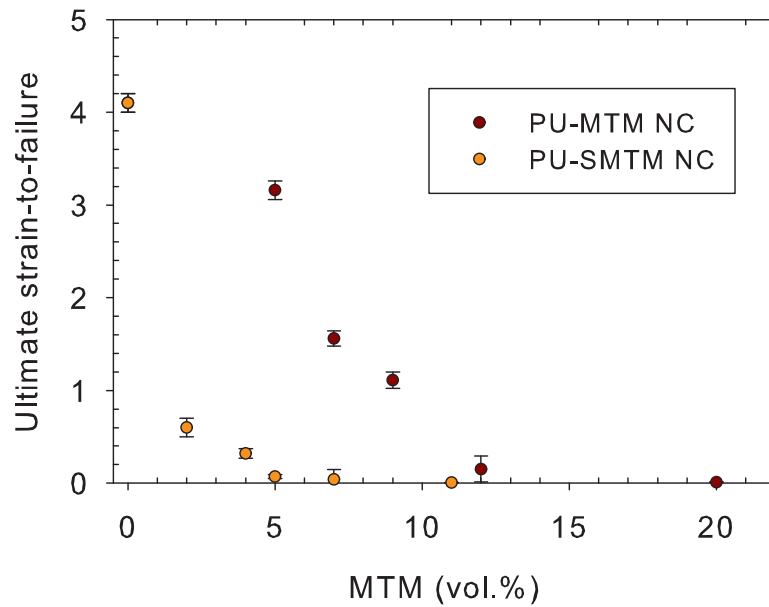


Figure 5.7: A comparison of the ultimate strain-to-failure of PU-SMTM nanocomposites with PU-MTM nanocomposites as a function of volume fraction of nanoparticles.

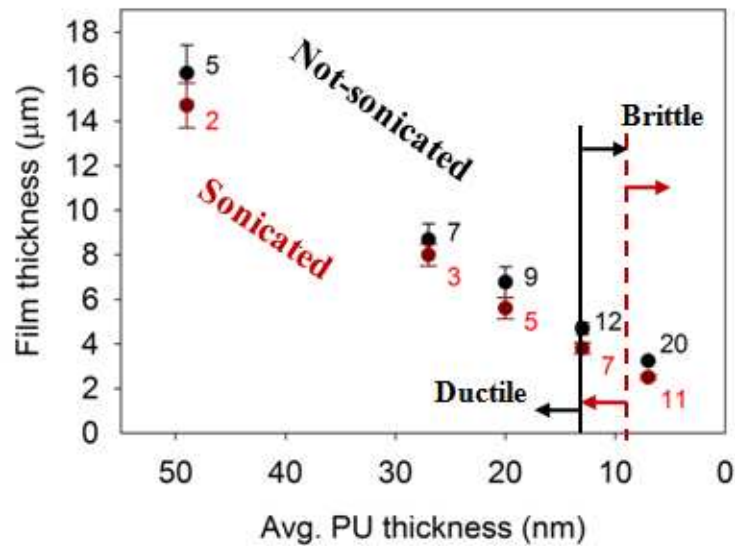


Figure 5.8: Film thickness of 300-bilayer nanocomposites as a function of average PU bilayer thickness. Numbers indicate the average volume fraction of nanoparticles in the PU-SMTM and PU-MTM nanocomposites. The vertical solid (in black) and dashed (in red) line shows the critical MTM layer separation in PU-MTM nanocomposites and PU-SMTM nanocomposites respectively. Below this separation, the nanocomposites demonstrate brittle behavior in the stress-strain response.

Chapter 6

Constitutive Model for PU and PU-MTM Nanocomposites

In this Chapter, a constitutive model capturing the major features of the stress-strain behavior of PU and multi-layered PU-MTM nanocomposites is developed. The first section of the Chapter introduces widely used constitutive modeling approaches for polymers. The second section discusses existing polymer composite models on polymer nanocomposites followed by a detailed description of the constitutive model developed for PU and multi-layered PU-MTM nanocomposites.

6.1 Constitutive Modeling of Polymers

The typical finite deformation response of many amorphous polymers consists of a viscoelastic response, followed by a viscoplastic yield phenomenon and then a strain hardening response. A few widely used constitutive models for the yield and strain hardening components of the polymer deformation have been briefly discussed below.

6.1.1 Yield Model: Argon Model

It is possible to think of yield and plastic deformation in polymers as a type of viscous flow. The first model to capture the yield of polymers was adopted from Eyring's in 1936 [107] which primarily described viscous flow in liquids. The Eyring model was readily adapted to describe the yield and plastic deformation of glassy polymers.

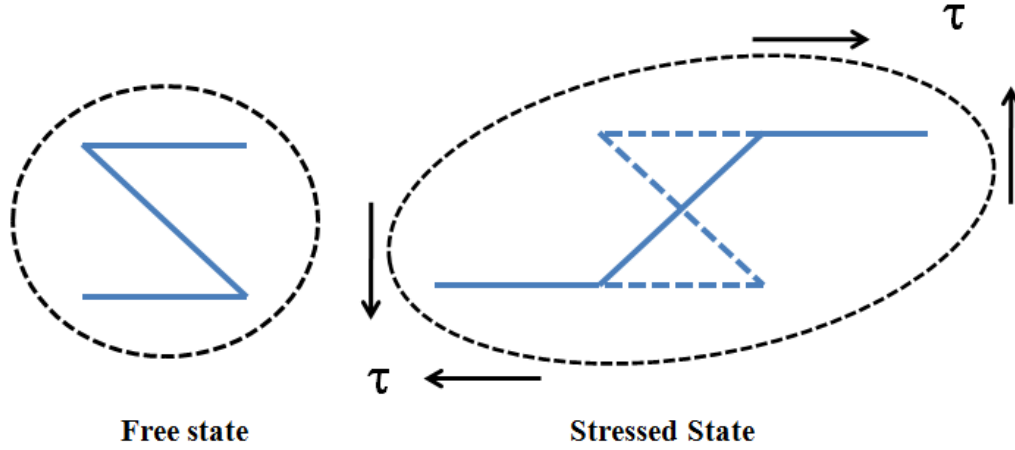


Figure 6.1: Argon kink pair yield model of intermolecular resistance in glassy polymers[108].

In early 1970 s, Argon developed a molecularly based yield model for glassy polymers that dealt with an intermolecular resistance to shear yielding [108]. In the model, the local shear strain was calculated for the rotation of a chain segment into the direction of principal stretch. The chain segment considered by Argon contained two “kinks” separated by a distance z along the chain, each with a bending angle ω (Figure 6.1). The resultant strain owing to the segment rotation is proportional to $a^2\omega^2z$ with a the radius of one chain or a cooperatively deforming bundle of chains. Argon determined the following inelastic strain rate equation when the applied shear stress is equal to the yield stress τ_y :

$$\dot{\gamma} = \dot{\gamma}_0 \exp\left[\frac{-\Delta U^*(\tau_y)}{kT}\right] \quad (6.1)$$

where $\dot{\gamma}_0$ is a pre-exponential or a fundamental rate factor, k is the Boltzmann constant, and ΔU^* is the maximum value of net energy ΔU of the kink pair of size $z=z^*$ from the elastic distortion of the surroundings having shear modulus G and Poisson’s ratio ν , and reduced by the work done by the applied stress τ . The inelastic strain rate is related to the yield stress τ_y , the athermal shear strength τ^* ($\tau^* = G/8$) and temperature T by

$$\dot{\gamma} = \dot{\gamma}_0 \exp\left[-\frac{G\omega^2 a^3}{kT} \left[1 - \left(\frac{\tau_y}{\tau^*}\right)^{5/6}\right]\right] \quad (6.2)$$

Equation 6.2 has been used extensively to capture the yield strength as a function of temperature and strain-rate in many glassy polymers. A few modifications to this Argon model have also been proposed to introduce the phenomenological treatment of polymer strain softening [89, 109, 110].

6.1.2 Strain Hardening Model: Eight Chain Model

The stress required to cause large deformations in polymers often contains a significant strain hardening component which is assumed to arise from configurational entropy changes in the polymer chains [108, 111]. Several elasticity theories, established upon either statistical mechanics or invariant-based/stretch-based continuum mechanics approaches have been developed in the literature [112, 113]. For modeling the strain hardening as a result of configurational entropy changes, the models derived from the statistical mechanics are used with the eight chain model as the most widely used model [114].

The statistical mechanics approach begins by assuming a structure of randomly-oriented macromolecular chains. In the Arruda-Boyce eight chain model, eight non-Gaussian chains emanate from the center of a cube to each of its corners as shown in Figure 6.2 [114]. The stretch on each chain in this symmetric network is given as the root mean square of the applied principal stretches, given as:

$$\lambda_{chain} = \frac{\sqrt{\lambda_1^2 + \lambda_2^2 + \lambda_3^2}}{\sqrt{3}} \quad (6.3)$$

where λ_1 , λ_2 and λ_3 are the stretches in the principal directions. When an external stress is applied, this network is stretched so that its configurational entropy decreases. The elastic strain energy in the deformed configuration is given as:

$$W = nk\theta[\beta_{chain}\lambda_{chain} + \sqrt{N}\ln(\frac{\beta_{chain}}{\sinh\beta_{chain}})] \quad (6.4)$$

where $\beta_{chain} = \mathcal{L}^{-1}(\frac{\lambda_{chain}}{\sqrt{N}})$, N is the number of links in the chain and θ is the temperature.

For incompressible cases, the principal Cauchy stresses are given as:

$$\sigma_i = \lambda_i \frac{\delta W}{\delta \lambda_i} + p \quad (6.5)$$

in which p is the pressure satisfying the boundary conditions. The principal stress-strain relation for the above strain energy is given by

$$\sigma_i - \sigma_j = \lambda_i \frac{\delta W}{\delta \lambda_i} - \lambda_j \frac{\delta W}{\delta \lambda_j} \quad (6.6)$$

$$\mathbf{T}^h = \frac{nk\theta}{3} \sqrt{N} \mathcal{L}^{-1}\left[\frac{\lambda_{chain}}{\sqrt{N}}\right] \frac{\lambda_i^2 - \lambda_j^2}{\lambda_{chain}} \quad (6.7)$$

where n and N are the two material constants. The eight chain model has been shown to successfully predict the large deformation stress-strain response of rubbery materials [53] as well as the strain-induced amorphous chain orientation in glassy polymers upon large deformation [115, 116].

6.1.3 Modeling of Polyurethane

The idea of introducing polyurethane (PU) was to bridge the gap between rubber and plastics since PUs offer the mechanical performance characteristics of rubber but can be processed as thermoplastics [117]. PUs are block copolymers with urethane backbone linkages composed of hard and soft segments, forming an alternating or block sequences. PUs are highly customizable and can have high elasticity or high stiffness depending on the ratio of hard and soft segments. The hard domains play the role of physical crosslinks and are responsible for the stiffness and strength of the PU. Since they also occupy significant volume

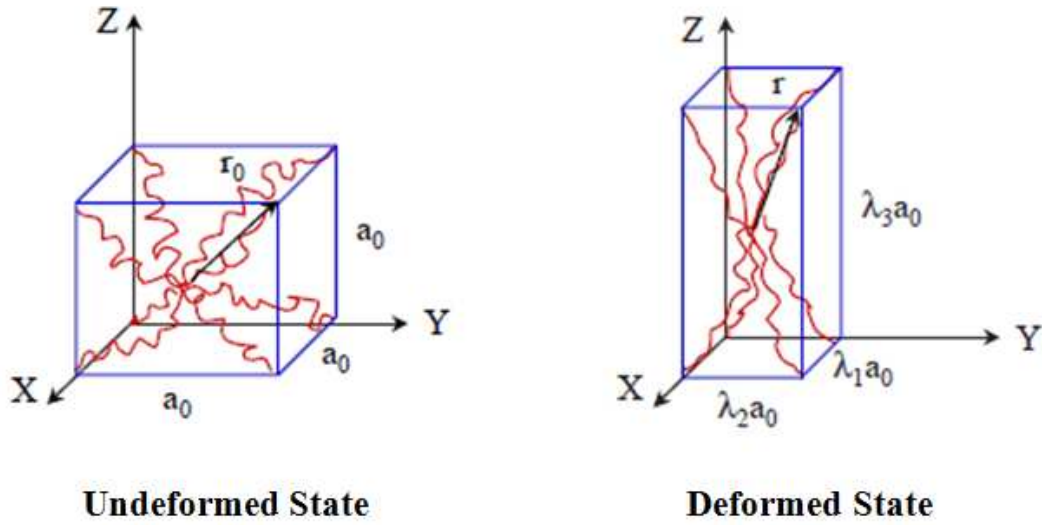


Figure 6.2: The unit cell of eight chain rubber elasticity model in an undeformed isotropic state and deformed state[114].

and are stiffer than the soft segments, they may be considered as effective nanoscale fillers that render a material behavior similar to that of a composites [109]. The soft segment, on the other hand, imparts a rubber-like behavior to the material.

A few constitutive model approaches for capturing the stress-strain behavior of PU have been used in the literature [109, 118]. Qi and Boyce [109] decomposed the material behavior into a rate-independent equilibrium part representing the soft segments and a rate-dependent viscoelastic-plastic part representing the hard segments of PU. The model adopted the concept of amplified strain using a strain amplification factor to account for the softening of equilibrium path. The amplification factor evolved with loading history due to structure reorganization of the soft and hard segments to increase the effective volume fraction of soft segments. As the volume fraction of hard segments decreases to zero, the Qi-Boyce model reduces to the Langevin chain based eight-chain model [114].

6.2 Modeling of Polymer-Clay Nanocomposites

Efforts to model the enhancements in mechanical properties of polymers that result from incorporation of rigid inclusions date back to early 1940s. Smallwood [119], in 1944, predicted the small strain Young's modulus of particle-filled solids. In the following year, Guth [120] theoretically estimated the stiffness of a rubber-carbon black system. These estimates were based on Einstein's work determining the viscosity of colloidal suspensions and emulsions [121]. Both estimates determined the stiffness of the system to be a non-linear function of the volume fraction of the filler particles and were accurate at low volume fractions. Since then, several models have been proposed to predict the enhancement in mechanical properties of composites with a few of them being variations of these estimates [122–131]. Many of these approaches have been found to provide robust predictions in the case of polymer nanocomposites. However, they have been employed to model only the elastic properties of nanocomposites with Halpin-Tsai [125] and Mori-Tanaka [126] models among the most widely accepted. Anthoulis and Kontou [131], however, have recently presented a model to formulate the elastoplastic response of epoxy-clay nanocomposites based on Mori-Tanaka theory [126] for the elastic stiffness and the Budiansky and Wu model [132] for the plastic response.

For the case of nanocomposites, computational chemistry approaches, including molecular dynamics (MD) simulations, have been utilized to investigate several structural and dynamic details at the atomic scale, e.g., changes in polymer mechanics in proximity to nanoparticles [133, 134] leading to an interphase and effects of filler sizes on mechanical properties of polymer nanocomposites [135]. In general, role of the interphase is vital in the enhancement of mechanical properties of nanocomposites as opposed to conventional composites. In nanocomposites, the surface area to volume ratio of nano-inclusions is several orders of magnitude higher than that of conventional fillers in composites. Thus, the interphase contributes significantly to the overall properties of the nanocomposite. Although research groups have investigated the properties of interphases using computational

approaches, experimental determination of properties and morphologies of the interphase is a challenging task. MD simulations, for example, have been used to determine the properties and size of the interphase with certain assumptions [130, 136]. These simulations yield the properties of polymer molecules in a time period of a few femtoseconds up to a few nanoseconds, several orders of magnitude in time lower than that required in the continuum-based calculations.

Many existing models for composites partition the total volume into particle and matrix domains. However, these can not be applied to nanocomposites due to the nanometer length scale morphology of nano-fillers and the modified matrix in proximity to these nanofillers leading to the interphase region [86, 100, 103, 137]. Considering this, several recent works have explicitly or implicitly used the idea of a pseudoparticle or an effective particle [128, 129, 138]. For instance, Sheng et al. [129] represented multiple sheets of intercalated clay and the inter-layer galleries as an effective particle. This was used in order to account for the potentially low shear modulus of inter-layer galleries.

In the present work, we have also utilized the idea of an effective particle to present the continuum-based model predictions of the finite deformation response of multi-layered polyurethane (PU)- montmorillonite (MTM) nanocomposites with a broad range of volume fractions of MTM nanoparticles [139]. Here, we model the nanocomposite as a heterogeneous material consisting of two phases: bulk PU and an effective particle. The effective particle is defined and employed to represent the stratified layer of MTM nanoparticles and the interphase region [86]. The overall mechanical properties of nanocomposites in terms of elastic stiffness, yield strength and strain hardening are predicted via a combination of constitutive models of Boyce, Parks and Argon [110] and Arruda and Boyce [114]. A notion of amplified strain in the interphase region is adopted to accommodate the applied strain owing to the limited strain in MTM nanoparticles [140]. The model predicts all the major features of the stress-strain constitutive response of multi-layered PU-MTM nanocomposites including linear elastic response, yield strength and post yield strain hard-

ening for all volume fractions of MTM nanoparticles, thus confirming the efficacy of the proposed constitutive model.

6.3 Modeling Approach

A schematic of a nano-structure that both approximates the actual nanocomposite structure and facilitates the mechanical modeling is shown in Figure 6.3 (A). Here, the total spatial volume is considered to be occupied by multi-layers of bulk PU matrix and effective particles. The thickness of bulk PU matrix is taken as t_{PU} . The effective particle is composed of stratified layers of MTM nanoparticles and the interphase region consisting of confined and stiffened PU chains. The stratified layer of MTM nanoparticles of thickness t_{strat} is composed of approximately three layers of MTM nanoparticles each 1 nm thick [86]. The thickness of the interphase on either side of the MTM stratified layer is t . The effective particle is employed as a basic element in the constitutive model to assess the influence of the MTM nanoparticles on the overall nanocomposite constitutive response. The volume fraction of effective particle, v_{ep} is determined as (c.f. Figure 6.3 (B)):

$$v_{ep} = \frac{t_{estrat} + 2t}{t_b} \quad (6.8)$$

i.e.

$$v_{ep} = v_p + \frac{2t}{t_b} \quad (6.9)$$

where t_{estrat} is a thickness equivalent to t_{strat} in Figure 6.3 (A), v_p is the volume fraction of MTM nanoparticles and t_b is the average bilayer thickness (Table 6.1). As evident from Equation 6.9, v_{ep} increases with an increase in t . In our modeling approach, we set t as a free fitting parameter and determine its value based on the convergence of the fitting procedure. v_{ep} also depends on both v_p and t and from Table 6.1 it is clear that t_b is itself dependent upon the particle volume fraction.

sample name	MTM loading v_p (v. %)	film thickness (μm)	avg. bilayer thickness, t_b (nm)	modulus (GPa)	yield strength (MPa)
PU	0	---	---	0.025 ± 0.005	2.0 ± 0.1
PU-MTM5	5	16.1 ± 1.2	53	0.45 ± 0.05	21.1 ± 0.3
PU-MTM7	7	8.7 ± 0.7	31	0.74 ± 0.10	25.2 ± 0.4
PU-MTM9	9	6.8 ± 0.7	24	1.0 ± 0.2	27.3 ± 0.4
PU-MTM12	12	5.1 ± 0.3	17	1.65 ± 0.15	28.5 ± 0.7
PU-MTM20	20	3.2 ± 0.1	11	3.6 ± 0.2	---

Table 6.1: Summary of structural and mechanical properties of PU and PU-MTM nanocomposites at a constant strain rate of 0.005/s at room temperature ($\sim 23^\circ\text{C}$) and a humidity of $\sim 30\%$ [86].

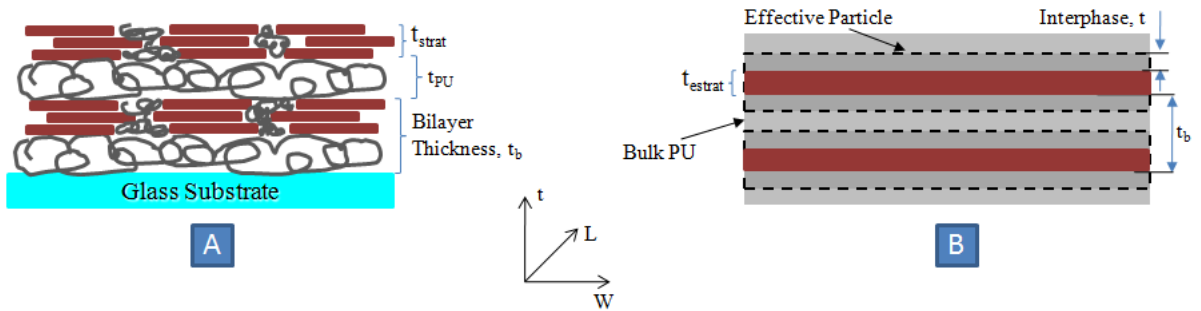


Figure 6.3: (A) A schematic of nanostructure of the PU-MTM nanocomposite[86]. (B) An equivalent representative volume element of the PU-MTM nanocomposite illustrating the interphase and effective particle concepts.

6.3.1 Modeling Constituents

In the current work, interest is in modeling the true stress-strain behavior of PU and PU-MTM nanocomposites.

The proposed three-dimensional constitutive model is decomposed into components representing the bulk PU and effective particle (Figure 6.4). The bulk PU used in the current nanocomposites has a significantly low volume fraction of hard segments [86, 118]. For modeling purposes we assume that the PU is composed of soft elastomeric segments only. Hence, we model the bulk PU with a non-linear hyperelastic rubbery spring element capturing the entropy change due to molecular orientation of PU chains. The component representing the effective particle comprises three elements: a linear spring to characterize the initial elastic response; a non-linear spring accounting for an anisotropic resistance to molecular chain orientation; and a visco-plastic dashpot accounting for the rate and temperature-dependent yield monitoring an isotropic resistance to chain segment rotation. We note from the representative volume element that the effective particle and bulk PU experience the same deformation (deformation direction is along W , c.f. Figure 6.3). Hence, the constitutive elements representing the effective particle are modeled “in parallel” to the hyperelastic rubbery spring element representing bulk PU (Figure 6.4).

The kinematics of three-dimensional finite strain deformation involves the macroscopic deformation gradient, \mathbf{F} , which maps the material from its reference configuration to its current configuration. Owing to the configuration of the constitutive elements (ref. Figure 6.4),

$$\mathbf{F} = \mathbf{F}^h = \mathbf{F}^e \mathbf{F}^p \quad (6.10)$$

where \mathbf{F}^h is the deformation gradient acting on the hyperelastic rubbery network, i.e. bulk PU; \mathbf{F}^e and \mathbf{F}^p are the elastic and plastic deformation gradients acting on the effective particle. \mathbf{F}^e can further be expressed into a left stretch tensor and a rotation tensor as

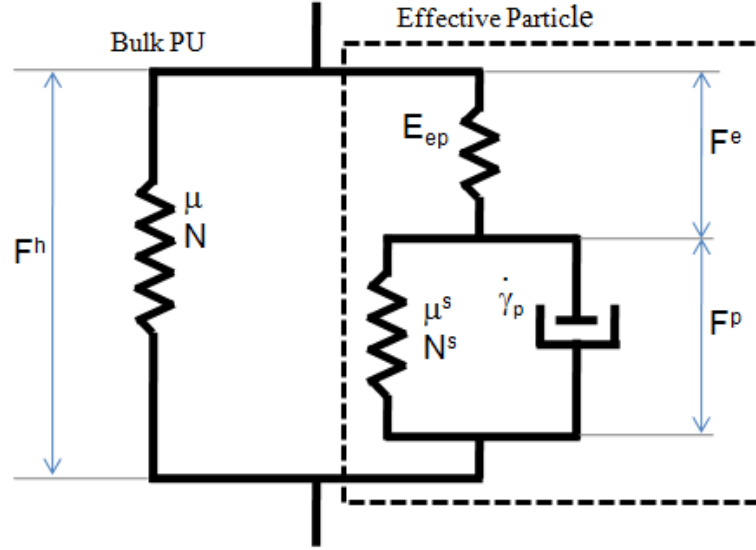


Figure 6.4: Mechanical analog of the proposed three-dimensional constitutive model for predicting the finite deformation response of PU-MTM nanocomposites[139].

$$\mathbf{F}^e = \mathbf{V}^e \mathbf{R}^e.$$

For the evolution of \mathbf{F} , \mathbf{F}^e and \mathbf{F}^p , we need $\dot{\mathbf{F}}$, $\dot{\mathbf{F}}^e$ and $\dot{\mathbf{F}}^p$. Hence, the velocity gradient, \mathbf{L} is given as

$$\mathbf{L} = \dot{\mathbf{F}}\mathbf{F}^{-1} = \mathbf{L}^e + \mathbf{F}^e \mathbf{L}^p \mathbf{F}^{e-1} \quad (6.11)$$

where \mathbf{L}^e and \mathbf{L}^p are the velocity gradients of the elastic and plastic deformation. \mathbf{L}^p can be expressed as the sum of a symmetric tensor, \mathbf{D}^p , the rate of deformation and a skew-symmetric tensor, \mathbf{W}^p , the spin as

$$\mathbf{L}^p = \mathbf{D}^p + \mathbf{W}^p \quad (6.12)$$

where \mathbf{W}^p can be reasonably assigned to be zero without loss of generality [110]. Hence, the evolution equation of the plastic deformation gradient can be simplified as

$$\dot{\mathbf{F}}^p = \mathbf{D}^p \mathbf{F}^p \quad (6.13)$$

with \mathbf{D}^p following a constitutive equation prescribed later.

The total Cauchy stress \mathbf{T} is distributed to the bulk PU and the effective particle as

$$\mathbf{T} = \mathbf{T}^h + \mathbf{T}^{ep} \quad (6.14)$$

where \mathbf{T}^h is the Cauchy stress acting on the bulk PU and \mathbf{T}^{ep} is the Cauchy stress acting on the effective particle. \mathbf{T}^h captures the resistance to entropy change in the bulk PU chains due to molecular network orientation and is modeled by the Langevin chain based eight-chain model capturing the large stretch hyperelastic behavior [114]. The eight-chain model has previously been used to model strain hardening in amorphous polymers [115, 141].

\mathbf{T}^h , taken to be deviatoric, is given as

$$\mathbf{T}^h = (1 - v_{ep}) \frac{\mu}{3J} \frac{\sqrt{N}}{\lambda_{chain}} \mathcal{L}^{-1} \left[\frac{\lambda_{chain}}{\sqrt{N}} \right] [\mathbf{B} - \lambda_{chain}^2 \mathbf{I}] \quad (6.15)$$

where $(1 - v_{ep})$ is the volume fraction of bulk PU, $J = \det \mathbf{F}^h$, $\mu = nk\Theta$ is the initial hardening modulus, N is the number of statistical rigid links between entanglements, $\mathbf{B} = \mathbf{F}^h \mathbf{F}^{hT}$ is the isochoric left Cauchy-Green tensor where $\langle . \rangle^T$ denotes the transpose of $\langle . \rangle$, $\lambda_{chain} = \sqrt{I_1/3}$ is the stretch on each chain in the network with $I_1 = tr(\mathbf{B})$ as the first invariant of \mathbf{B} . \mathcal{L}^{-1} is inverse Langevin function, defined as

$$\mathcal{L}(x) = coth(x) - \frac{1}{x} \quad (6.16)$$

providing the functionality that as λ_{chain} approaches its locking extensibility \sqrt{N} , the stress increases dramatically.

The linear-elastic element of the effective particle is constitutively governed by Hooke's law as

$$\mathbf{T}^{ep} = \frac{v_{ep}}{\det \mathbf{F}^e} \mathbf{C} [ln \mathbf{V}^e] \quad (6.17)$$

where \mathbf{C} is the fourth-order isotropic elasticity tensor. The coefficients of \mathbf{C} depend on the modulus, E_{ep} and poisson's ratio, ν of the effective particle [89].

As defined above, the effective particle is composed of modified PU chains and stiff MTM nanoparticles. Due to the presence of these MTM nanoparticles, the average strain in the modified PU chains is amplified over that of the macroscopic strain to accommodate the limited strain in the nanoparticles as suggested by Mullins and Tobin [140]. We incorporate this by amplifying the first invariant of stretch as suggested by Bergström and Boyce. [142]

$$\langle I_{1s} \rangle_m = X(\langle I_{1s} \rangle - 3) + 3 \quad (6.18)$$

where $\langle I_{1s} \rangle_m$ is the amplified first invariant of stretch, and $\langle I_{1s} \rangle$ is the first invariant of the stretch on the related modified PU chains. X is an amplification factor dependent on the volume fraction of MTM nanoparticles. It has a general form of $X = 1 + av_p + bv_p^2$. Here, we choose the amplification factor for the Guth model [120, 142], i.e. $a = 0.67g_p$ and $b = 1.62g_p^2$, hence resulting in $X = 1 + 0.67g_pv_p + 1.62g_p^2v_p^2$, where g_p is a constant typically between 4 and 10. Stress in the hyperelastic spring, \mathbf{T}^s , is given as [109]

$$\mathbf{T}^s = (v_p) \frac{\mu^s}{3J_s} \frac{\sqrt{N^s}}{\Lambda_{chain}^s} \mathcal{L}^{-1} \left[\frac{\Lambda_{chain}^s}{\sqrt{N^s}} \right] [\mathbf{B}^s - \Lambda_{chain}^{s2} \mathbf{I}] \quad (6.19)$$

where $J_s = \det \mathbf{F}^p$, $\mu^s = n^s k \Theta$, $\mathbf{B}^s = \mathbf{F}^p \mathbf{F}^{pT}$ is the isochoric left Cauchy-Green tensor, $\Lambda_{chain}^s = \sqrt{X(\lambda_{chain}^{s2} - 1) + 1}$ is the amplified chain stretch [109]. $\lambda_{chain}^s = \sqrt{I_1^s/3}$ is the stretch on each chain in the network with $I_1^s = \text{tr}(\mathbf{B}^s)$. It is worth noting that the elastic strain should also be ideally amplified over that of the macroscopic strain. We, however, neglect this effect here since the elastic strains are very small.

The plastic driving stress \mathbf{T}^p on the viscoplastic dashpot is determined from the tensorial difference between the total Cauchy stress on the effective particle \mathbf{T}^{ep} and the convected network stress from hyperelastic spring element, \mathbf{T}^s .

$$\mathbf{T}^p = \mathbf{T}^{ep} - \frac{1}{J_s} \mathbf{F}^p \mathbf{T}^s \mathbf{F}^{pT} \quad (6.20)$$

$$\tau = \sqrt{\frac{1}{2} (\mathbf{T}^{p*} \cdot \mathbf{T}^{p*})} \quad (6.21)$$

where \mathbf{T}^{p*} is the deviatoric portion of the plastic driving stress. The viscoplastic response activated once the isotropic resistance to chain segment rotation is overcome, is prescribed constitutively, through the rate of plastic deformation, \mathbf{D}^p , defined as

$$\mathbf{D}^p = \dot{\gamma}^p \mathbf{N}^p \quad (6.22)$$

where $\dot{\gamma}^p$ is the equivalent plastic shear strain rate and \mathbf{N}^p is a normalized tensor aligned with the deviatoric driving stress state,

$$\mathbf{N}^p = \frac{1}{\sqrt{2}\tau} \mathbf{T}^{p*} \quad (6.23)$$

$\dot{\gamma}^p$ is given as

$$\dot{\gamma}^p = \dot{\gamma}_0 \exp\left[-\frac{\Delta G}{k\Theta} \left\{1 - \left(\frac{\tau}{s_0}\right)\right\}\right] \quad (6.24)$$

where $\dot{\gamma}_0$ is the pre-exponential factor proportional to the attempt frequency, $s_0 = 0.077\mu/(1-\nu)$ is

the athermal shear strength with μ as the elastic shear modulus and ν as the poisson's ratio [109, 143].

ΔG is the zero stress level activation energy, k is the Boltzmann's constant and Θ is absolute temperature.

Material	Constitutive	Parameters elements	Constitutive equation
Bulk PU	Hyperelastic rubbery spring element	μ, N	$\mathbf{T}^h = (1 - v_{ep}) \frac{\mu}{3J} \frac{\sqrt{N}}{\lambda_{chain}} \mathcal{L}^{-1} \left[\frac{\lambda_{chain}}{\sqrt{N}} \right] [\mathbf{B} - \lambda_{chain}^2 \mathbf{I}]$
Effective Particle	Linear elastic spring element	E_{ep}, ν	$\mathbf{T}^{ep} = \frac{v_{ep}}{\det \mathbf{F}^e} \mathbf{C} [l n \mathbf{V}^e]$
	Hyperelastic rubbery spring element	μ^s, N^s	$\mathbf{T}^s = (v_p) \frac{\mu^s}{3J_s} \frac{\sqrt{N^s}}{\lambda_{chain}^s} \mathcal{L}^{-1} \left[\frac{\lambda_{chain}^s}{\sqrt{N^s}} \right] [\mathbf{B}^s - \lambda_{chain}^{s2} \mathbf{I}]$ $X = 1 + 0.67 g_p v_p + 1.62 g_p^2 v_p^2$
	Viscoplastic dashpot element	$\dot{\gamma}_0, \Delta G$	$\dot{\gamma}^p = \dot{\gamma}_0 \exp \left[-\frac{\Delta G}{k\Theta} \left\{ 1 - \left(\frac{\tau}{s_0} \right) \right\} \right]$

Table 6.2: Summary of constitutive model and material parameters[139].

6.3.2 Material Parameters Identification

The summary of the constitutive model and the required material parameters are listed in Table 6.2. The parameters needed to be determined for the bulk PU are μ and N (c.f. Equation 6.15). The true stress-strain constitutive response for PU is utilized in order to determine these parameters (c.f. Figure 4.11). The inverse Langevin function, $\mathcal{L}^{-1}(x)$, is evaluated by a Padé approximation given as:

$$\mathcal{L}^{-1}(x) = \frac{x(3 - x^2)}{1 - x^2} \quad (6.25)$$

We determine $\mu = 3.3$ MPa and $N = 32.0$. The locking stretch, hence, is $\sqrt{N} = 5.66$ [89]. Figure 6.5 shows the curve fitting using the estimated parameters. A parametric study of μ and N is also shown.

The material parameters needed to be determined for the effective particle are $E_{ep}, \nu,$

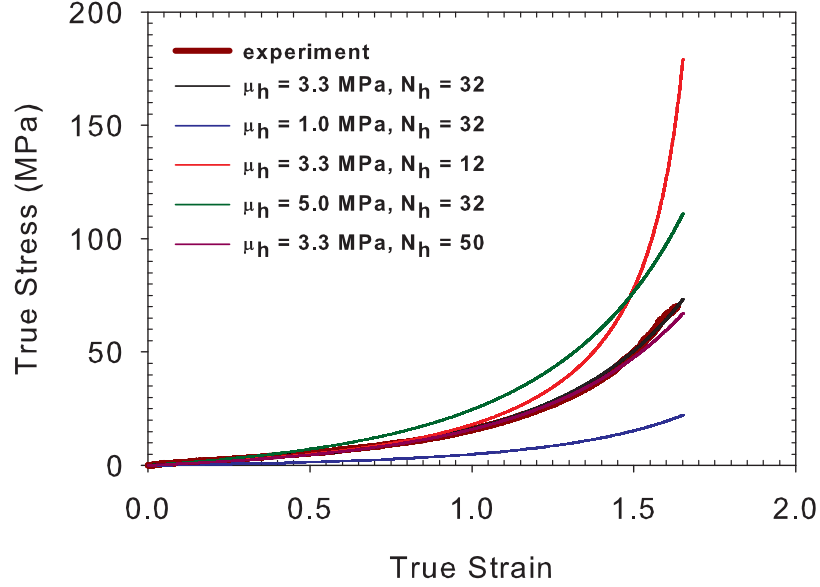


Figure 6.5: Material parameter identification and parametric study for the non-linear elastic spring for the bulk PU[139].

μ^s , N^s , $\dot{\gamma}_0$ and ΔG (c.f. Equations 6.17, 6.19 and 6.24). The Young's modulus of the PU-MTM nanocomposite, E_c , is the contribution from that of bulk PU, E_b , and effective particle, E_{ep} . E_b and E_c for the entire series of PU-MTM nanocomposites were determined experimentally (initial slope of true stress-strain curves, c.f. Table 6.1). E_{ep} was then determined from the traditional Voigt upper bound [144] for a linear elastic isotropic material as:

$$E_{ep} = \frac{E_c - (1 - v_{ep})E_b}{v_{ep}} \quad (6.26)$$

The Poisson's ratio, ν , is assumed to be 0.48. This is a reasonable assumption as PU is rubbery at room temperature (glass transition temperature, $T_g \sim -76^\circ\text{C}$ [86]). Additionally, changes in ν do not affect the results strongly. The material constants $\dot{\gamma}_0$ and ΔG are obtained by rewriting Equation 6.24 as

$$\tau = c \ln \dot{\gamma}^p + b, \quad (6.27)$$

where $c = \frac{s_0}{D}$, $b = \frac{s_0}{D}(D - \ln \dot{\gamma}_0)$, and $D = \frac{\Delta G}{k\Theta}$. These constants are determined experimentally from true stress-strain curves at two different strain rates in uniaxial tension. We choose the PU-MTM5 nanocomposite to determine these parameters (Figure 6.6). The nanocomposite demonstrates a dependence of yield strength on strain rate. The yield strength increased with an increase in the strain rate. The equivalent shear stress, τ and shear strain, γ^p are related to the uniaxial stress, σ and uniaxial strain, ϵ respectively by

$$\tau = \frac{\sigma}{\sqrt{3}}, \quad (6.28)$$

and

$$\gamma^p = \sqrt{3}\epsilon \quad (6.29)$$

The material parameters μ^s and N^s for the effective particle are determined by fitting the strain hardening portion of the true stress-strain response curve for the PU-MTM5 nanocomposite. We obtained $\mu^s = 3.6$ MPa and $N^s = 12.0$. The value of g_p is determined to be 10.

6.4 Modeling Results and Discussion

The three-dimensional constitutive model for PU and PU-MTM nanocomposites at finite deformations was implemented into MATLAB[®] (The Math Works Inc., Natick, MA) for uniaxial tension simulations. The material parameters for the bulk PU and the PU-MTM nanocomposites are listed in Table 6.3. The value of t was determined to be 2 nm. Figure 6.7 depicts the dependence of E_{ep} on v_{ep} and t . E_{ep} increases with an increase in v_p for a given t . This could be understood as an increased interaction between the MTM

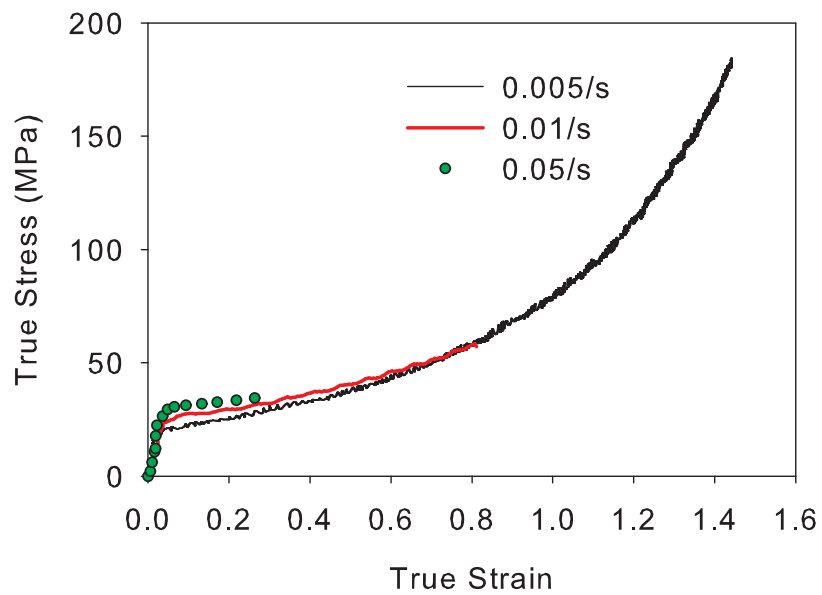


Figure 6.6: True stress-strain constitutive response of PU-MTM nanocomposites with 5 v.% MTM nanocomposites. The dog-bone specimens were loaded at a constant strain rates of = 0.005/s, = 0.01/s and 0.05/s at room temperature ($\sim 23^\circ\text{C}$) and a humidity of $\sim 30\%$ until failure[139].

Bulk PU		Effective	Particle					
μ (MPa)	N	t (nm)	E_{ep} (GPa)	ν	$\dot{\gamma}_0$ ($10^{49} s^{-1}$)	ΔG ($10^{-19} J$)	μ^s (MPa)	N^s
3.3	32.0	2	2.95(5)	0.48	1.01	5.25	4.8	10.0
			3.17(7)					
			3.46(9)					
			4.14(12)					
			5.90(20)					

Table 6.3: Material parameters for bulk PU and effective particle[139].

nanoparticles in the alternate layers. As v_p increases, the MTM layer separation decreases resulting in an increased particle interaction leading to an increased E_{ep} . E_{ep} decreases with an increased interphase thickness t . This could be attributed to the effective reduction in the volume of MTM nanoparticles with an increased t owing to a larger interphase.

Figure 6.8 shows the modeling and experimental results for uniaxial tension tests at $\dot{\epsilon} = 0.005/s$. The model results are in excellent agreement with the experimental results and demonstrate the ability of the constitutive model to accurately predict the constitutive response of PU-MTM nanocomposites across a wide range of volume fraction of MTM nanoparticles. It is important to note here that only the bulk PU and the PU-MTM5 nanocomposite response curves were fitted and used to determine the material parameters; the rest of the responses have been predicted with the same set of parameters. Clearly, the model captures the major characteristic features of PU-MTM nanocomposites response to large strain uniaxial deformation including the initial linear elastic response, volume fraction dependent yield strength and post-yield strain hardening. The model predicts the yield strength of PU-MTM20 nanocomposite at 44 MPa. However, the nanocomposite was brittle and fractured before yielding because of the complete transition of bulk PU into the interphase with restricted motion owing to the proximity of MTM nanoparticles. This is due to the fact that although in reality portions of the interphase regions may have overlapped but in our modeling approach, a fraction of PU is still present as the bulk matrix.

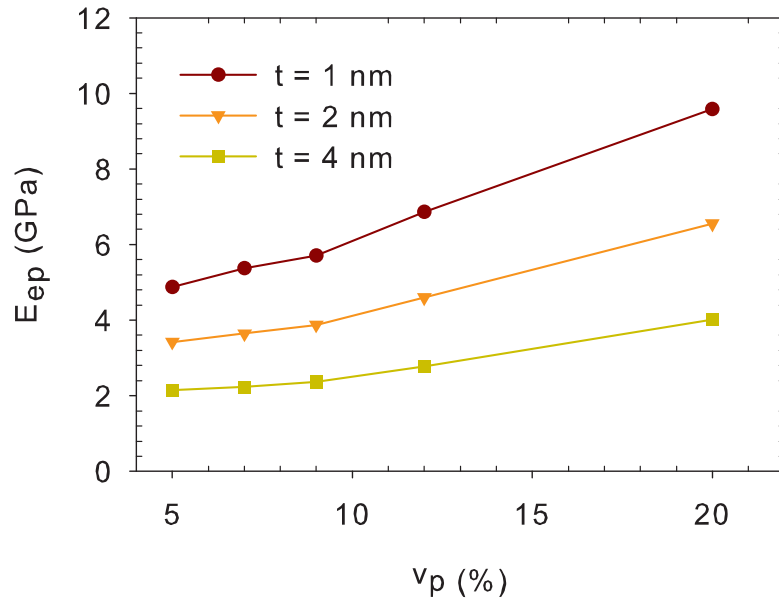


Figure 6.7: E_{ep} as a function of volume fraction of MTM nanoparticles, v_p and interphase thickness, t .

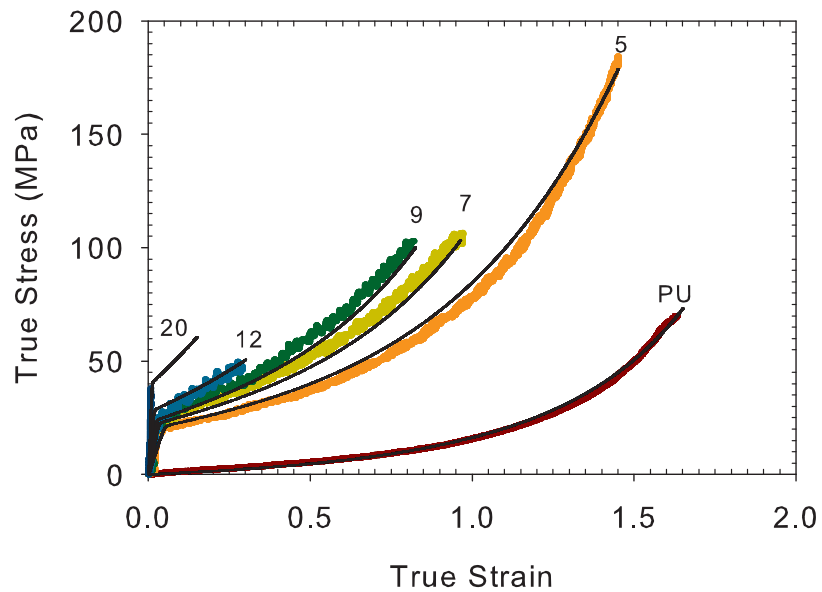


Figure 6.8: Model results (in black) and experimental results (in color) for the finite deformation constitutive response of PU and PU-MTM nanocomposites at a strain rate of $= 0.005/s$ at room temperature ($\sim 23^\circ C$) and a humidity of $\sim 30\%$ [139].

It is important to note that the application of amplified stretch was a significant reason for the success of the constitutive model to accurately predict the post-yield constitutive response of PU-MTM nanocomposites. Figure 6.9 shows the model results without the amplified stretch. Here, again the PU-MTM5 nanocomposite was used to determine μ^s and N^s . We found $\mu^s = 5.3 \text{ MPa}$ and $N^s = 4.5$. Clearly, the constitutive model without amplified stretch, although able to predict the initial elastic response and yield strength, is not able to predict the post-yield strain hardening response. This suggests that the mechanism of amplified stretch is vital in predicting the constitutive response of layered PU-MTM nanocomposites.

The presence of strain-rate dependent viscoplastic dashpot allows the prediction of the strain-rate dependent constitutive response of PU-MTM nanocomposites. Figure 6.10 shows the model predictions for finite deformation response of PU-MTM5 at $\dot{\epsilon} = 0.01/\text{s}$ and $0.05/\text{s}$. The model captures the strain-rate dependent yield strength and post-yield strain hardening response fairly well.

6.5 Summary and Conclusions

This paper presented several important aspects in the finite deformation response of multi-layered PU-MTM nanocomposites:

- The interphase region plays a vital role in the finite deformation response of the nanocomposites owing to large surface area to volume ratio. The effect of interphase is studied via an effective particle that consisted of stratified layers of MTM nanoparticles and the interphase region comprising modified PU matrix.
- The presence of MTM nanoparticles leads to large strain-gradients during the finite deformation of nanocomposites resulting in an increased strain-hardening response. The current constitutive model with the aid of amplified stretch accounts for the increase in these strain gradients increased with volume fraction of MTM nanopar-

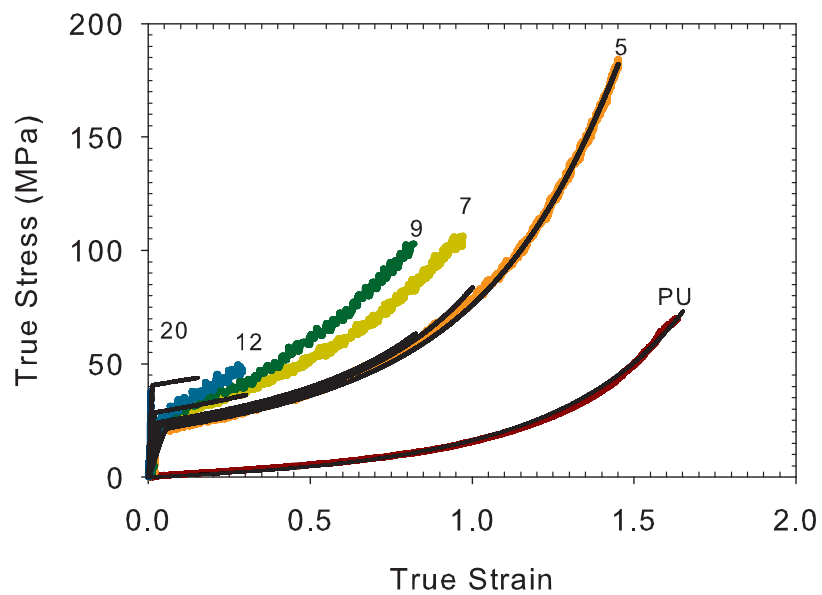


Figure 6.9: Model results (in black) and experimental results (in color) for the finite deformation constitutive response of PU and PU-MTM nanocomposites at a strain rate of $\dot{\epsilon} = 0.005/s$ at room temperature ($\sim 23^\circ C$) and a humidity of $\sim 30\%$. The model results are without any amplified stretch, i.e. $X = 1$ [139].

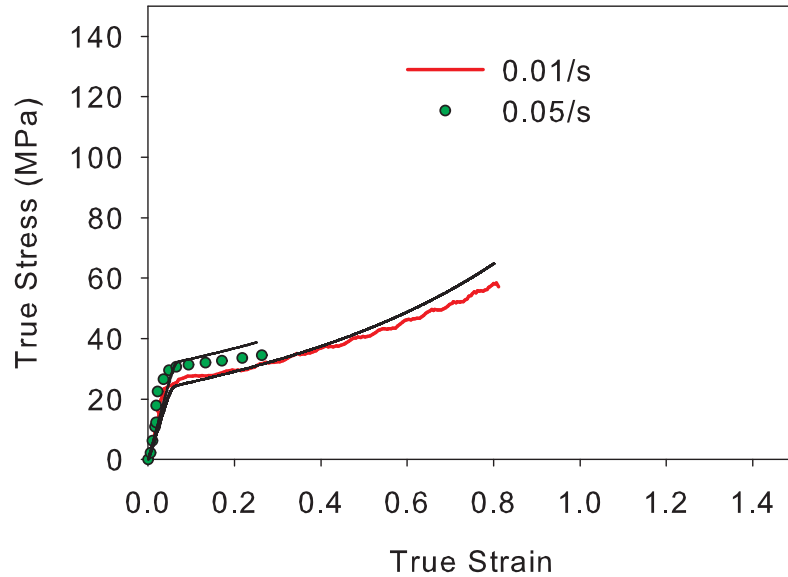


Figure 6.10: Model predictions (in black) and experimental results (in color) for the finite deformation constitutive response of PU-MTM5 at strain rates of = 0.01/s and 0.05/s at room temperature ($\sim 23^\circ\text{C}$) and a humidity of $\sim 30\%$ [139].

ticles. The stretch amplified as a function of the volume fraction of MTM nanoparticles was a significant reason for the success of the constitutive model to accurately predict the post-yield response of the PU-MTM nanocomposites.

- In the present work, the finite deformation response of nanocomposites is examined only at a room temperature and a limited strain-rate range but the current constitutive model may be used to predict temperature and strain-rate effects over broad ranges. Further experimental tests are needed to verify the efficacy of the constitutive model at high strain rates and/or where temperature effects play a role.

Chapter 7

Polymer-Nanoparticle Interface

In this Chapter, the role of the polymer-nanoparticle interface in controlling the finite deformation response of multi-layered polymer-clay nanocomposites is investigated. The interfacial interactions between the PU and MTM nanoparticles were altered by varying the effective charge density at the interface of PU and MTM nanoparticles. This was accomplished by diffusing negatively charged polyacrylic acid (PAA) through the PU matrix during nanocomposite fabrication using an exponential (e)-LBL manufacturing technique. The e-LBL manufacturing technique and the inherent diffusion mechanism in e-LBL are detailed in the subsequent sections.

7.1 Exponential Layer-by-Layer Nanocomposites

Some special combinations of polyelectrolytes have been found to exhibit so-called exponential growth (e-LBL) in film thickness, i.e. much faster than traditional LBL assembly growth [145]. e-LBL growth was first observed for a system of poly(L-lysine) (PLL) and alginate (ALG) polyelectrolytes in 1999 by Elbert et al. [146]. Elbert and co-workers observed that the thickness of dried PLL-ALG films increased exponentially with the number of deposited layers. They attributed the exponential buildup to the possibility of formation of a PLL-ALG complex coacervate gel on the film surface during successive depositions. Subsequently, several other combinations of polyelectrolytes for e-LBL assembly have been determined and several mechanisms have been attributed to such a rapid growth in film thickness [145, 147–152]. For example, Ruths et al. attributed the rapid growth

in poly(styrene sulfonate) (PSS)-poly(allylamine) (PAA) multilayer to increasing roughness leading to an increasing effective interfacial area with increasing thickness [147]. Pardo-Yissar and co-workers reported the swelling and increased absorbance of water in the PLL-PAA multilayer system [148]. Picart et al. [149] and Lavallo et al. [150] reported an “in-and-out” diffusion mechanism of the polyelectrolytes in PLL-hyaluronic acid films, resulting in the formation of a complex polycation-polyanion layer.

It can be easily noted that all of the above-mentioned e-LBL structures were based on purely polymeric or organic precursors. In this thesis work, however, the aim is to develop and characterize nanocomposites with inorganic MTM nanoparticles. To proceed further, we have asked the following questions: First, is it feasible to assemble MTM based e-LBL films? Second, is it possible to utilize the e-LBL assembly to investigate the role of polymer-nanoparticle interface in controlling the finite deformation response of multilayered nanocomposites? In Chapter 2, it was demonstrated that in an LBL nanocomposite (PVA-MTM nanocomposite), the MTM nanoparticles interact strongly with PVA leading to the formation of a nanocomposite with excellent mechanical properties. Moreover, the MTM nanoparticles were shown to form a densely packed region and were oriented parallel to plane of substrate. From the perspective of e-LBL assembly, the MTM nanoparticles were perpendicular to the direction of the diffusing polyelectrolyte. Such an orientation and organization appears to inhibit the diffusion of polyelectrolyte through the MTM layer, thus retarding the rate of growth of the film thickness. Although this is not favorable to the e-LBL assembly, it proves beneficial for invoking the investigation of the role of the polymer-nanoparticle interface in the multi-layered nanocomposites, which is detailed in the subsequent sections.

Polyacrylic acid (PAA), a negatively charged water-soluble polyelectrolyte, along with the PU used in previous chapters, form one such special combination of polyelectrolytes that exhibits the e-LBL growth. In this Chapter, we present results from the e-LBL assembly of a hybrid system composed of PU, PAA and MTM nanoparticles. Since PAA is

negatively charged it could be substituted for MTM nanoparticles. A typical e-LBL assembly process deposition cycle and deposition times is detailed in Chapter 3. Section 7.2 of this Chapter describes “uniform-layered” and “hierarchical-layered” PU-PAA-MTM nanocomposites manufactured with different deposition sequences. The e-LBL assembly and film architectures were characterized with scanning confocal microscopy, ellipsometry and scanning electron microscopy studies and were compared with the traditional LBL assembly. Mechanical properties of the e-LBL assembled films at low strain-rate in tension were characterized using the Tensile Tester detailed in Chapter 3. The Aluminum split-Hopkinson (ASHPB) was used to characterize the mechanical properties at high strain-rates in compression.

7.2 Uniform and Hierarchical-Layered Nanocomposites

e-LBL multi-layers of PU, PAA and MTM were assembled via two different deposition sequences to prepare uniform-layered and hierarchical-layered PU-PAA-MTM nanocomposites. While the uniform-layered PU-PAA-MTM nanocomposites were fabricated using the following deposition sequence: $(\text{PU/PAA/PU/MTM})_m$, hierarchical-layered PU-PAA-MTM nanocomposites were fabricated using the following deposition sequence: $(\text{PU/PAA}/(\text{PU/MTM})_n)_p$ (Figure 7.1). Here m and p are the number of deposition cycles and n is the number of times the (PU/MTM) bilayer is deposited within a cycle in the hierarchical-layered nanocomposites. For $n=1$, the deposition cycle is the same for both the uniform-layered and hierarchical-layered PU-PAA-MTM nanocomposites. Besides nanocomposites with MTM nanoparticles, a PU-PAA nanocomposite was also assembled with the deposition sequence: $(\text{PU/PAA})_l$.

Following an approach similar to the preparation of PU-MTM nanocomposites, a series of uniform-layered PU-PAA-MTM nanocomposites with different volume fractions of MTM nanoparticles was prepared by varying the thickness of the PU layer (Figure 7.2). The PU layer thickness was varied by changing the concentration of PU in solution. A

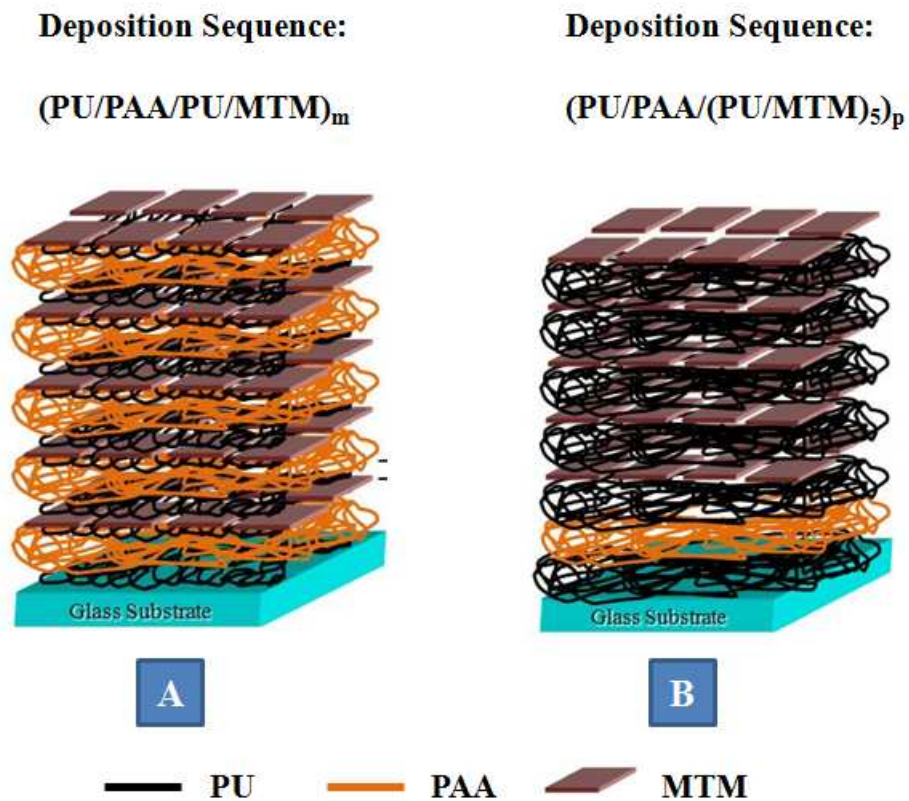


Figure 7.1: Schematic illustration of (A) a uniform-layered PU-PAA-MTM nanocomposite with a deposition sequence of $(\text{PU/PAA/PU/MTM})_m$; and (B) a hierarchical-layered PU-PAA-MTM nanocomposite with a deposition sequence of $(\text{PU/PAA}/(\text{PU/MTM})_5)_p$

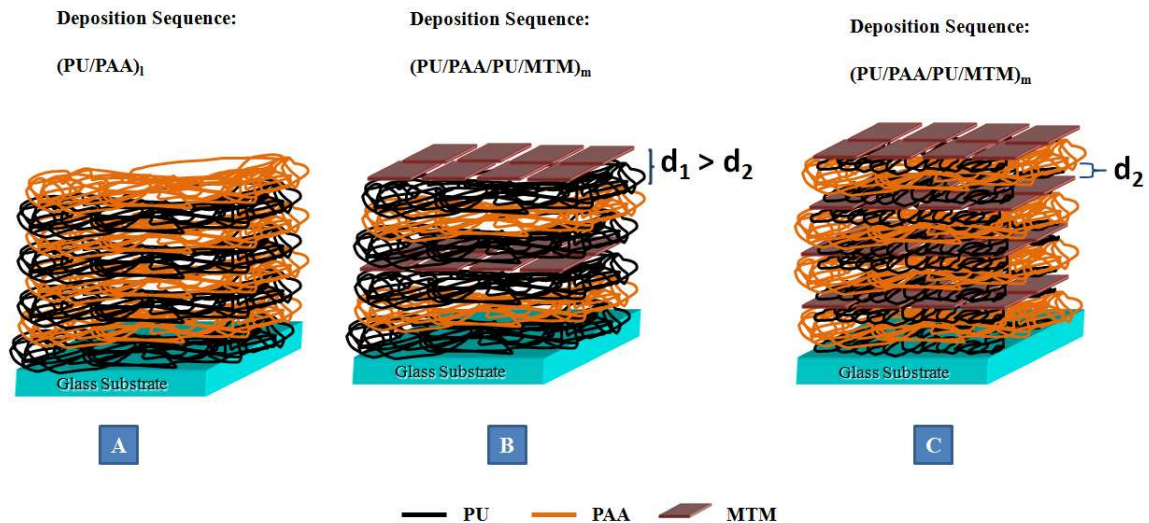


Figure 7.2: Ideal schematic of structure of (A) PU-PAA nanocomposite with 0 v.% MTM nanoparticles; uniform-layered PU-PAA-MTM nanocomposite with (B) lower volume fraction and (C) higher volume fraction of MTM nanoparticles

Sample Name	MTM loading (v.%)
PU-PAA	0
PU-PAA-MTM3	3
PU-PAA-MTM6	6
PU-PAA-MTM8	8

Table 7.1: Uniform-layered PU-PAA-MTM nanocomposite nomenclature.

PU-PAA nanocomposite without MTM nanoparticles was also prepared. The MTM volume fraction was varied from 0 v.% with $(PU/PAA)_l$ deposition sequence to 8 v.% with $(PU/PAA/PU/MTM)_m$ deposition sequence as shown in Table 7.1. It should be noted that the thickness of PAA layer is potentially a variable but it was held constant for all the e-LBL nanocomposites in this series.

Until this point of the thesis, the MTM volume fraction has always been varied by changing the thickness of the polymer layer. Here, the deposition sequence of the hierarchical-layered PU-PAA-MTM nanocomposites (deposition sequence: $(PU/PAA/(PU/MTM)_n)_p$) was utilized to vary the volume fraction of MTM nanoparticles by keeping the PU layer

Sample Name	Parameter, n	MTM loading (v.%)
PU-PAA-MTM6(h)	5	6
PU-PAA-MTM8(h)	10	8

Table 7.2: Hierarchical-layered PU-PAA-MTM nanocomposite nomenclature.

thickness constant while changing the value of the parameter n in the deposition sequence. A set of hierarchical PU-PAA-MTM nanocomposites was prepared with $n = 5$ and $n = 10$ as shown in Table 7.2 and Figure 7.3. Both PU-PAA-MTM6(h) and PU-PAA-MTM8(h) with 6 v.% and 8 v.% MTM nanoparticles respectively were composed of the same PU layer thickness. Note that the nanocomposites with 6 and 8 v.% MTM nanoparticles were prepared using both uniform and hierarchical deposition sequence (compare Tables 7.1 and 7.2). Section 7.4 will compare the mechanical properties of these nanocomposites and show how these nanocomposites were used to investigate the role of polymer-nanoparticle interface in controlling the finite deformation response of multi-layered nanocomposites.

7.3 Structural Characterization

The exponential growth for the PU-PAA system was verified for the first few bilayers by thickness characterization using ellipsometry as shown in Figure 7.4. The growth rate is consistent with previous e-LBL reports that have shown a similar growth for at most 30 bilayers and film thicknesses of no more than 15 μm . For subsequent layers and much larger thicknesses, however, the growth was linear but with unusually thick individual bilayers. This is shown in Figure 7.5 in which the film thickness, measured using SEM, is shown as a function of the number of bilayers. The growth in film thickness in the PU-PAA nanocomposite is also compared with that of traditional PU-MTM nanocomposites with 5 and 20 v.% MTM nanoparticles.

The rapid growth in the thickness of PU-PAA nanocomposites is attributed to the dif-

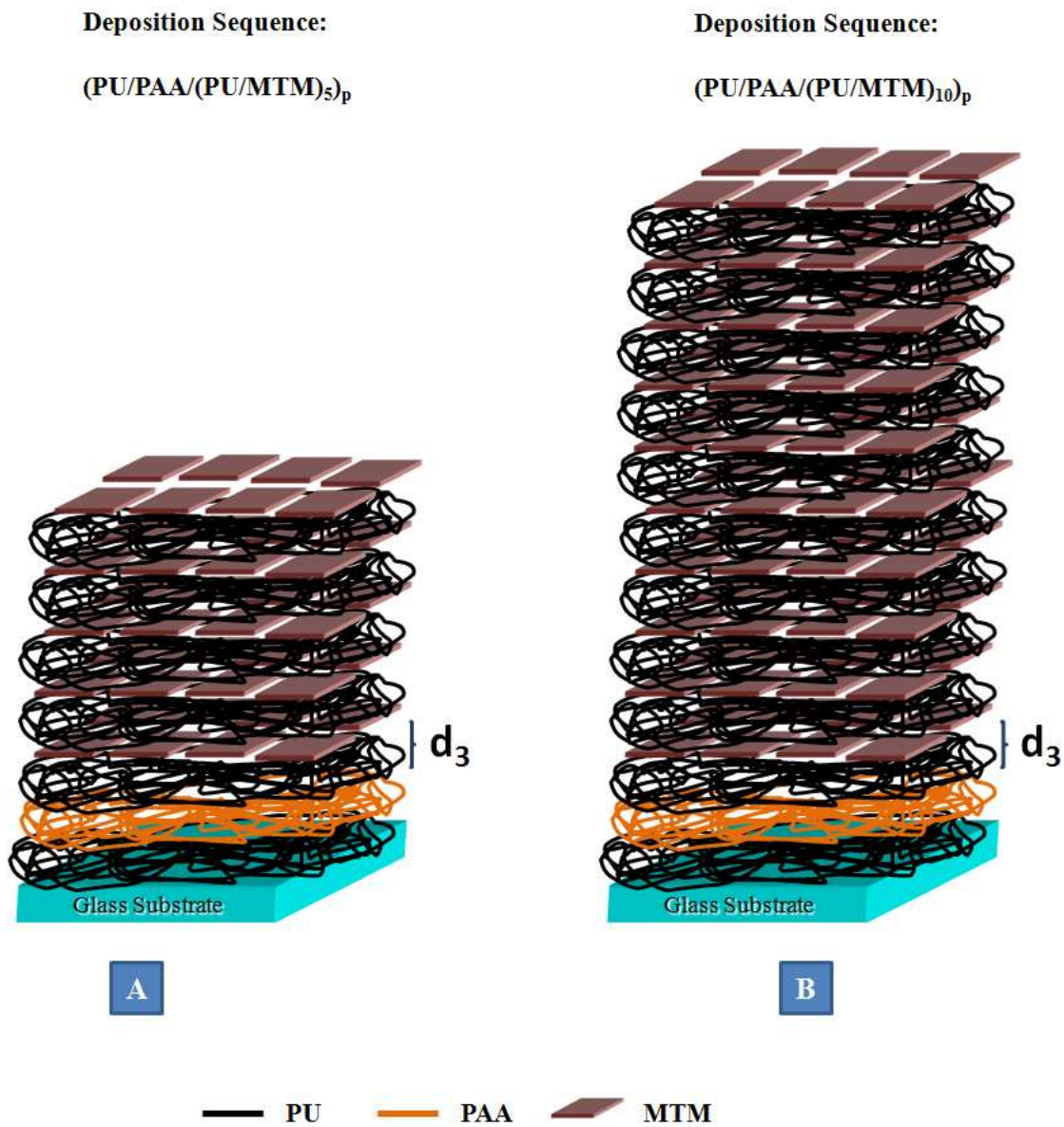


Figure 7.3: Ideal schematic of nanocomposite structures of (A) PU-PAA-MTM6(h); and (B) PU-PAA-MTM8(h) hierarchical-layered nanocomposites

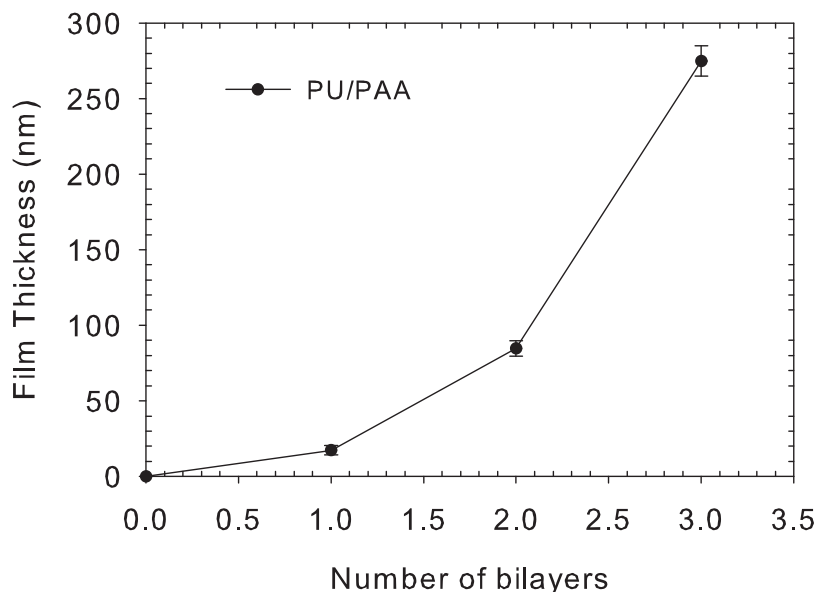


Figure 7.4: Film thickness for PU-PAA as function of number of bilayers. The growth is observed to be exponential for the first few bilayers[145].

fusion of polyelectrolytes through the film thickness. Previous work in our research group has verified this diffusion mechanism in a similar PAA based e-LBL system [145]. A system of poly(ethyleneimine) (PEI) and PAA was investigated in which the polyelectrolytes were conjugated with fluorescein isothiocyanate isomer I (FITC) and N-(5-aminopentyl)-4-amino-3,6-disulfo-1,8-naphthalimide, dipotassium salt (lucifer yellow cadaverine, LYC) fluorescent dyes, respectively, and their diffusion through the film thickness was observed with confocal microscopy. The microscopy images showed the diffusion of the polyelectrolytes through the film thickness, thus confirming the e-LBL growth mechanism for the PAA based system [145]. Further, the successful e-LBL growth was also verified in the thickness of uniform-layered PEI-PAA-MTM nanocomposites.

Figure 7.6 shows the film thicknesses in PU-PAA, PU-PAA-MTM6 and PU-PAA-MTM6(h) nanocomposites as a function of the number of bilayers measured using SEM. During deposition, the PU-PAA-MTM nanocomposite films, similar to PU-PAA films, be-

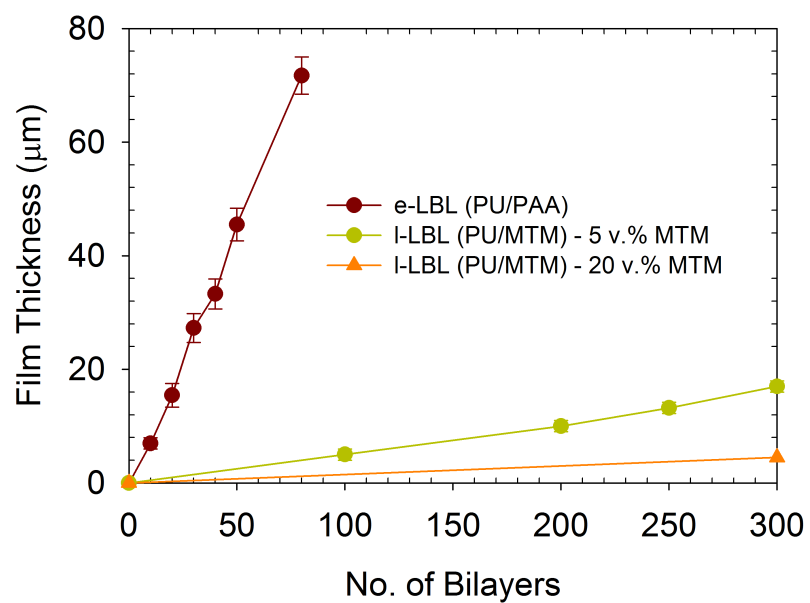


Figure 7.5: Film thickness in e-LBL PU-PAA nanocomposites as a function of the number of bilayers. Film thicknesses in the traditional PU-MTM LBL nanocomposite with 5 v.% and 20 v.% MTM nanoparticles as a function of the number of bilayers are also shown for comparison.

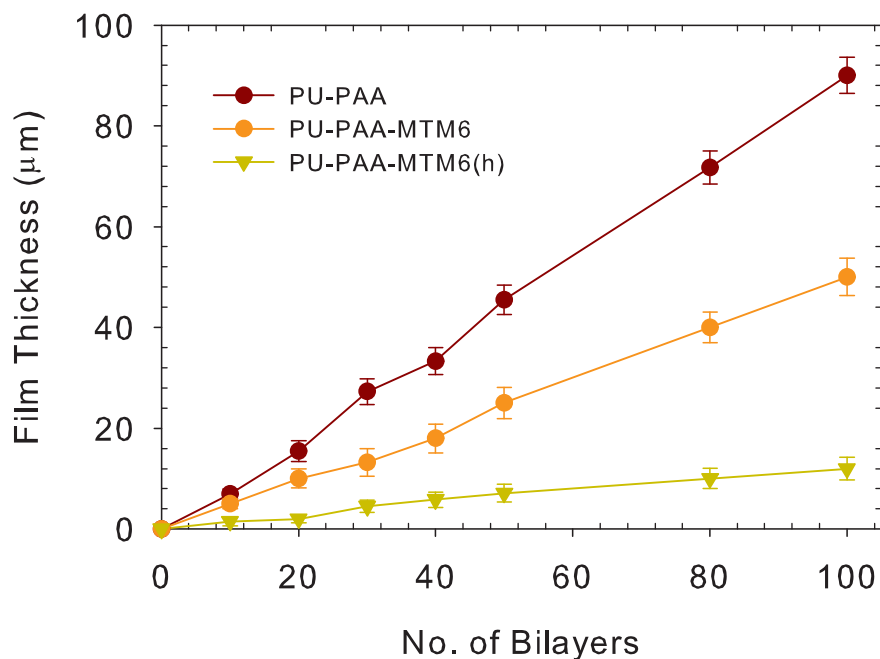


Figure 7.6: Film thickness in an e-LBL nanocomposite with and with out MTM nanoparticles as function of number of bilayers.

came strongly hydrated and had a gel-like appearance which was indicative of a successful e-LBL process. The diffusion of the negatively charged PAA through the positively charged PU matrix resulted in a complex PU/PAA layer. Noting the deposition sequences of the uniform and hierarchical-layered nanocomposites, this complex PU/PAA layer is formed more often in the uniform-layered nanocomposites (e.g. PU-PAA-MTM6) than the hierarchical-layered nanocomposites. The hierarchical-layered nanocomposites (e.g. PU-PAA-MTM6(h)) consisted of mostly PU/MTM layers. The formation of complex layer reduces the effective positive charge density and hence reduces the interfacial interactions between the polymer and MTM nanoparticles in the LBL assembly.

7.4 Mechanical Characterization

Figures 7.7 and 7.8 show the nominal and true stress-strain responses and Tables 7.3 and 7.4 summarize the mechanical properties of PU, PU-PAA and uniform-layered PU-PAA-MTM nanocomposites in uniaxial tension at room temperature ($\sim 23^\circ\text{C}$) and a humidity of $\sim 30\%$ with various volume fractions of MTM nanoparticles. The thickness of the nanocomposites reduced to approximately 0.5 times after hot-pressing and was used to determine the stresses. With the incorporation of PAA at the nanoscale in the PU matrix, the average Young's modulus and yield strength in the PU-PAA nanocomposite increased approximately 24 and 7.5 times and the average ultimate strain-to-failure reduced from 4.1 to 3.0 when compared with PU. The available literature data for PAA gives an ultimate tensile strength of $\sim 4.5\text{-}12.3$ MPa and an ultimate strain-to-failure of $\sim 0.02\text{-}1.16$ and they correspond to the hydrated state due to the highly hydroscopic nature of the polymer [85, 153, 154]. These data together with the results in Figure 7.7 and Table 7.3 suggest that the nanoscale diffusion of PAA through PU strongly interacts with the PU matrix, thus simultaneously stiffening and strengthening the matrix and reducing the average ultimate strain-to-failure of PU by $\sim 25\%$ though this failure strain is substantially larger than that of PAA. This latter result was remarkable in the sense that none of the previously reported e-LBL systems have approached this level of ductility [155]. With the incorporation of MTM nanoparticles, the yield strength and stiffness continued to increase with an increase in the MTM volume fraction (Figures 7.9 and 7.10). For example, PU-PAA-MTM3 demonstrated a 34 times increase in modulus over that of PU and a 1.5 times increase over that of PU-PAA. For this same nanocomposite, the yield strength increased ~ 8.5 and ~ 1.3 -fold when compared with PU and PU-PAA respectively. PU-PAA-MTM8 demonstrated a ~ 68 and ~ 3 -fold increase in modulus and ~ 21 and ~ 3 fold increase in yield strength over PU and PU-PAA respectively. The ultimate strain-to-failure, however, decreased with the volume fraction of MTM nanoparticles (Figure 7.11). This is consistent with our previous findings with traditional PU-MTM LBL nanocomposites (c.f. Chapter 4) in that both

Sample Name	Modulus (GPa)	Yield Strength (MPa)
PU	0.025 \pm 0.005	2.0 \pm 0.1
PU-PAA	0.6 \pm 0.2	14.8 \pm 1.1
PU-PAA-MTM3	0.85 \pm 0.3	19.2 \pm 1.2
PU-PAA-MTM6	1.1 \pm 0.25	24.5 \pm 1.1
PU-PAA-MTM8	1.7 \pm 0.15	42.5 \pm 1.5

Table 7.3: Summary of the mechanical properties of PU, PU-PAA and uniform-layered PU-PAA-MTM nanocomposites at a constant strain rate of 0.005/s at room temperature ($\sim 23^\circ\text{C}$) and a humidity of $\sim 30\%$. Numbers shown indicate average volume fractions of MTM nanoparticles.

increase in the MTM volume fraction or decrease in the PU layer thickness increase the volume of the confined PU matrix in proximity to MTM layer leading to reductions in the ultimate strain-to-failure.

The above increases in mechanical properties, specifically the modulus and strength, of the e-LBL nanocomposites are a result of two competing factors: volume fraction of MTM nanoparticles and interfacial interactions between the polymer matrix and MTM nanoparticles. The increase in the volume fraction of MTM nanoparticles is favorable to increasing the strength and modulus of the nanocomposites. However, an increased volume fraction of MTM nanoparticles in these e-LBL nanocomposites is achieved by reducing the thickness of the positively charged PU layer, as in LBL nanocomposites, but here the amount of PAA in the nanocomposites is constant. The reduction in the thickness of the PU layer and diffusion of PAA through the PU layer results in a reduction of effective positive charge density at the PU-MTM interface, thus weakening the interfacial interactions between the polymer matrix and the MTM nanoparticles. Intuitively, this should result in decreased modulus and strength due to less effective load transfer between the matrix and nanoparticle with increased volume fraction. However, although the interface weakens, the increased volume fraction of MTM nanoparticles results in an overall increased yield strength and modulus with increased MTM nanoparticle volume fraction.

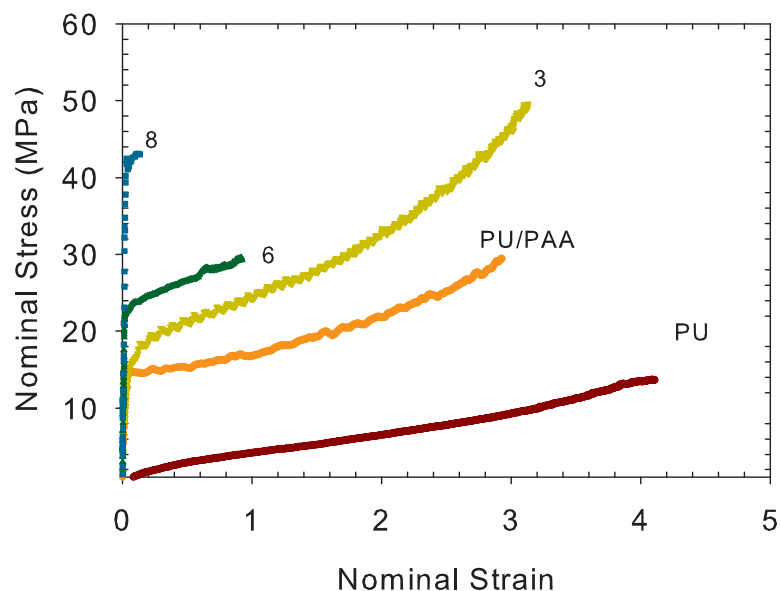


Figure 7.7: Representative nominal stress-strain response of PU, PU-PAA and uniform-layered PU-PAA-MTM nanocomposites. The dog-bone specimens were loaded at a constant strain rate of 0.005/s at room temperature ($\sim 23^\circ\text{C}$) and a humidity of $\sim 30\%$ until failure. Numbers shown indicate average volume fractions of MTM nanoparticles.

Sample Name	Ultimate Tensile Strength (MPa)	Ultimate Strain
PU	13.2 ± 0.9	4.10 ± 0.10
PU-PAA	29.6 ± 1.5	3.0 ± 0.3
PU-PAA-MTM3	49.5 ± 3.0	2.9 ± 0.35
PU-PAA-MTM6	30.1 ± 2.0	0.94 ± 0.2
PU-PAA-MTM8	43.5 ± 1.5	0.14 ± 0.04

Table 7.4: Summary of the mechanical properties of PU, PU-PAA and uniform-layered PU-PAA-MTM nanocomposites at a constant strain rate of 0.005/s at room temperature ($\sim 23^\circ\text{C}$) and a humidity of $\sim 30\%$.

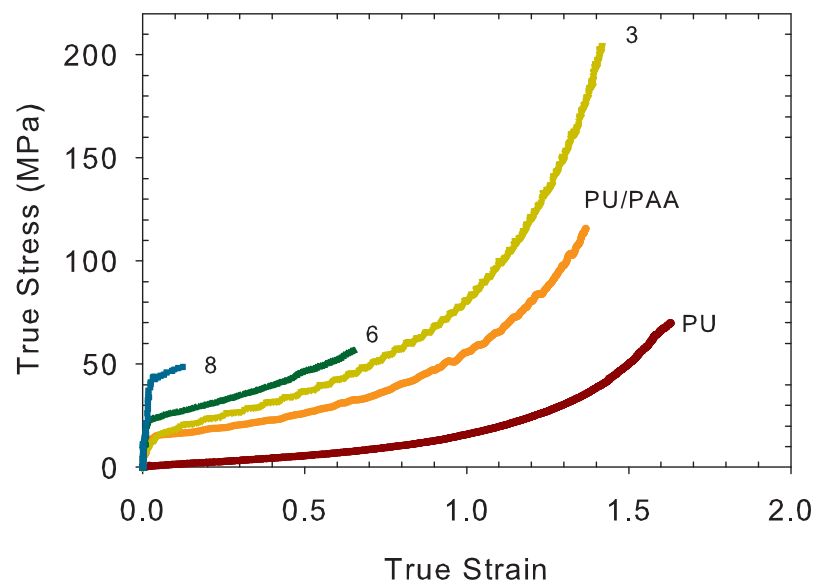


Figure 7.8: Representative true stress-strain response of PU, PU-PAA and uniform-layered PU-PAA-MTM nanocomposites. The dog-bone specimens were loaded at a constant strain rate of 0.005/s at room temperature ($\sim 23^{\circ}\text{C}$) and a humidity of $\sim 30\%$ until failure. Numbers indicate the volume fraction of MTM nanoparticles.

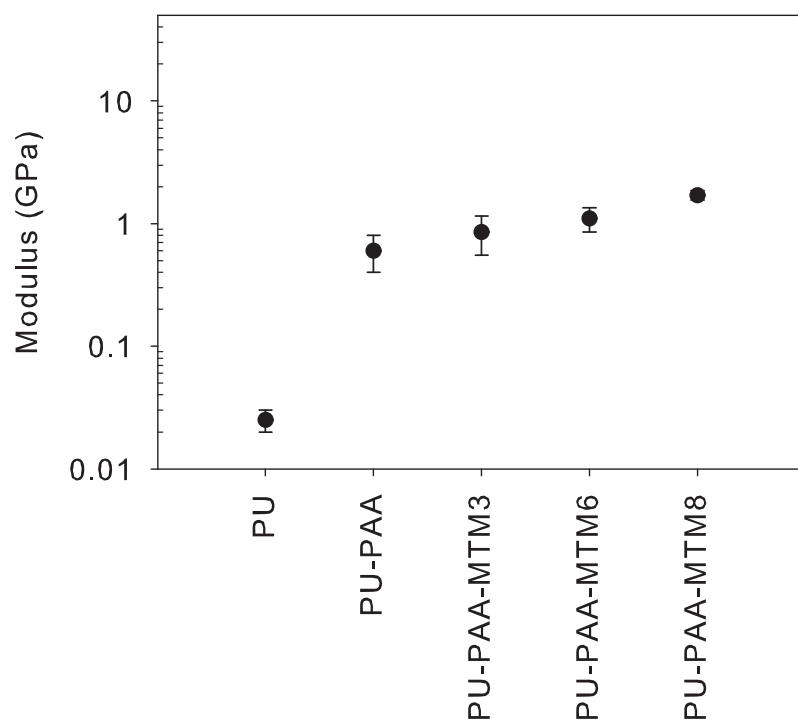


Figure 7.9: Comparison of modulus of PU, PU-PAA and uniform-layered PU-PAA-MTM nanocomposites.

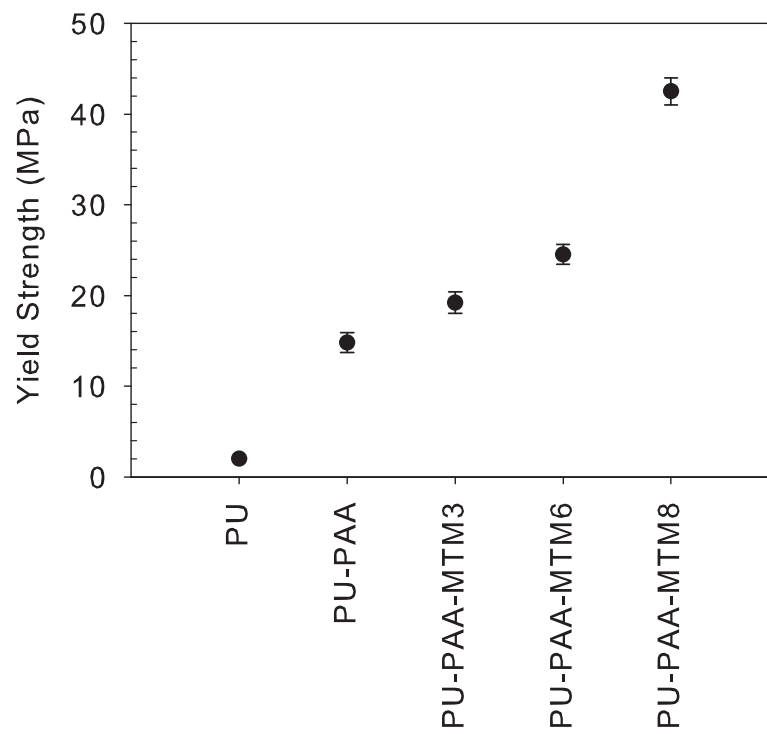


Figure 7.10: Comparison of yield strength of PU, PU-PAA and uniform-layered PU-PAA-MTM nanocomposites.

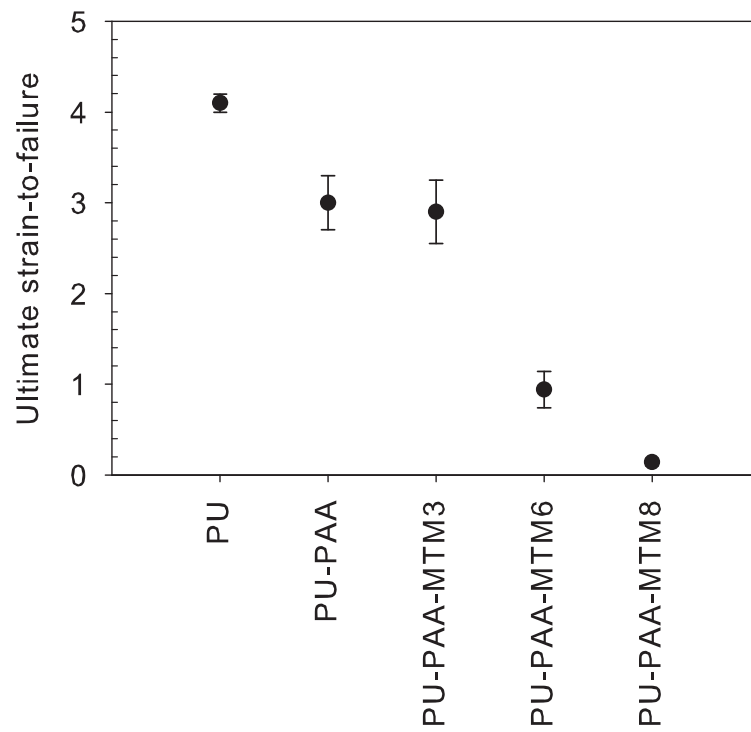


Figure 7.11: Comparison of ultimate strain-to-failure of PU, PU-PAA and uniform-layered PU-PAA-MTM nanocomposites.

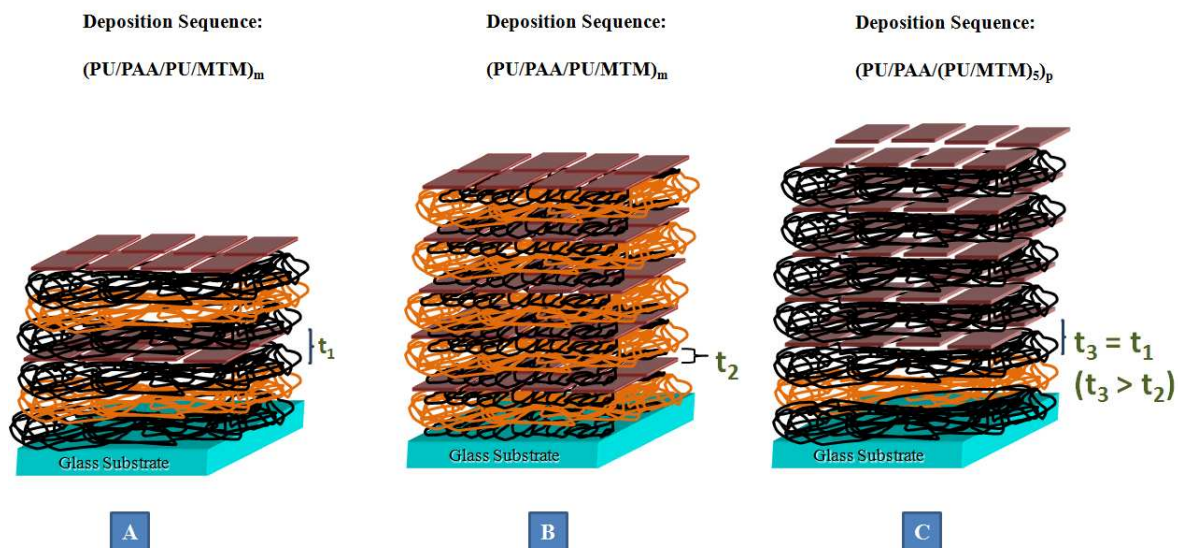


Figure 7.12: A schematic showing uniform-layered (A) PU-PAA-MTM3 and (B) PU-PAA-MTM6 nanocomposite, and a (C) hierarchical-layered PU-PAA-MTM6(h) nanocomposite.

Since the mechanical property enhancement in the uniform-layered PU-PAA-MTM nanocomposites involved the competing factors of the MTM nanoparticle volume fraction and interfacial interactions, it was difficult to explicitly investigate the role of the polymer-nanoparticle interface in controlling the finite deformation response of these nanocomposites. One systematic approach to investigate the role of polymer-nanoparticle interface is to modify the surface of MTM nanoparticles to alter the interfacial interactions between the PU matrix and the MTM nanoparticles. Processing techniques to modify the surface of MTM nanoparticles, specifically in the dry powdered form, have been used in the literature. However, this modification is difficult in the LBL assembled composites because of the fact that MTM nanoparticles are in the aqueous solution during the deposition process. Here we make use of the hierarchical-layered nanocomposites to investigate the role of PU-MTM nanoparticle interface in controlling the mechanical properties of PU-PAA-MTM nanocomposites.

Figure 7.12 shows a schematic of the PU-PAA-MTM3, PU-PAA-MTM6 and PU-PAA-MTM6(h) e-LBL nanocomposites. While the uniform-layered PU-PAA-MTM3 and PU-

PAA-MTM6 nanocomposites were assembled via the deposition sequence: (PU/PAA/PU/MTM)_m with PU layer thicknesses t_1 and t_2 respectively; the hierarchical-layered PU-PAA-MTM6(h) was assembled via the deposition sequence: (PU-PAA-(PU-MTM)₅)_p with PU layer thickness t_3 . The above three nanocomposites were assembled to possess the following structural relationships: the volume fraction of MTM nanoparticles in the uniform-layered PU-PAA-MTM6 nanocomposite was the same as that in the hierarchical-layered PU-PAA-MTM6(h) nanocomposite; the PU thickness t_3 is equal to t_1 ; and obviously t_2 is less than t_1 since PU-PAA-MTM6 has a higher loading of MTM nanoparticles than PU-PAA-MTM3 (c.f. Figure 7.12). Thus, both PU-PAA-MTM6 and PU-PAA-MTM6(h) are composed of 6 v.% MTM nanoparticles and may be used to explicitly investigate the role of the interface in controlling their properties since they differ mainly in the quality of PU-MTM interactions at the interface. Since the deposition sequence of PU-PAA-MTM6(h) nanocomposite consisted of more MTM layers than that of PU-PAA-MTM6 nanocomposite, it was believed to inherit a reduced diffusion of the polyelectrolyte like PAA through the film thickness. Hence, the interfacial interactions were stronger in the PU-PAA-MTM6(h) than in the PU-PAA-MTM6 nanocomposite.

Figure 7.13 shows the constitutive stress-strain responses of the three nanocomposites in tension at a strain-rate of 0.005 s^{-1} at room temperature ($\sim 23^\circ\text{C}$) and a humidity of $\sim 30\%$. It can be clearly seen that the PU-PAA-MTM6(h) demonstrated a higher modulus and yield strength when compared with PU-PAA-MTM6 nanocomposite containing the same volume fraction of MTM nanoparticles (Figures 7.14 and 7.15). Moreover, the PU-PAA-MTM6(h) nanocomposite demonstrated a simultaneous increase in the ultimate strain-to-failure as well when compared with PU-PAA-MTM6 nanocomposite (Figure 7.16). This is attributed to a larger PU layer thickness in the PU-PAA-MTM6(h) nanocomposite. Hence, with the aid of comparison between uniform-layered and hierarchical-layered nanocomposite, it is demonstrated that stronger interface resulted in increased strength and modulus of the nanocomposite. Moreover, a simultaneous increase in the modulus, strength, ductility

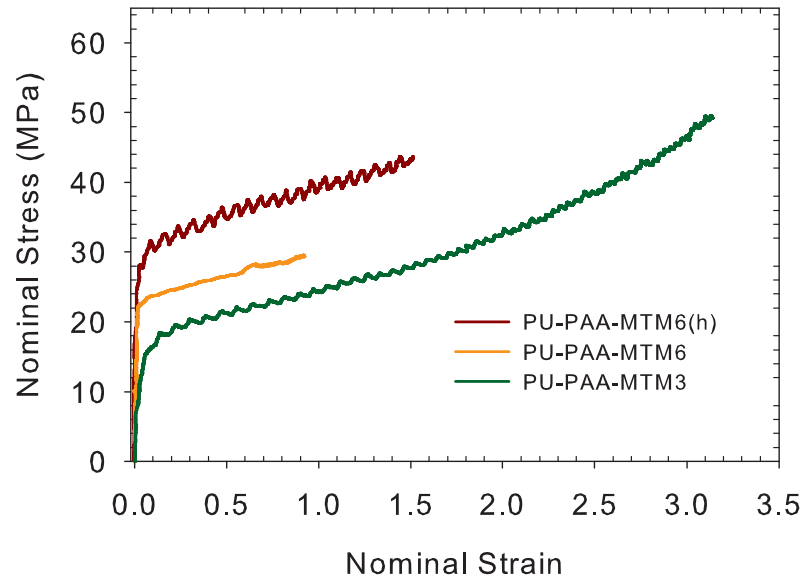


Figure 7.13: Representative stress strain constitutive response of PU-PAA-MTM3, PU-PAA-MTM6 and PU-PAA-MTM6(h) nanocomposites. The dog-bone specimens were loaded at a constant strain rate of 0.005/s at room temperature ($\sim 23^\circ\text{C}$) and a humidity of $\sim 30\%$ until failure.

and hence enhanced toughness was obtained in the hierarchical PU-PAA-MTM nanocomposite. Similar improvements in the strength, stiffness and ductility were also obtained in the PU-PAA-MTM8(h) over the PU-PAA-MTM8 nanocomposite as shown in Figure 7.16. In the next section, the results from high-strain characterization of e-LBL nanocomposites in compression are detailed.

7.5 High Strain-Rate Characterization and Potential Applications in Blast Mitigation

An effort to improve the survivability of structures under blast and ballistic applications has been of interest to the research community. Investigations have revealed that protection against blast and ballistic damage is improved by sandwiching rigid structures by soft com-

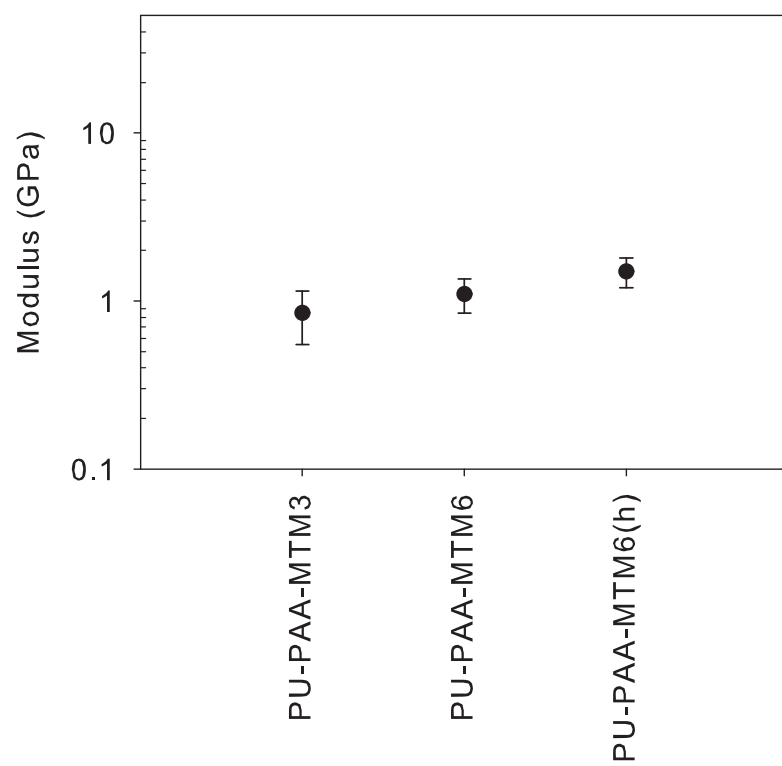


Figure 7.14: Comparison of modulus of PU-PAA-MTM3, PU-PAA-MTM6 and PU-PAA-MTM6(h) nanocomposites.

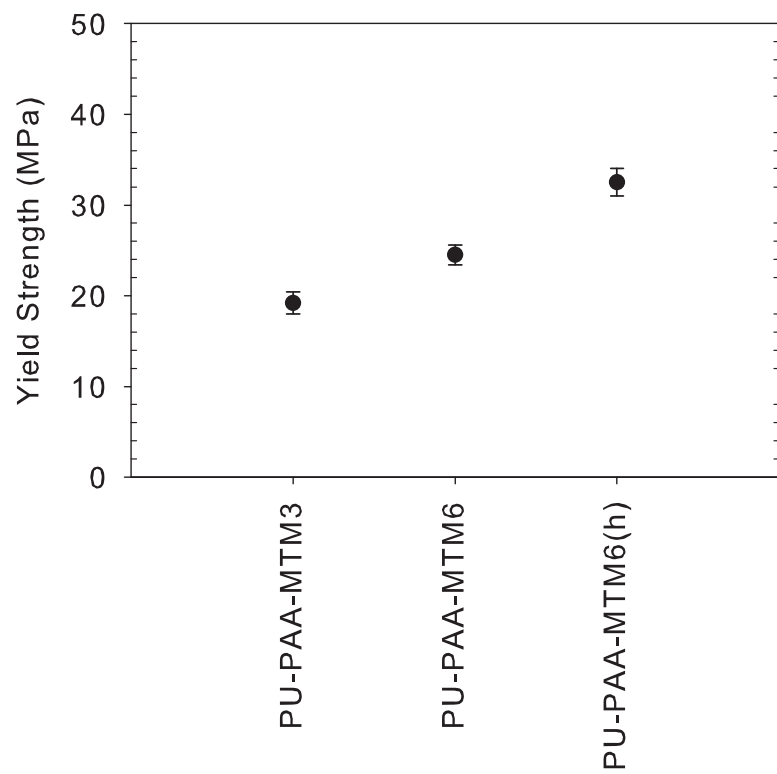


Figure 7.15: Comparison of yield strength of PU-PAA-MTM3, PU-PAA-MTM6 and PU-PAA-MTM6(h) nanocomposites.

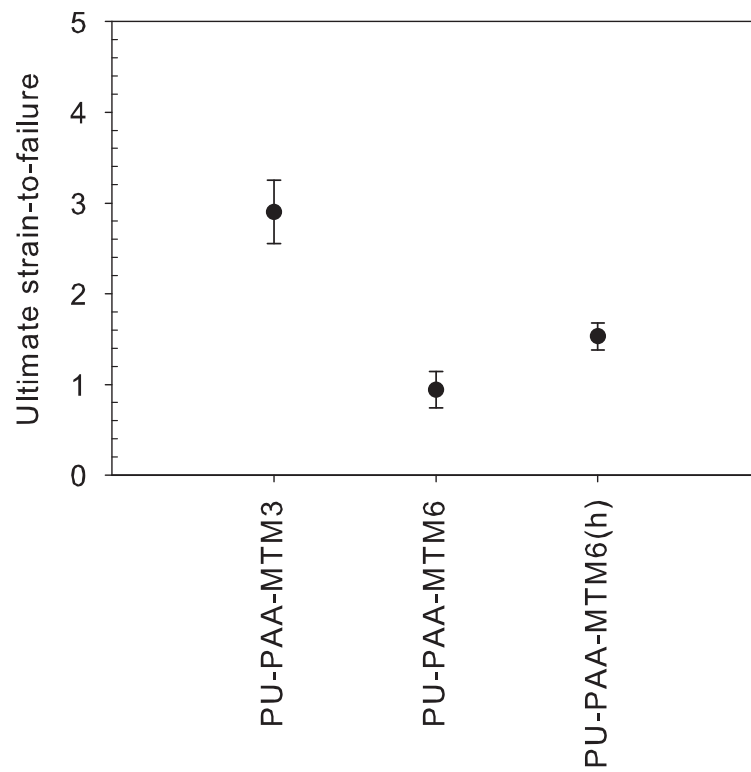


Figure 7.16: Comparison of ultimate strain-to-failure of PU-PAA-MTM3, PU-PAA-MTM6 and PU-PAA-MTM6(h) nanocomposites.

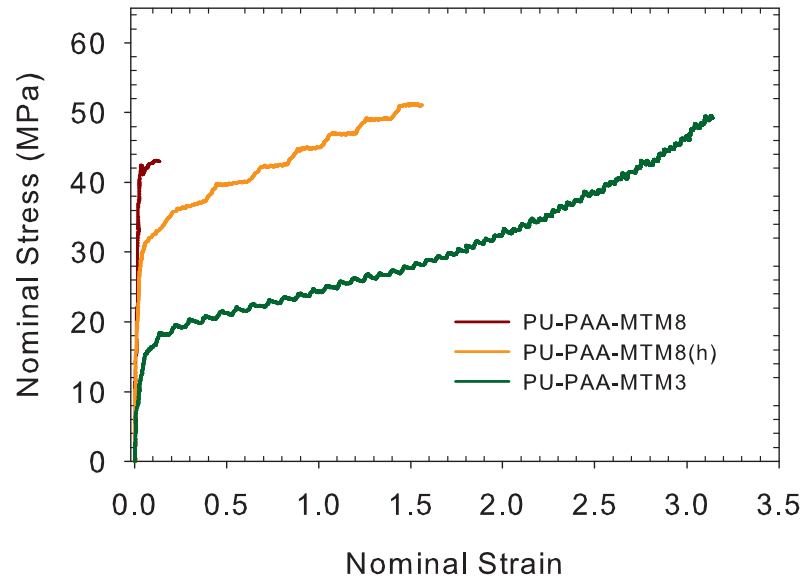


Figure 7.17: Representative stress strain constitutive response of PU-PAA-MTM3, PU-PAA-MTM8 and PU-PAA-MTM8(h) nanocomposites.

pliant materials [156–162]. Elastomers like polyurea and PU have been found to be strong choices for these soft materials [159, 162]. The strain rates in a typical blast impact loading increase rapidly and can reach values as high as $10^4/s$. Hence, a thorough understanding of the mechanical behavior of materials suitable for these applications at high strain rates is important.

The behavior of polyurea and PU at high impact rates for blast applications has been studied by several groups in the past [157, 162]. The interesting properties that separate these from other polymers are found to be the following: high strain-rate hardening, ability to sustain large deformations without undergoing failure, reduction in the overall momentum of shock wave, and absorption of the strain energy. In this work, the high strain-rate mechanical properties of PU-PAA and PU-PAA-MTM nanocomposites are investigated and compared with those of PU and polyurea.

High strain-rate compression tests were performed using the ASHPB detailed in Chap-

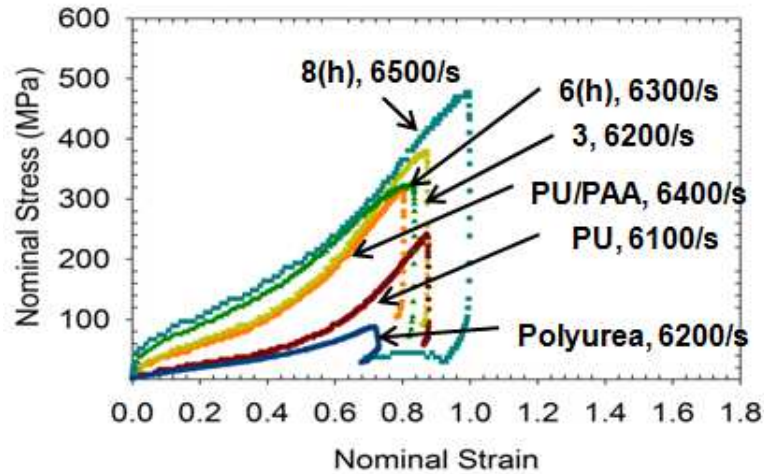


Figure 7.18: Representative nominal stress-strain response of polyurea, PU, PU-PAA and PU-PAA-MTM nanocomposites at high impact rate of about 6200 s^{-1} at room temperature ($\sim 23^\circ\text{C}$) and a humidity of $\sim 30\%$. The curves are labeled as (material, strain rate) and a and h in $a(h)$ represents the average volume fraction of MTM nanoparticles and hierarchical-layered nanocomposite.

ter 3. As shown in Figure 7.18, the stress-strain responses of polyurea, PU, PU-PAA and PU-PAA-MTM nanocomposites under impact compression at approximately constant strain rates of about 6200 s^{-1} and 7500 s^{-1} at room temperature ($\sim 23^\circ\text{C}$) and a humidity of $\sim 30\%$ have been successfully obtained via the ASHPB. PU-PAA-MTM6(h) and PU-PAA-MTM8(h) nanocomposites were chosen for high impact investigations over PU-PAA-MTM6 and PU-PAA-MTM8 due to their ability to sustain large deformations (in tension, c.f. Figures 7.13 and 7.16). Polyurea and PU deformed elastically with an evident post yield strain-hardening behavior (Figure 7.19). Both polyurea and PU show a less sensitive strain-rate dependent Young's modulus and yield strength. However, the post-yield hardening increased with the strain-rate for both polyurea and PU.

PU-PAA and PU-PAA-MTM nanocomposites were observed to demonstrate a strain-rate dependent Young's modulus (shown by the rate sensitive initial stiffness), and a rate sensitive yield strength (e.g. 8 MPa increase per decade of strain-rate from 6500 s^{-1} to 7500 s^{-1} for PU-PAA-MTM8(h) nanocomposite) as shown in Figure 7.20. Similar to the

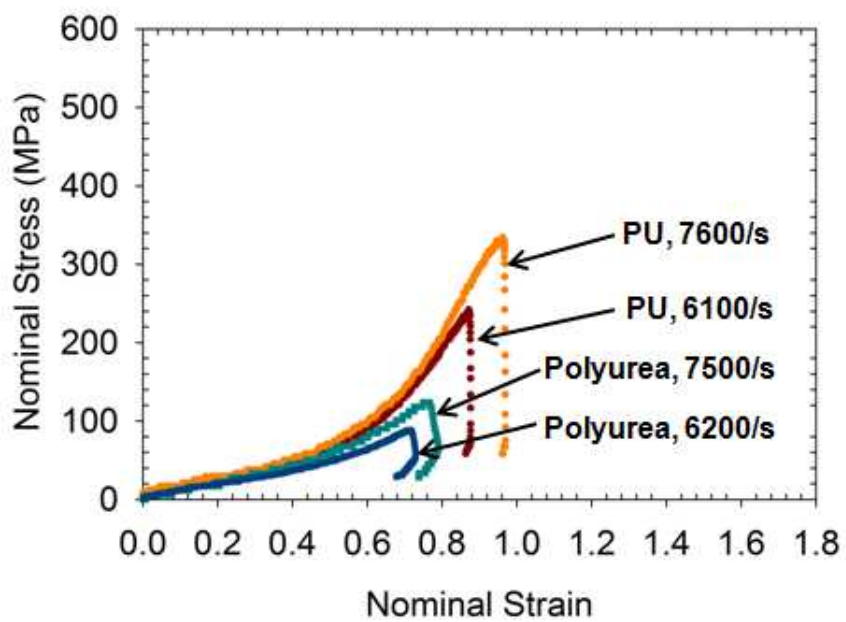


Figure 7.19: Representative nominal stress-strain response of polyurea and PU at high impact rates of about 6200 s^{-1} and 7500 s^{-1} at room temperature ($\sim 23^\circ\text{C}$) and a humidity of $\sim 30\%$. The curves are labelled as (material, strain rate).

behavior seen at low strain-rates (in tension), nanocomposites demonstrated an increase in modulus and yield strength when compared to PU. Both modulus and yield strength continue to increase with volume fraction of MTM nanoparticles. More interestingly, the post-yield response at impact rates showed a further increase in the strain hardening behavior for the nanocomposites when compared with PU. The strain hardening was observed to increase with the MTM volume fraction. In Chapter 6, it was shown that amplified stretch and strain gradients may be used to describe the finite deformation responses of these materials. Here, the presence of MTM nanoparticles may have led to large strain-gradients resulting in an increased strain-hardening response. The energy at the moderate strains increased with an increasing MTM volume fraction as shown in Figure 7.22. The energy at 0.5 strain increased more than 3.5 times with 8 v.% MTM nanoparticles in the PU-PAA-MTM8(h) nanocomposite when compared with PU.

Another interesting and useful observation was made from measuring the residual strains in the polymers and nanocomposites as shown in Figure 7.20. Polyurea and PU underwent zero or very small plastic deformation at unloading, thus recovering most of the deformation. However, with an incorporation of PAA and MTM nanoparticles, the residual strain increased resulting in a permanent deformation in the nanocomposites. This plastic deformation increased with an increase in the volume fraction of MTM nanoparticles. Hence, while the base polymers, polyurea and PU, stored all the strain energy during the deformation, PU-PAA and nanocomposites dissipated some part of this energy in plastically deforming the material. This increased dissipation of energy is favorable for utilizing these materials for the blast mitigation applications.

7.6 Summary and Conclusions

In summary, the role of polymer-nanoparticle interface in controlling the finite deformation response of layered nanocomposites has been investigated. The interfacial interactions between the PU and MTM nanoparticles were altered by varying the effective charge density

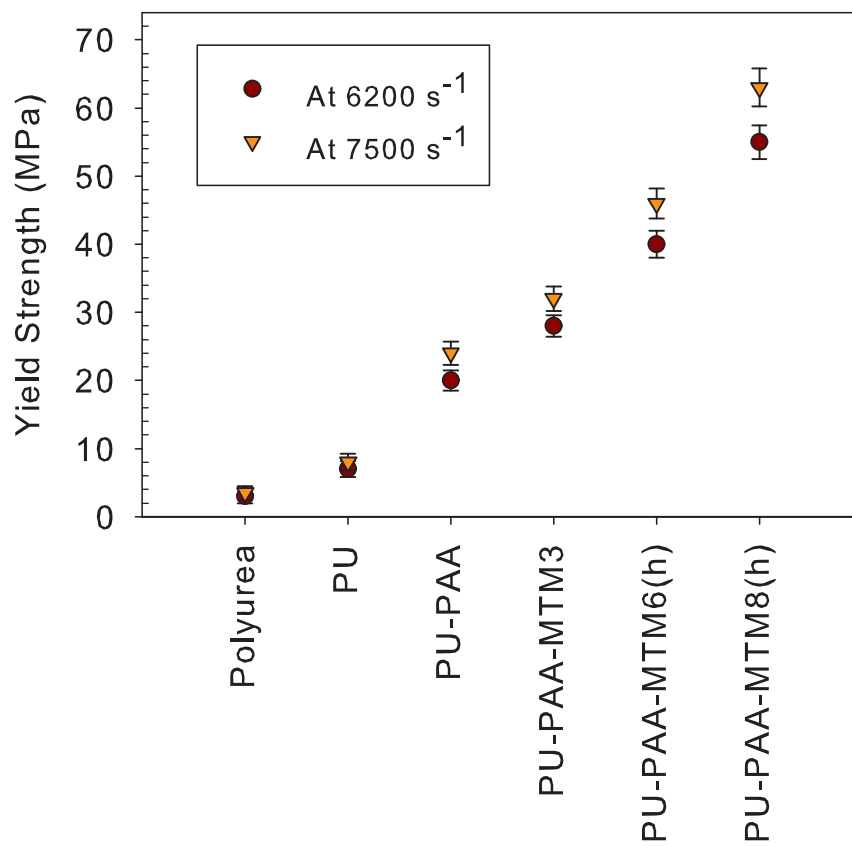


Figure 7.20: Comparison of yield strength of polyurea, PU, PU-PAA and PU-PAA-MTM nanocomposites at high impact rates of about 6200 s⁻¹ and 7500 s⁻¹.

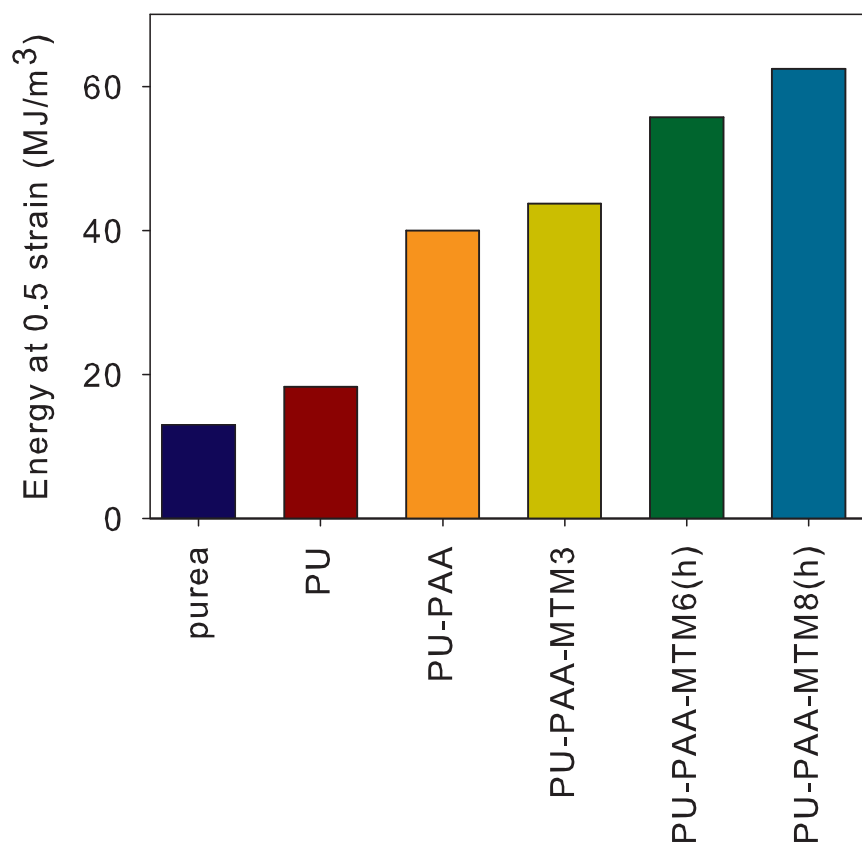


Figure 7.21: Energy at 0.5 strain for PU, Polyurea, PU-PAA and uniformly and hierarchically layered PU-PAA-MTM nanocomposites.

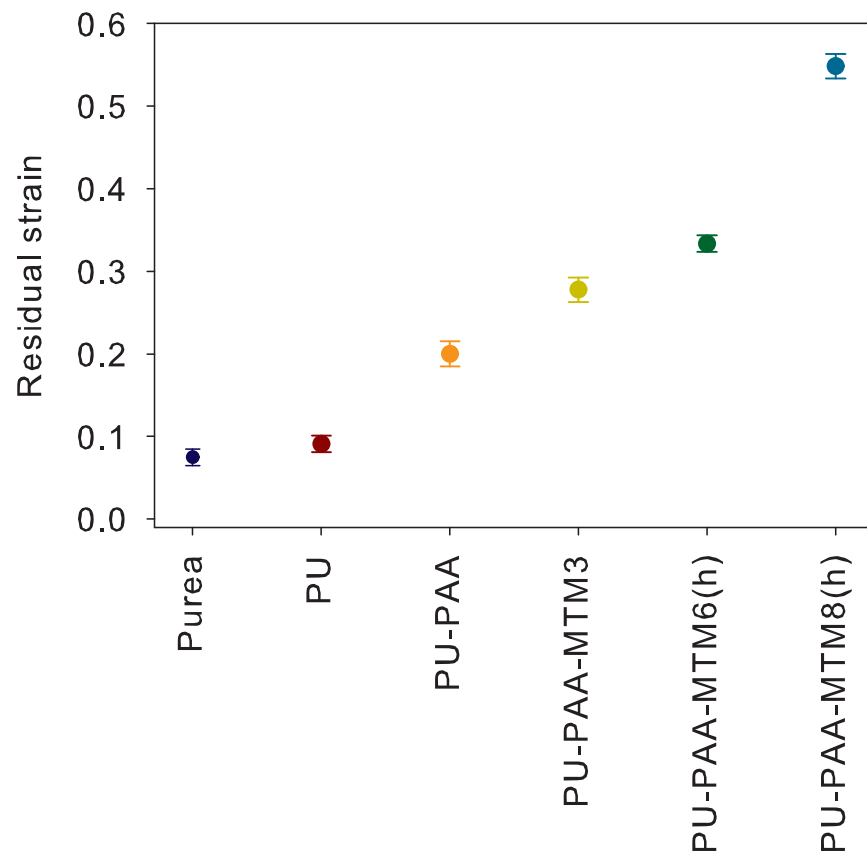


Figure 7.22: Residual strain at unloading for Polyurea, PU, PU-PAA and PU-PAA-MTM nanocomposites.

at the interface. The hierarchical-layered PU-PAA-MTM nanocomposites with a stronger interface demonstrated higher yield strength and modulus as compared to the uniform-layered nanocomposites, owing to the enhanced load transfer between the polymer and the nanoparticle. Here, we demonstrate that it is possible to manufacture nanocomposites which demonstrate simultaneous increase in strength, stiffness and toughness. The high impact investigations of e-LBI PU-PAA-MTM nanocomposites demonstrated increasing strain-hardening with increased MTM volume fraction. Moreover, the plastic deformation in the nanocomposites increased with an increase in MTM volume fraction, thus resulting in an increased energy dissipation.

Chapter 8

Summary and Future Work

The research presented in this work has addressed several issues facing the design of polymer-clay nanocomposites. The use of the LBL manufacturing method allows us to tune various structural parameters like the volume fraction of clay nanoparticles; the clay layer separation or the thickness of the polymer layer; the stratified layer of nanoparticle; and the interface between the polymer and clay nanoparticles in multi-layered polymer-clay nanocomposites. The systematic control over the structure using the LBL method enabled the explicit investigation of the role of each parameter in controlling the finite deformation response of multi-layered polymer-clay nanocomposites. Some of the key findings of this research are summarized below:

- Although the role of the volume fraction of clay nanoparticles is tremendous in increasing the stiffness and strength of the nanocomposites, uniform dispersion of the nanoparticles within the polymer matrix is the key. We have demonstrated this aspect by systematically varying the MTM nanoparticle layer separation or the thickness of PU layer in the multilayered PU-MTM nanocomposites. These nanocomposites demonstrate an increasing yield strength and stiffness with increased MTM volume fraction or reduced nanoparticle layer separation or PU layer thickness. We demonstrate that the PU layer thickness controls the ultimate strain-to-failure of the nanocomposites. An existence of a critical MTM nanoparticle layer separation was determined below which brittle behavior dominated the nanocomposite response. The ductile nanocomposites, with a layer separation above this critical value, were

tough with increased yield strength and stiffness (as compared to PU) and demonstrated consistent ultimate strain-to-failure in tension. The simultaneous improvement in stiffness, strength and toughness in these nanocomposites was the result of the volume fraction of MTM nanoparticles, their strong interaction with the PU matrix and the control of defects such as non-uniform dispersion of MTM nanoparticles.

- Interestingly, the stratified layers of MTM nanoparticles provided an additional slipping mechanism, enhancing the overall ductility, and hence the energy at failure of the PU-MTM nanocomposites under uniaxial tension deformation state. Although the stratified layer reinforces the PU to a lesser extent as compared to a single layer of MTM nanoparticles, leading to smaller stiffness and strength, it provides larger deformation to the nanocomposite before failure.
- The role of interfacial strength is critical in increasing the strength and stiffness of the nanocomposite, owing to the enhanced load transfer between the polymer and the nanoparticle. Using the e-LBL deposition, we demonstrate that this enhanced interface results in an increased stiffness and strength. We also demonstrate that it is possible to manufacture a multi-layered nanocomposite by hierarchical layering that demonstrates increased stiffness, strength and the ultimate strain-to-failure, thus resulting in a tough nanocomposite. This hierarchically layered nanocomposite was tuned to possess enhanced interfacial strength between the polymer matrix and the nanoparticles and increased polymer layer thickness or nanoparticle layer separation.
- The presence of MTM nanoparticles led to large strain-gradients during the finite deformation, resulting in an increased strain-hardening response. This was established using the constitutive modeling approach where these large strain gradients were accounted with the aid of amplified stretch. The stretch amplified as a function of the volume fraction of MTM nanoparticles was a significant reason for the success of the constitutive model to accurately predict the post-yield response of the PU-MTM

nanocomposites. These large strain hardening behavior of PU-MTM nanocomposites could potentially be used in the blast mitigating applications.

The results presented here are only a tip of an iceberg, but nevertheless they present several aspects of the understanding of deformation mechanisms in polymer-clay nanocomposites. The current work mostly focused on determining mechanical properties in the in-plane direction only. However, the properties in the out-of-plane direction may also be crucial for several purposes. Mechanical testing in the out-of-plane direction is difficult due to the slow growth of nanocomposites in the thickness direction. Hence, Brillouin light scattering may be useful to determine the out-of-plane stiffness. Preliminary results along these lines are shown in Figure 8.1. The in-plane (E_1) and out-of-plane (E_2) moduli of PU-MTM nanocomposites, measured using Brillouin light scattering, are shown as a function of the volume fractions of MTM nanoparticles. Interestingly, the values of E_2 are fairly comparable to E_1 , suggesting less than expected anisotropy in these multi-layered nanocomposites. The future work entails comparing these values with those obtained for PU-SMTM nanocomposites.

This work focused on understanding the deformation mechanisms in polymer-clay nanocomposites primarily from the mechanics point of view. However, it would indeed be worthwhile to investigate various reinforcing mechanisms from the chemistry perspective. Experimental techniques like nuclear magnetic resonance (NMR), Fourier transform infrared spectroscopy (FTIR), x-ray photoelectron scattering spectroscopy (XPS) can be used to investigate the formation of linkages between the different phases. These characterizations can further lead to potential optimization of the interactions between the polymer matrix and nanoparticles for enhanced load transfer. Furthermore, stress transfer between the polymer matrix and nanoparticle can be probed in-situ via Raman spectroscopy.

The direction of research in this work was the fundamental understanding of multi-layered nanocomposites. The future work entails on developing advanced composites that could potentially challenge the existing materials. Some of the examples include Kevlar

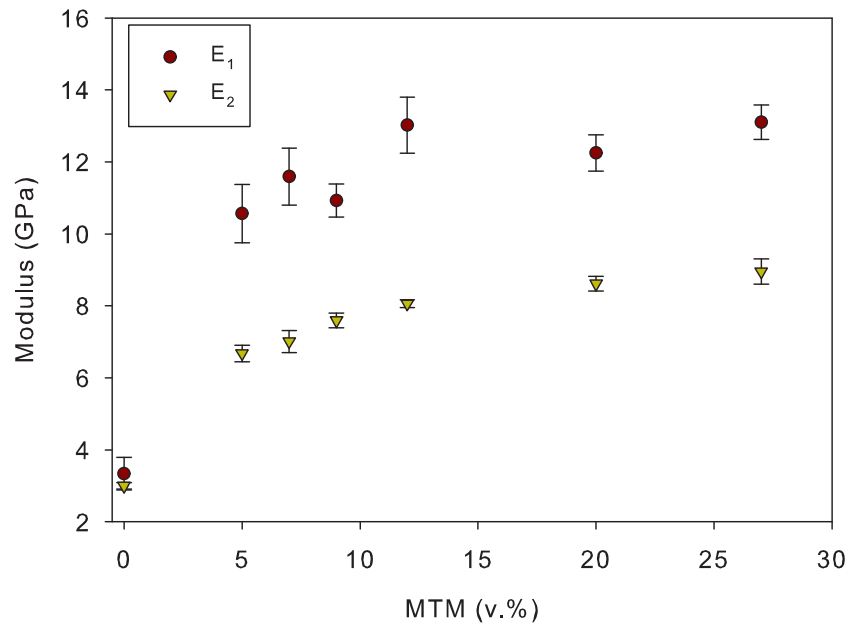


Figure 8.1: In-plane (E_1 , shown in circles) and out-of-plane (E_2 , shown in triangles) modulus of PU-MTM nanocomposites as a function of volume fraction of MTM nanoparticles.

and polycarbonate based nanocomposites. Kevlar is one of the most widely used materials for applications like body armor and polycarbonate is used widely in automotives. An improvement in the properties of these materials by incorporating nanoparticles at the nanoscale can have a large impact.

Bibliography

- [1] Ortiz, C. and Boyce, M. (2008). Bioinspired structural materials. *Science*, 319(5866), pp. 1053–1054. [1](#)
- [2] Heslot, H. (1998). Artificial fibrous proteins: a review. *Biochimie*, 80(1), pp. 19–31. [1](#)
- [3] Hinman, M., Dong, Z., Xu, M. and Lewis, R. (1992). Spider silk: a mystery starting to unravel. *Biomol. Mater.*, (19), pp. 25–34. [1](#)
- [4] Currey, J. (1977). Mechanical properties of mother of pearl in tension. *Proc. R. Soc. Lond.*, 196, pp. 443–463. [1](#)
- [5] Jackson, A., Vincent, J. and Turner, R. (1988). The mechanical design of nacre. *Proc. R. Soc. Lond.*, 234(1277), pp. 415–440. [1](#)
- [6] Gao, H., Ji, B., Jager, I., Arzt, E. and Fratzl, P. (2003). Materials become insensitive to flaws at nanoscale: lessons from nature. *Proc. Nat. Acad. Soc.*, 100(10), p. 5597. [2, 5](#)
- [7] Manevitch, O. and Rutledge, G. (2004). Elastic properties of a single lamella of montmorillonite by molecular dynamics simulation. *J. Phys. Chem. B*, 108(4), pp. 1428–1435. [2, 7](#)
- [8] Bartczak, Z., Argon, A., Cohen, R. and Weinberg, M. (1999). Toughness mechanism in semi-crystalline polymer blends: I. High-density polyethylene toughened with rubbers. *Polymer*, 40, pp. 2331–2346. [4](#)
- [9] Kramer, E. Microscopic and molecular fundamentals of crazing. *Adv. Polym. Sci.*, pp. 1–56. [4](#)
- [10] Liang, J. and Li, R. (2000). Rubber toughening in polypropylene: A review. *J. Appl. Polym. Sci.*, 77(2), pp. 409–417. [4](#)
- [11] Wang, Y. (2002). Characterization, Testing and Constitutive modeling of an impact modified polypropylene. *PhD Thesis, The University of Michigan*. [4, 32, 36, 39](#)
- [12] Mahieux, C. (2001). Cost effective manufacturing process of thermoplastic matrix composites for the traditional industry: the example of a carbon-fiber reinforced thermoplastic flywheel. *Compos. Struct.*, 52(3-4), pp. 517–521. [4](#)

- [13] <http://www.safesimplesoon.com/AresV-config.htm>. 4
- [14] Chan, A. and Hwang, S. (1993). Modeling resin transfer molding of polyimide (PMR-15)/fiber composites. *Polym. Compos.*, 14(6), pp. 524–528. 5
- [15] Xie, W., Pan, W. and Chuang, K. (2001). Thermal characterization of PMR polyimides. *Thermochim. Acta.*, 367, pp. 143–153. 6
- [16] Coleman, J., Khan, U. and Gun'Ko, Y. (2006). Mechanical reinforcement of polymers using carbon nanotubes. *Adv. Mater.*, 18(6), pp. 689–706.
- [17] Patil, A., Vaia, R. and Dai, L. (2005). Surface modification of aligned carbon nanotube arrays for electron emitting applications. *Synth. Metals*, 154(1-3), pp. 229–232. 6
- [18] Schmidt, D., Shah, D. and Giannelis, E. (2002). New advances in polymer/layered silicate nanocomposites. *Curr. Opin. Solid State Mater. Sci.*, 6(3), pp. 205–212. 6
- [19] Okada, A. and Usuki, A. (2006). Twenty years of polymer-clay nanocomposites. *Macromol. Mat. Eng.*, 291(12), pp. 1449–1476.
- [20] Powell, C. and Beall, G. (2006). Physical properties of polymer/clay nanocomposites. *Phy. Prop. Polym.*, pp. 561–575. 6
- [21] Podsiadlo, P., Choi, S., Shim, B., Lee, J., Cuddihy, M., Kotov, N. *et al.* (2005). Molecularly engineered nanocomposites: Layer-by-layer assembly of cellulose nanocrystals. *BioMacromol.*, 6(6), pp. 2914–2918. 6
- [22] Hussain, F., Hojjati, M., Okamoto, M. and Gorga, R. (2006). Review article: polymer-matrix nanocomposites, processing, manufacturing, and application: an overview. *J. Compos. Mater.*, 40(17), p. 1511. 6
- [23] Cho, D., Lee, S., Yang, G., Fukushima, H. and Drzal, L. (2005). Dynamic mechanical and thermal properties of phenylethynyl-terminated polyimide composites reinforced with expanded graphite nanoplatelets. *Macromol. Mater. Eng.*, 290(3), pp. 179–187.
- [24] Sevostianov, I. and Kachanov, M. (2007). Effect of interphase layers on the overall elastic and conductive properties of matrix composites. Applications to nanosize inclusion. *Int. J. Solids Struct.*, 44(3-4), pp. 1304–1315. 6
- [25] Iijima, S. *et al.* (1991). Helical microtubules of graphitic carbon. *Nature*, 354(6348), pp. 56–58. 6
- [26] Holt, J., Park, H., Wang, Y., Stadermann, M., Artyukhin, A., Grigoropoulos, C., Noy, A. and Bakajin, O. (2006). Fast mass transport through sub-2-nanometer carbon nanotubes. *Science*, 312(5776), p. 1034. 7

- [27] Fornasiero, F., Park, H. G., Holt, J. K., Stadermann, M., Grigoropoulos, C. P., Noy, A. and Bakajin, O. (2008). Ion exclusion by sub-2-nm carbon nanotube pores. pp. 1–6. [7](#)
- [28] Sherman, L. (1999). Nanocomposites: a little goes a long way. *Plast. Technol.*, 45(6), pp. 52–54. [7](#), [9](#)
- [29] Usuki, A., Kojima, Y., Kawasumi, M., Okada, A., Fukushima, Y., Kurauchi, T. and Kamigaito, O. (1993). Synthesis of nylon 6-clay hybrid. *J. Mater. Res.*, 8(5), pp. 1179–1184. [9](#), [10](#)
- [30] Usuki, A., Kojima, Y., Kawasumi, M., Okada, A., Fukushima, Y., Kurauchi, T. and Kamigaito, O. (1993). Mechanical properties of nylon 6-clay hybrid. *J. Mater. Res.*, 8(5), pp. 1185–1189. [9](#)
- [31] Giannelis, E. (1996). Polymer Layered Silicate Nanocomposites. *Adv. Mater*, 8, pp. 29–35. [9](#), [10](#), [11](#)
- [32] Alexandre, M. and Dubois, P. (2000). Polymer-layered silicate nanocomposites: preparation, properties and uses of a new class of materials. *Br. Mat. Sci. Eng. R.: Rep.*, 28(1-2), pp. 1–63. [7](#)
- [33] Pinnavaia, T. and Beall, G. (2000). *Polymer-clay nanocomposites*. John Wiley & Sons New York. [7](#)
- [34] Kojima, Y., Usuki, A., Kawasumi, M., Okada, A., Kurauchi, T. and Kamigaito, O. (1993). Synthesis of nylon 6-clay hybrid by montmorillonite intercalated with ϵ -caprolactam. *J. Polym. Sci., Polym. Chem.*, 31(4), pp. 983–986. [9](#)
- [35] Okada, A. and Usuki, A. (1995). The chemistry of polymer-clay hybrids. *Mat. Sci. Eng.*, 3(2), pp. 109–115. [9](#)
- [36] Lan, T. and Pinnavaia, T. (1994). Clay-reinforced epoxy nanocomposites. *Chem. Mater.*, 6(12), pp. 2216–2219. [9](#), [10](#)
- [37] Pinnavaia, T. and Wang, Z. (1998). Hybrid organic-inorganic nanocomposites: exfoliation of magadiite nanolayers in an elastomeric epoxy polymer. *Chem. Mater.*, 10(7), pp. 1820–1826. [9](#)
- [38] Yano, K., Usuki, A. and Okada, A. (2000). Synthesis and properties of polyimide-clay hybrid films. *J. Polym. Sci. Part A: Polym. Chem.*, 35(11), pp. 2289–2294. [9](#)
- [39] Fukushima, Y. and Inagaki, S. (1987). Synthesis of an intercalated compound of montmorillonite and 6-polyamide. *J. Includ. Phen. Macro. Chem.*, 5(4), pp. 473–482. [9](#)
- [40] Vaia, R., Jandt, K., Kramer, E. and Giannelis, E. (1995). Kinetics of polymer melt intercalation. *Macromolecules*, 28(24), pp. 8080–8085. [9](#), [60](#)

- [41] Chen, T., Tien, Y. and Wei, K. (2000). Synthesis and characterization of novel segmented polyurethane/clay nanocomposites. *Polymer*, 41(4), pp. 1345–1353. [9](#), [10](#), [56](#)
- [42] Tortora, M., Gorrasi, G., Vittoria, V., Galli, G., Ritrovati, S. and Chiellini, E. (2002). Structural characterization and transport properties of organically modified montmorillonite/polyurethane nanocomposites. *Polymer*, 43(23), pp. 6147–6157. [11](#), [56](#)
- [43] Pattanayak, A. and Jana, S. (2005). Properties of bulk-polymerized thermoplastic polyurethane nanocomposites. *Polymer*, 46(10), pp. 3394–3406. [10](#)
- [44] Lee, H. and Lin, L. (2006). Waterborne polyurethane/clay nanocomposites: novel effects of the clay and its interlayer ions on the morphology and physical and electrical properties. *Macromolecules*, 39(18), pp. 6133–6141.
- [45] Rao, Y. and Pochan, J. (2007). Mechanics of Polymer- Clay Nanocomposites. *Macromolecules*, 40(2), pp. 290–296. [11](#), [56](#), [60](#), [61](#)
- [46] Lagaly, G. (1999). Introduction: from clay mineral-polymer interactions to clay mineral-polymer nanocomposites. *Appl. Clay Sci.*, 15(1), pp. 1–9. [9](#), [10](#), [11](#), [56](#)
- [47] Hasegawa, N., Okamoto, H., Kato, M. and Usuki, A. (2000). Preparation and mechanical properties of polypropylene-clay hybrids based on modified polypropylene and organophilic clay. *J. Appl. Polym. Sci.*, 78(11), pp. 1918–1922. [9](#)
- [48] Reichert, P., Hoffmann, B., Bock, T., Thomann, R., M^ulhaupt, R. and Friedrich, C. (2001). Morphological stability of poly (propylene) nanocomposites. *Macromol. Rap. Comm.*, 22(7), pp. 519–523.
- [49] Nam, P., Maiti, P., Okamoto, M., Kotaka, T., Hasegawa, N. and Usuki, A. (2001). A hierarchical structure and properties of intercalated polypropylene/clay nanocomposites. *Polymer*, 42(23), pp. 9633–9640.
- [50] Liu, X. and Wu, Q. (2001). PP/clay nanocomposites prepared by grafting-melt intercalation. *Polymer*, 42(25), pp. 10013–10019.
- [51] Zhang, Q., Wang, Y. and Fu, Q. (2003). Shear-induced change of exfoliation and orientation in polypropylene/montmorillonite nanocomposites. *J. Polym. Sci.-B: Polym. Phys.*, 41(1), pp. 1–10. [9](#)
- [52] Rong, J., Jing, Z., Li, H. and Sheng, M. (2001). A polyethylene nanocomposite prepared via in-situ polymerization. *Macromol. Rap. Comm.*, 22(5), pp. 329–334. [9](#)
- [53] Wang, K., Choi, M., Koo, C., Choi, Y. and Chung, I. (2001). Synthesis and characterization of maleated polyethylene/clay nanocomposites. *Polymer*, 42(24), pp. 9819–9826. [79](#)

- [54] Alexandre, M., Dubois, P., Sun, T., Garces, J. and Jérôme, R. (2002). Polyethylene-layered silicate nanocomposites prepared by the polymerization-filling technique: synthesis and mechanical properties. *Polymer*, 43(8), pp. 2123–2132. [9](#), [10](#)
- [55] Podsiadlo, P., Kaushik, A., Arruda, E., Waas, A., Shim, B., Xu, J., Nandivada, H., Pumplun, B., Lahann, J., Ramamoorthy, A. *et al.* (2007). Ultrastrong and stiff layered polymer nanocomposites. *Science*, 318(5847), p. 80. [10](#), [16](#), [17](#), [20](#), [44](#)
- [56] Zerda, A. and Lesser, A. (2001). Intercalated clay nanocomposites: morphology, mechanics, and fracture behavior. *J. Polym. Sci. Part B: Polym. Phys.*, 39(11), pp. 1137–1146. [11](#), [56](#), [61](#)
- [57] Ray, S. (2003). Polymer/layered silicate nanocomposites: a review from preparation to processing. *Prog. Polym. Sci.*, 28(11), pp. 1539–1641. [11](#)
- [58] Chang, J. and An, Y. (2002). Nanocomposites of polyurethane with various organo-clays: thermomechanical properties, morphology, and gas permeability. *J. Polym. Sci. Part B: Polym. Phys.*, 40(7), pp. 670–677. [11](#), [56](#), [61](#)
- [59] Lvov, Y., Haas, H., Decher, G., Moehwald, H. and Kalachev, A. (1993). Assembly of polyelectrolyte molecular films onto plasma-treated glass. *J. Phy. Chem.*, 97(49), pp. 12835–12841. [13](#), [14](#), [24](#)
- [60] Decher, G. (1997). Fuzzy nanoassemblies: toward layered polymeric multicomposites. *Science*, 277(5330), p. 1232. [14](#)
- [61] Kotov, N. (2001). Ordered layered assemblies of nanoparticles. *MRS Bulletin*, 26(12), pp. 992–997. [13](#), [24](#)
- [62] Kotov, N., Dekany, I. and Fendler, J. (1995). Layer-by-layer self-assembly of polyelectrolyte-semiconductor nanoparticle composite films. *J. Phy. Chem.*, 99(35), pp. 13065–13069. [14](#)
- [63] Mamedov, A., Kotov, N., Prato, M., Guldi, D., Wicksted, J. and Hirsch, A. (2002). Molecular design of strong single-wall carbon nanotube/polyelectrolyte multilayer composites. *Nature Mater.*, 1(3), pp. 190–194. [14](#)
- [64] Keller, S., Kim, H. and Mallouk, T. (1994). Layer-by-Layer Assembly of Intercalation Compounds and Heterostructures on Surfaces: Toward Molecular Beaker Epitaxy. *J. Amer. Chem. Soc.*, 116(19), pp. 8817–8818. [14](#)
- [65] Hong, J., Lowack, K., Schmitt, J. and Decher, G. (1993). Layer-by-layer deposited multilayer assemblies of polyelectrolytes and proteins: from ultrathin films to protein arrays. *Trends Colloid Inter. Sci.*, pp. 98–102. [14](#)
- [66] Lvov, Y., Ariga, K. and Kunitake, T. (1994). Layer-by-layer assembly of alternate protein/polyion ultrathin films. *Chem. Lett.*, 23(12), pp. 2323–2326. [14](#)

- [67] Cooper, T., Campbell, A. and Crane, R. (1995). Formation of polypeptide-dye multilayers by electrostatic self-assembly technique. *Langmuir*, 11(7), pp. 2713–2718. [14](#)
- [68] Yoo, P., Nam, K., Qi, J., Lee, S., Park, J., Belcher, A. and Hammond, P. (2006). Spontaneous assembly of viruses on multilayered polymer surfaces. *Nature Mater.*, 5(3), pp. 234–240. [14](#)
- [69] Tang, Z., Wang, Y. and Podsiadlo, P. (2006). Biomedical Applications of Layer-by-Layer Assembly: From Biomimetics to Tissue Engineering. *Adv. Mater.*, 18(24), pp. 3203–3224. [14](#)
- [70] Liu, Y., Wang, A. and Claus, R. (1997). Layer-by-layer electrostatic self-assembly of nanoscale FeO particles and polyimide precursor on silicon and silica surfaces. *Appl. Phys. Lett.*, 71, p. 2265. [15](#)
- [71] Lenahan, K., Wang, Y., Liu, Y., Claus, R., Heflin, J., Marciu, D. and Figura, C. (1999). Novel polymer dyes for nonlinear optical applications using ionic self-assembled monolayer technology. *Adv. Mater.*, 10(11), pp. 853–855. [15](#)
- [72] Tang, Z., Kotov, N., Magonov, S. and Ozturk, B. (2003). Nanostructured artificial nacre. *Nature Mater.*, 2(6), pp. 413–418. [15](#), [25](#), [44](#)
- [73] Stockton, W. and Rubner, M. (1997). Molecular-level processing of conjugated polymers. 4. Layer-by-layer manipulation of polyaniline via hydrogen-bonding interactions. *Macromolecules*, 30(9), pp. 2717–2725. [15](#)
- [74] Caruso, F., Niikura, K., Furlong, D. and Okahata, Y. (1997). Assembly of alternating polyelectrolyte and protein multilayer films for immunosensing. *Langmuir*, 13(13), pp. 3427–3433. [15](#)
- [75] Anzai, J., Kobayashi, Y., Nakamura, N., Nishimura, M. and Hoshi, T. (1999). Layer-by-layer construction of multilayer thin films composed of avidin and biotin-labeled poly (amine) s. *Langmuir*, 15(1), pp. 221–226.
- [76] Cassier, T., Lowack, K. and Decher, G. (1998). Layer-by-layer assembled protein/polymer hybrid films: nanoconstruction via specific recognition. *Supramol. Sci.*, 5(3-4), pp. 309–315. [15](#)
- [77] Deville, S., Saiz, E., Nalla, R. and Tomsia, A. (2006). Freezing as a path to build complex composites. *Science*, 311(5760), p. 515. [16](#)
- [78] Hindeleh, A. and Abdo, S. (1989). Relationship Between Crystalline Structure and Mechanical Properties in Kevlar 49 Fibres. *Polym. Comm.*, 30(6), pp. 184–186. [17](#)
- [79] Yue, C., Sui, G. and Looi, H. (2000). Effects of heat treatment on the mechanical properties of Kevlar-29 fibre. *Compos. Sci. Technol.*, 60(3), pp. 421–427.

- [80] Cheng, M., Chen, W. and Weerasooriya, T. (2005). Mechanical properties of Kevlar® KM2 single fiber. *J. Eng. Mater. Technol.*, 127, p. 197. [17](#)
- [81] Dalton, A., Collins, S., Munoz, E., Razal, J., Ebron, V., Ferraris, J., Coleman, J., Kim, B. and Baughman, R. (2003). Super-tough carbon-nanotube fibres. *Nature*, 423(6941), p. 703. [17](#)
- [82] Podsiadlo, P. (2008). Layer-by-layer assembly of nanostructured composites: mechanical and applications. *PhD Thesis, The University of Michigan*. [20](#)
- [83] Ke, Y. and Stroeve, P. (2005). *Polymer-layered silicate and silica nanocomposites*. Elsevier Science Ltd. [24](#)
- [84] Ferreira, M., Cheung, J. and Rubner, M. (1994). Molecular self-assembly of conjugated polyions: a new process for fabricating multilayer thin film heterostructures. *Thin Solid Films*, 244(1-2), pp. 806–809. [24](#)
- [85] Podsiadlo, P., Arruda, E., Kheng, E., Waas, A., Lee, J., Critchley, K., Qin, M., Chuang, E., Kaushik, A., Kim, H. *et al.* (2009). LBL Assembled laminates with hierarchical organization from nano-to microscale: High-toughness nanomaterials and deformation imaging. *ACS Nano*, 3(6), pp. 1564–1572. [27](#), [109](#)
- [86] Kaushik, A., Podsiadlo, P., Qin, M., Shaw, C., Waas, A., Kotov, N. and Arruda, E. (2009). The Role of Nanoparticle Layer Separation in the Finite Deformation Response of Layered Polyurethane-Clay Nanocomposites. *Macromolecules*, 42(17), pp. 6588–6595. [29](#), [82](#), [83](#), [85](#), [91](#)
- [87] Larkin, L., Calve, S., Kostrominova, T. and Arruda, E. (2006). Structure and functional evaluation of tendon-skeletal muscle constructs engineered in vitro. *Tissue Eng.*, 12(11), pp. 3149–3158. [30](#)
- [88] Malvern, L. (1976). *Engineering Mechanics: Statics*. Prentice Hall. [32](#)
- [89] Wang, Y. and Arruda, E. (2006). Constitutive Modeling of a Thermoplastic Olefin Over a Broad Range of Strain Rates. *J. Eng. Mater. Tech.*, 128, p. 551. [32](#), [78](#), [88](#), [90](#)
- [90] Przybylo, P. (1999). Experimental Investigation and Constitutive Modeling of Rubbery Polymers. *PhD thesis, The University of Michigan*. [33](#), [34](#)
- [91] Meyers, M. (1994). *Dynamic behavior of materials*. Wiley-Interscience. [36](#)
- [92] Rubio-Zuazo, J.; Jiménez-Riobóo, R. R.-C. E. P. C. P. T. C. F. M. E. S.-G. M. (1999). Brillouin characterization of the acoustic waves phase-velocity in $\text{Al}_x\text{Ga}_{1-x}\text{N}$ epilayers. *Mat. Sci. Eng.*, 93, pp. 168–171. [40](#)
- [93] Brillouin, L. (1914). Scattering of Light. *Compt. Rend. Acad. Sci.*, 158, pp. 1331–1334. [40](#)

- [94] McCullough, D. and Regen, S. (2004). Don't forget Langmuir–Blodgett films. *Chem. Comm.*, 2004(24), pp. 2787–2791. [45](#)
- [95] Wang, A., D'Souza, N. and Golden, T. (2008). Ceramic montmorillonite nanocomposites by electrochemical synthesis. *Appl. Clay Sci.*, 42(1-2), pp. 310–317. [51](#), [52](#)
- [96] Moore, D. and Reynolds, R. (1997). *X-ray Diffraction and the Identification and Analysis of Clay Minerals*. Oxford University Press, USA. [51](#), [52](#)
- [97] Xu, W., Johnston, C., Parker, P. and Agnew, S. (2000). Infrared study of water sorption on Na-, Li-, Ca-, and Mg-exchanged (SWy-1 and SAz-1) montmorillonite. *Clays Clay Min.*, 48(1), p. 120. [52](#)
- [98] Li, Y., Kaushik, A., Waas, A., Podsiadlo, P., Kotov, N. and Arruda, E. M. (2010). . *In Preparation*. [53](#)
- [99] Fornes, T. and Paul, D. (2003). Modeling properties of nylon 6/clay nanocomposites using composite theories. *Polymer*, 44(17), pp. 4993–5013. [56](#)
- [100] Ramanathan, T., Liu, H. and Brinson, L. (2005). Functionalized SWNT polymer nanocomposites for dramatic property improvement. *J. Polym. Sci., Part B: Polym. Phys.*, 43(17), pp. 2269–2279. [60](#), [61](#), [82](#)
- [101] Fisher, F., Eitanz, A., Andrews, R., Schadler, L. and Brinson, L. (2004). Spectral response and effective viscoelastic properties of MWNT reinforced polycarbonate. *Adv. Compos. Lett.*, 13(2), pp. 105–111. [60](#), [61](#)
- [102] H., K., Choi, K. and Noh, S. (2010). Preparation and properties of polyurethane dispersions with aromatic/aliphatic mixed diisocyanate. *In Preparation*. [60](#)
- [103] Vaia, R., Sauer, B., Tse, O. and Giannelis, E. (1998). Relaxations of confined chains in polymer nanocomposites: glass transition properties of poly (ethylene oxide) intercalated in montmorillonite. *J. Polym. Sci. Part B: Polym. Phys.*, 35(1), pp. 59–67. [61](#), [82](#)
- [104] Efremov, M., Olson, E., Zhang, M. and Allen, L. (2003). Glass transition of thin films of poly (2-vinyl pyridine) and poly (methyl methacrylate): nanocalorimetry measurements. *Thermochimica Acta.*, 403(1), pp. 37–41. [61](#)
- [105] Shepherd, P., Golemba, F. and Maine, F. (1974). Fillers and reinforcements for plastics. *Adv. Chem. Ser.*, pp. 134–141. [61](#)
- [106] Hwang, J. and Liu, H. (2002). Influence of organophilic clay on the morphology, plasticizer-maintaining ability, dimensional stability, and electrochemical properties of gel polyacrylonitrile (PAN) nanocomposite electrolytes. *Macromolecules*, 35(19), pp. 7314–7319. [61](#)

- [107] Eyring, H. (1936). Viscosity, plasticity, and diffusion as examples of absolute reaction rates. *J. Chem. Phys.*, 4, p. 283. [76](#)
- [108] Argon, A. (1973). A theory for the low-temperature plastic deformation of glassy polymers. *Philos. Mag.*, 28(4), pp. 839–865. [77](#), [78](#)
- [109] Qi, H. and Boyce, M. (2005). Stress-strain behavior of thermoplastic polyurethanes. *Mech. Mater.*, 37(8), pp. 817–839. [78](#), [80](#), [88](#), [89](#)
- [110] Boyce, M., Parks, D. and Argon, A. (1988). Large inelastic deformation of glassy polymers. Part I: rate dependent constitutive model. *Mech. Mater.*, 7(1), pp. 15–33. [78](#), [82](#), [86](#)
- [111] Haward, R. and Thackray, G. (1968). The use of a mathematical model to describe isothermal stress-strain curves in glassy thermoplastics. *Proc. Roy. Soc. Lond. Series A: Math. and Phys. Sci.*, pp. 453–472. [78](#)
- [112] Treloar, L. (2005). *The physics of rubber elasticity*. Oxford University Press, USA. [78](#)
- [113] Arruda, E. and Boyce, M. (2000). Constitutive models of rubber elasticity: a review. *Rubb. Chem. Technol.*, 72, pp. 504–523. [78](#)
- [114] Arruda, E. and Boyce, M. (1993). A three-dimensional constitutive model for the large stretch behavior of elastomers. *J. Mech. Phys. Solids*, 41, pp. 389–412. [78](#), [80](#), [82](#), [87](#)
- [115] Arruda, E., Boyce, M. and Jayachandran, R. (1995). Effects of strain rate, temperature and thermomechanical coupling on the finite strain deformation of glassy polymers. *Mech. Mater.*, 19(2-3), pp. 193–212. [79](#), [87](#)
- [116] Boyce, M., Arruda, E. and Jayachandran, R. (2004). The large strain compression, tension, and simple shear of polycarbonate. *Polym. Eng. Sci.*, 34(9), pp. 716–725. [79](#)
- [117] Qi, H. (2003). Mechanics of abrasive wear of elastomeric materials. *PhD Thesis, The Massachusetts Institute of Technology*. [79](#)
- [118] Kim, J., Kang, T. and Yu, W. (2009). Thermo-mechanical constitutive modeling of shape memory polyurethanes using a phenomenological approach. *Int. J. Plast.*, [80](#), [85](#)
- [119] Smallwood, H. (1944). Limiting law of the reinforcement of rubber. *J. Appl. Sci.*, 15, p. 758. [81](#)
- [120] Guth, E. (1945). Theory of filler reinforcement. *J. Appl. Phys.*, 16, p. 20. [81](#), [88](#)
- [121] Einstein, A. (1906). Eine neue bestimmung der molekül-dimensionen. *Ann. Physik.*, 19, pp. 289–306. [81](#)

- [122] Vand, V. (1948). Viscosity of solutions and suspensions. I. Theory. *J. Phy. Chem.*, 52(2), pp. 277–299. [81](#)
- [123] Mooney, M. (1951). The viscosity of a concentrated suspension of spherical particles. *J. Coll. Sci.*, 6(2), pp. 162–170.
- [124] Budiansky, B. (1965). On the elastic moduli of some heterogeneous materials. *J. Mech. Phy. Solids*, 13(4), pp. 223–227.
- [125] Halpin, J. (1969). Stiffness and expansion estimates for oriented short fiber composites. *J. Compos. Mater.*, 3(4), p. 732. [81](#)
- [126] Mori, T. and Tanaka, K. (1973). Average stress in matrix and average elastic energy of materials with misfitting inclusions. *Acta Metal.*, 21(5), pp. 571–574. [81](#)
- [127] Govindjee, S. (1997). An evaluation of strain amplification concepts via Monte Carlo simulations of an ideal composite. *Rub. Chem. Technol.*, 70(1), pp. 25–37.
- [128] Luo, J. and Daniel, I. (2003). Characterization and modeling of polymer/clay nanocomposites. *Compos. Sci. Tech.*, 63(11), pp. 1607–1616. [82](#)
- [129] Sheng, N., Boyce, M., Parks, D., Rutledge, G., Abes, J. and Cohen, R. (2004). Multiscale micromechanical modeling of polymer/clay nanocomposites and the effective clay particle. *Polymer*, 45(2), pp. 487–506. [82](#)
- [130] Odegard, G., Clancy, T. and Gates, T. (2005). Modeling of the mechanical properties of nanoparticle/polymer composites. *Polymer*, 46(2), pp. 553–562. [82](#)
- [131] Anthonoulis, G. and Kontou, E. (2008). Micromechanical behaviour of particulate polymer nanocomposites. *Polymer*, 49(7), pp. 1934–1942. [81](#)
- [132] Budiansky, B. and Wu, T. (1962). Theoretical prediction of plastic strains of polycrystals. In *Proc. 4th US Nat. Congr. Appl. Mech.*, vol. 1175, p. 1185. [81](#)
- [133] Starr, F., Schroder, T. and Glotzer, S. (2002). Molecular dynamics simulation of a polymer melt with a nanoscopic particle. *Macromolecules*, 35(11), pp. 4481–4492. [81](#)
- [134] Smith, J., Bedrov, D. and Smith, G. (2003). A molecular dynamics simulation study of nanoparticle interactions in a model polymer-nanoparticle composite. *Compos. Sci. Technol.*, 63(11), pp. 1599–1605. [81](#)
- [135] Adnan, A., Sun, C. and Mahfuz, H. (2007). A molecular dynamics simulation study to investigate the effect of filler size on elastic properties of polymer nanocomposites. *Compos. Sci. Technol.*, 67(3-4), pp. 348–356. [81](#)
- [136] Boutaleb, S., Zaïri, F., Mesbah, A., Naït-Abdelaziz, M., Gloaguen, J., Boukharouba, T. and Lefebvre, J. (2009). Micromechanics-based modelling of stiffness and yield stress for silica/polymer nanocomposites. *Int. J. Sol. Struct.*, 46(7-8), pp. 1716–1726. [82](#)

- [137] Brune, D. and Bicerano, J. (2002). Micromechanics of nanocomposites: comparison of tensile and compressive elastic moduli, and prediction of effects of incomplete exfoliation and imperfect alignment on modulus. *Polymer*, 43(2), pp. 369–387. [82](#)
- [138] Fisher, F., Bradshaw, R. and Brinson, L. (2003). Fiber waviness in nanotube-reinforced polymer composites–I: Modulus predictions using effective nanotube properties. *Compos. Sci. Technol.*, 63(11), pp. 1689–1703. [82](#)
- [139] Kaushik, A., A.M., W. and E.M., A. (2010). Layer-by-layer assembled protein/polymer hybrid films: nanoconstruction via specific recognition. *submitted to Mech. Mater.* [82](#)
- [140] Mullins, L. and Tobin, N. (1965). Stress softening of rubber vulcanizates. Part I. Use of strain amplification factor to describe the elastic behavior of filler-reinforced vulcanized rubber. *J. Appl. Poly. Sci.*, 9(9), pp. 2993–3009. [82](#), [88](#)
- [141] Arruda, E. and Boyce, M. (1993). Evolution of plastic anisotropy in amorphous polymers during finite straining. *Int. J. Plast.*, 9(6), pp. 697–720. [87](#)
- [142] Bergstrom, J. and Boyce, M. (1999). Mechanical behavior of particle filled elastomers. *Rubb. Chem. Technol.*, 72(4), pp. 633–656. [88](#)
- [143] Arruda, E., Boyce, M. and Quintus-Bosz, H. (1993). Effects of initial anisotropy on the finite strain deformation behavior of glassy polymers. *Int. J. Plast.*, 9(7), pp. 783–811. [89](#)
- [144] Voigt, W. (1889). Ueber die beziehung zwischen den beiden elasticitats-constanten isotroper. *Wied. Ann.*, 38, pp. 573–587. [91](#)
- [145] Podsiadlo, P., Michel, M., Lee, J., Verploegen, E., Kam, N., Ball, V., Lee, J., Qi, Y., Hart, A., Hammond, P. *et al.* (2008). Exponential growth of LBL films with incorporated inorganic sheets. *Nano Lett.*, 8(6), pp. 1762–1770. [99](#), [106](#)
- [146] Elbert, D., Herbert, C. and Hubbell, J. (1999). Thin polymer layers formed by polyelectrolyte multilayer techniques on biological surfaces. *Langmuir*, 15(16), pp. 5355–5362. [99](#)
- [147] Ruths, J., Essler, F., Decher, G. and Riegler, H. (2000). Polyelectrolytes I: Polyanion/Polycation Multilayers at the Air/Monolayer/Water Interface as Elements for Quantitative Polymer Adsorption Studies and Preparation of Hetero-superlattices on Solid Surfaces. *Langmuir*, 16(23), pp. 8871–8878. [99](#), [100](#)
- [148] Pardo-Yissar, V., Katz, E., Lioubashevski, O. and Willner, I. (2001). Layered polyelectrolyte films on Au electrodes: characterization of electron-transfer features at the charged polymer interface and application for selective redox reactions. *Langmuir*, 17(4), pp. 1110–1118. [100](#)

- [149] Picart, C., Lavallo, P., Hubert, P., Cuisinier, F., Decher, G., Schaaf, P. and Voegel, J. (2001). Buildup mechanism for poly (L-lysine)/hyaluronic acid films onto a solid surface. *Langmuir*, 17(23), pp. 7414–7424. [100](#)
- [150] Lavallo, P., Gergely, C., Cuisinier, F., Decher, G., Schaaf, P., Voegel, J. and Picart, C. (2002). Comparison of the structure of polyelectrolyte multilayer films exhibiting a linear and an exponential growth regime: An in situ atomic force microscopy study. *Macromolecules*, 35(11), pp. 4458–4465. [100](#)
- [151] Richert, L., Lavallo, P., Payan, E., Shu, X., Prestwich, G., Stoltz, J., Schaaf, P., Voegel, J. and Picart, C. (2004). Layer by layer buildup of polysaccharide films: Physical chemistry and cellular adhesion aspects. *Langmuir*, 20(2), pp. 448–458.
- [152] Porcel, C., Lavallo, P., Decher, G., Senger, B., Voegel, J. and Schaaf, P. (2007). Influence of the polyelectrolyte molecular weight on exponentially growing multilayer films in the linear regime. *Langmuir*, 23(4), pp. 1898–1904. [99](#)
- [153] Nam, S. and Lee, Y. (1997). Pervaporation and properties of chitosan-poly (acrylic acid) complex membranes. *J. Memb. Sci.*, 135(2), pp. 161–171. [109](#)
- [154] Huang, Y., Lu, J. and Xiao, C. (2007). Thermal and mechanical properties of cationic guar gum/poly (acrylic acid) hydrogel membranes. *Polym. Degrad. Stab.*, 92(6), pp. 1072–1081. [109](#)
- [155] Gao, C., Leporatti, S., Moya, S., Donath, E. and Mohwald, H. (2001). Stability and mechanical properties of polyelectrolyte capsules obtained by stepwise assembly of poly (styrenesulfonate sodium salt) and poly (diallyldimethyl ammonium) chloride onto melamine resin particles. *Langmuir*, 17(11), pp. 3491–3495. [109](#)
- [156] Tekalur, S., Shukla, A. and Shivakumar, K. (2008). Blast resistance of polyurea based layered composite materials. *Compos. Struct.*, 84(3), pp. 271–281. [122](#)
- [157] Yi, J., Boyce, M., Lee, G. and Balizer, E. (2006). Large deformation rate-dependent stress–strain behavior of polyurea and polyurethanes. *Polymer*, 47(1), pp. 319–329. [122](#)
- [158] Amirkhizi, A., Isaacs, J., McGee, J. and Nemat-Nasser, S. (2006). An experimentally-based viscoelastic constitutive model for polyurea, including pressure and temperature effects. *Philos. Mag.*, 86(36), pp. 5847–5866.
- [159] Bahei-El-Din, Y. and Fredricksen, O. (2006). A blast-tolerant sandwich plate design with a polyurea interlayer. *Int. J. Solids Struct.*, 43(25), pp. 7644–7658. [122](#)
- [160] Davidson, J., Porter, J., Dinan, R., Hammons, M. and Connell, J. (2004). Explosive testing of polymer retrofit masonry walls. *J. Perform. Const. Fac.*, 18, p. 100.
- [161] Xue, Z. and Hutchinson, J. (2007). Neck retardation and enhanced energy absorption in metal-elastomer bilayers. *Mech. Mater.*, 39(5), pp. 473–487.

- [162] Roland, C., Twigg, J., Vu, Y. and Mott, P. (2007). High strain rate mechanical behavior of polyurea. *Polymer*, 48(2), pp. 574–578. [122](#)